論文 / 著書情報
Article / Book Information

題目(和文)	電気化学的水分解およびCO2還元を目的としたSiC光電極の開発
Title(English)	The development of SiC photo-electrodes for electrochemical water-splitting and CO2 reduction
著者(和文)	宋浚太
Author(English)	Jun Tae Song
出典(和文)	学位:博士（工学）, 学位授与機関:東京工業大学, 報告番号:甲第9786号, 授与年月日:2015年3月26日, 学位の種別:課程博士, 審査員:波多野　睦子,小田　俊理,宮本　恭幸,河野　行雄,小寺　哲夫,藤井　克司
Citation(English)	Degree:, Conferring organization: Tokyo Institute of Technology, Report number:甲第9786号, Conferred date:2015/3/26, Degree Type:Course doctor, Examiner:,,,,,
学位種別(和文)	博士論文
Type(English)	Doctoral Thesis

The development of 3C-SiC photo-electrodes for electrochemical water-splitting and CO_2 reduction

A thesis submitted

In fulfillment of the requirements for the degree of

Doctor of Engineering

by

Jun Tae Song

Supervised by Prof. Mutsuko Hatano

To the

Department of Physical Electronics

Graduate of Science and Engineering

Tokyo institute of Technology

March 2015

Abstract

This thesis presents the development of SiC photo-electrodes towards improvement of the solar-to-chemical conversion efficiency and stability for water-splitting and CO_2 reduction. The band-edge structure of the 3C-SiC semiconductor analyzed by impedance measurement shows the 3C-SiC has a sufficient potential for the application. However, the dominant obstacles causing unfavorable performance are a high overpotential for water-oxidation reaction and surface corrosion. To overcome these problems, Pt nanoparticles were optimally fabricated on the 3C-SiC surface to promote the carrier transfer at the 3C-SiC/liquid interface. In the viewpoint of durability, the Pt nanoparticles lead to the effect of suppressing the surface oxidation, although the photocurrent still decreases with time. As an approach to the further enhancement of stability, the effect of graphene was investigated as a passivation layer on 3C-SiC. Finally, production of CO gas by the carriers generated from the 3C-SiC photo-anode in aqueous solution was achieved by the CO_2 reduction. These results indicate that the 3C-SiC semiconductor is prospective as a photo-electrode for the realization of the artificial photosynthesis system.

Table of contents

Figures and tables

Chapter 1
Background and objective of the research

1.1 Energy and Environmental crisis

Since the industrial revolution in the period of 18 - 19th century, the new technologies such as electricity, new materials and the combustion engine have emerged. The development of these technologies has provided mankind convenient life. According to the development, the demand for energy has been increased at the same time with large increase of global population. Figure 1.1 shows the rate of energy consumption all over the world.[1] Currently, more than 7 billion people are consuming the oil energy of over 15 TW per year. Fossil fuels such as oil, coal and natural gas are considered as very important energy resource covering more than 80 % of the energy for human beings.

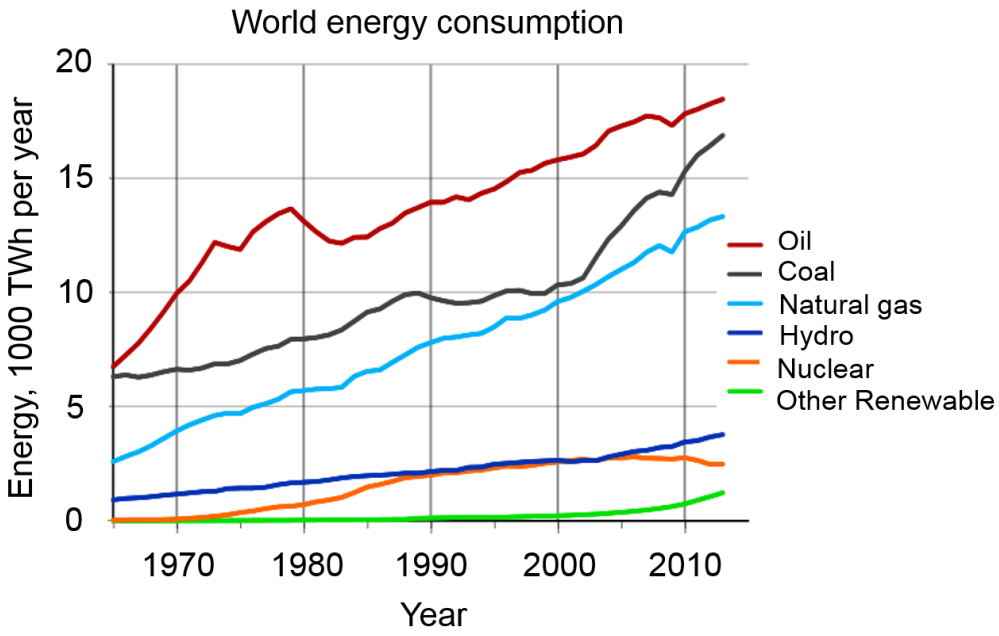

Figure 1.1. Trend of world energy consumption rate. (Adapted from the reference 1)

Chapter 1. Background and objective of the research

These highly increasing consumption of the fossil fuels leads to global energy and environmental problems. First of all, indiscriminate use of fossil fuel energy has threatened the earth while causing the air pollution and emitting carbon dioxide (CO_2) in the atmosphere. Especially, a level of CO_2 gas which is considered as one of the greenhouse gases has grown dramatically for a few decades because almost energy needs have been satisfied by burning of fossil fuels as reviewed above. Figure 1.2 is a record for CO_2 concentration which called as Keeling curve observed at Mauna Loa for about 50 years.[2] In this graph, CO_2 gas concentration in 80 ppm in the atmosphere has increased for 50 years. Although greenhouse gases originally have a positive effect to keep the temperature in the earth, the phenomena was proved to be abnormal with climate change. In Figure 1.3, the global temperature rise in a similar tendency to the CO_2 concentration.[3] Therefore, such a significant growth of CO_2 emission has brought negative effect in result of global warming. In this situation, lots of clean technologies have been developed since Kyoto protocol was adopted in 1997 to decrease the main greenhouse gas, CO_2.

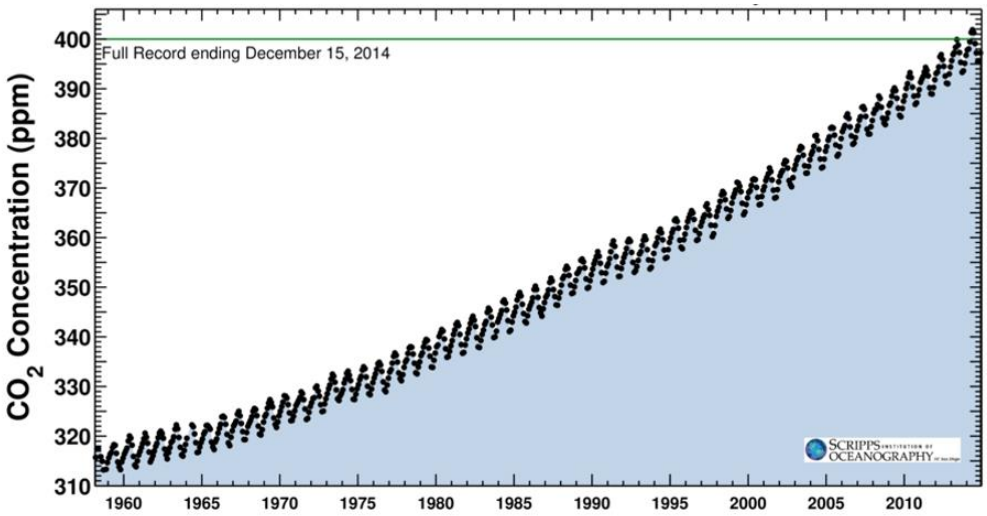

Figure 1.2. The record of CO_2 concentration for about 50 years. (Adapted from the reference 2)

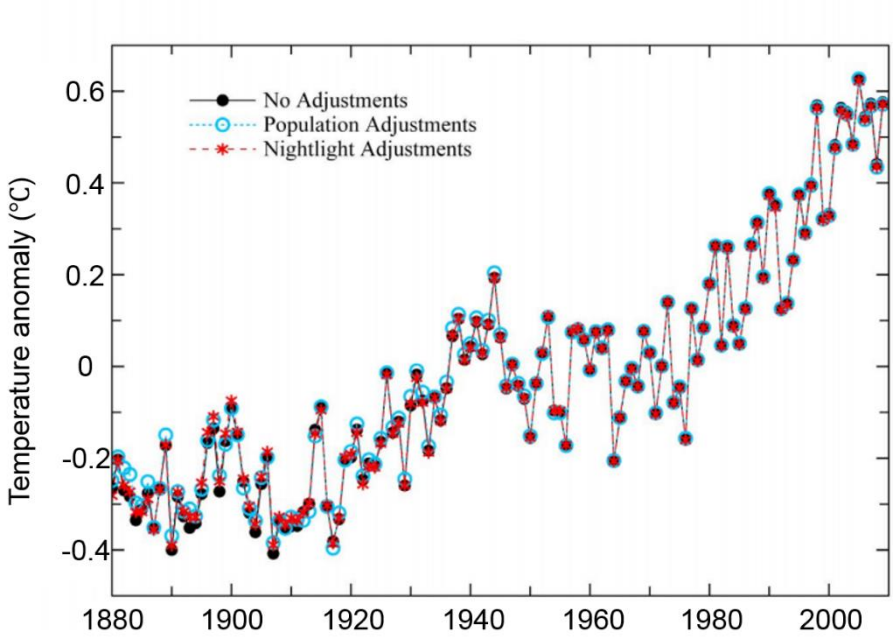

Figure 1.3. Global mean annual mean land-ocean temperature index. (Adapted from the reference 3)

In addition to the environmental issue, the oil energy production is expected to be declined due to the crisis of fossil fuel depletion in the future. The fossil fuel energy reserve is predicted to be exhausted in 100 years as shown in Figure 1.4.[4] This situation is providing a challenge to meet the need of energy with other energy resource.

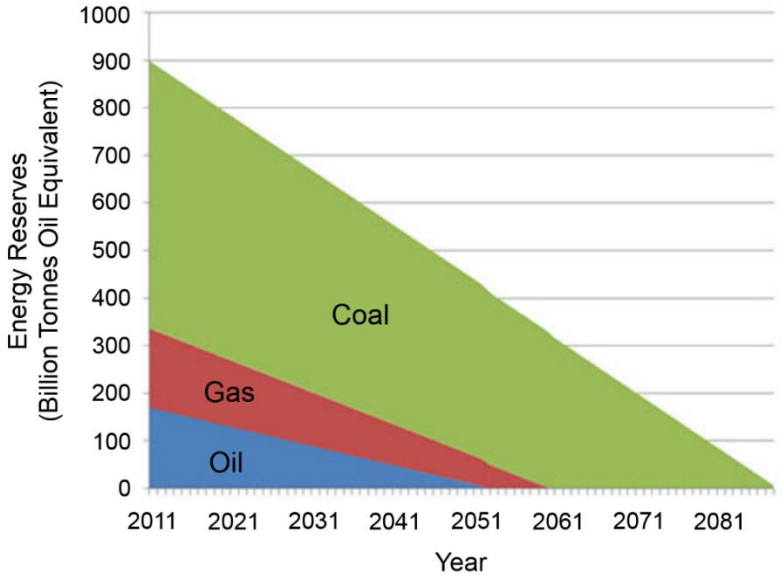

Figure 1.4. The expected available period of fossil fuel production. (Adapted from the reference 4)

1.2 The status of renewable energy

In the circumstance, new concept energy resources which are clean and sustainable is strongly necessary to be developed to solve the problems. As discussed in Section 1.1, the requirement of energy is being met with fossil fuels even if the reserves are decreasing constantly with a rapid development of science and technology. However, Figure 1.5 shows that the renewable energy covers merely 7 % in a whole energy consumption (recorded in 2009). Among the types of renewable energy, biomass is the most actively used with 53 %. Somewhat surprising is that usage of the solar energy is recorded to the smallest, 1 % (In the

record of 2013, it is slightly increased to 2 % in renewable energy consumption).[5] The reason why solar energy has the largest potential to satisfy the whole power consumption with assumption that the surface of 0.8 % on earth is covered by solar cells with 10 % efficiency as shown in Figure 1.6. (Average power of the solar energy reaching on the land is 36,000 TW) Actually, the improvement of the various solar cells with an efficiency over 40 % (in respect to research step (world record)) has been achieved at this moment.[6]

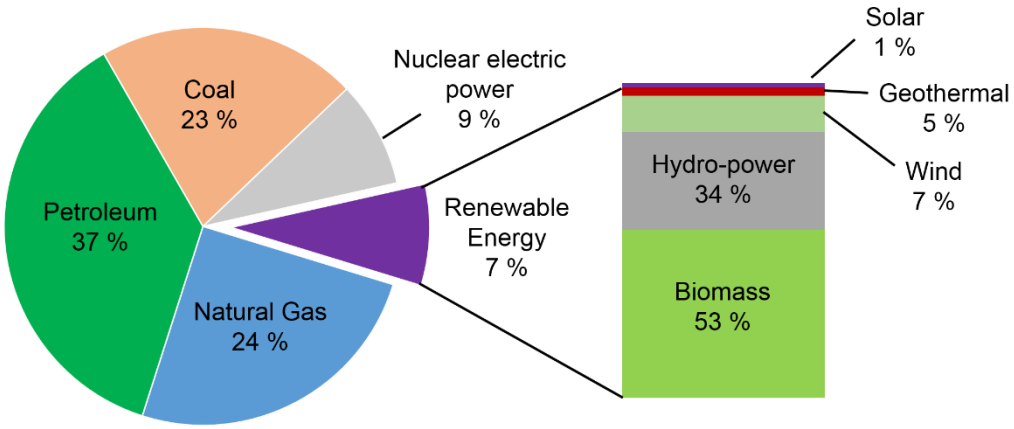

Figure 1.5. The ratio of renewable energy consumption in 2009. (Adapted from the reference 7)

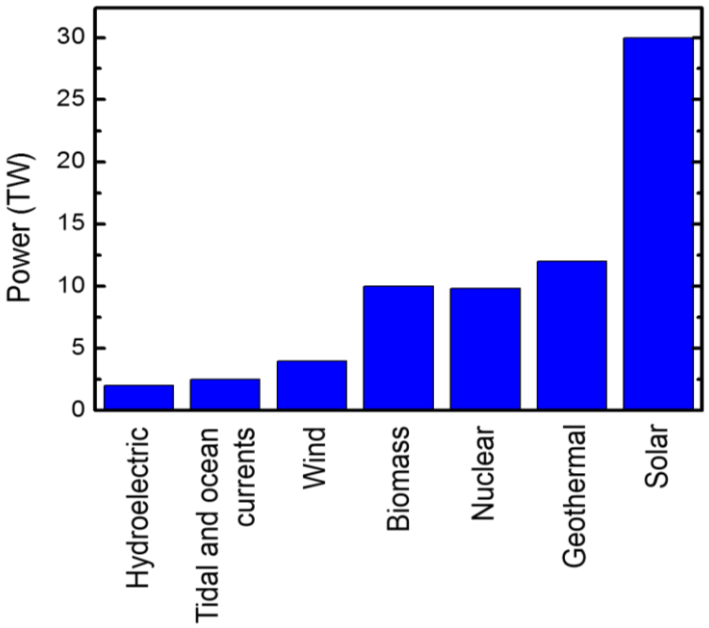

Figure 1.6. The capacity to generate power of diverse renewable energy resource. (Adapted from the reference 8)

Despite of the intensive progress for solar cell technology over the past a few decades, the solar energy has a limitation of intermittency. The electric grid system has been implemented for energy storage to solve this problem. However, another issue to maintain the grid system as the growth of market while the capacity should be exceeded in the near future. As one pathway to solution, chemical fuel can be produced by this intermittent energy resources, solar energy. Besides, the energy density of chemical fuels is superior as compared to batteries and capacitors as shown in Table 1.1.

Table 1.1. Energy densities of various energy materials. (Adapted from the reference 9)

Storage material	**Type of energy**	**Specific energy (MJ/kg)**	**Applications**
Hydrogen	Chemical	142	rocket, automotive engine
Methane	Chemical	55.5	cooking, automotive engine
Ethanol fuel	Chemical	26.4	stoves, lighting
Wood	Chemical	16.2	heating, cooking
Lithium battery	Electrochemical	1.8	portable electronic
Lithium-ion battery	Electrochemical	0.36 – 0.875	laptop, mobile device
Super capacitor	Electrochemical	0.018	electronic circuits

Among the chemical energies, methane and ethanol fuel need a carbon as a source in their synthesis routes. Carbon can be obtained from the CO_2 gas in atmosphere. In this case, it is promising strategy to serve the energy and reduce the CO_2 concentration in the viewpoint of environment. The conversion of CO_2 to those fuels is possible by electrochemical reduction. Although it is very hard challenge due to the necessity of a number of electrons transfer to synthesis, this technology is essential against greenhouse effect. But most of all, hydrogen (H_2) has the highest energy density and is applied as main energy resource for automotive engine which is one of the main reasons for pollution in the near future. Thus, the increase of commercial hydrogen usage leads to make a breakthrough for energy and environmental issues. There exist some technologies to synthesize the hydrogen. Especially, the core technology is water-splitting conducted by thermochemical, electrolysis and photolysis (photoelectrochemical (PEC) method) processes.[10] Among these ways for water-splitting, solar conversion to chemical has been recently considered as a promising strategy. The most beneficial merit is to use the solar light which has largest capacity for

energy demand as an energy resources. As the products, H_2 and oxygen (O_2) are obtained from water-splitting and hydrocarbon is evolved from CO_2 reduction. In this thesis, the development of semiconductor device for solar conversion to chemical is a main focus.

1.3 The prospective of hydrogen production cost and efficiency

In the current situation of renewable energy, it is demonstrated that chemical fuel is very important energy carrier to cover the energy needs of human beings. According to the importance, artificial photosynthesis technology for water-splitting and CO_2 reduction has been developed. U.S. DOE (Department of Energy) set the objectives to reduce the cost of hydrogen production to \$2 – \$4/gge (gasoline gallon equivalent) under the considerations including a gasoline prices. This target price of hydrogen production would be equal to the one of gasoline.[11, 12] B. A. Pinaud *et al*. present a technical and economic feasibility for solar hydrogen production with PEC device with various designs of reactors. According to their calculation, the simplest structure of single photoactive particle with baseline solar-to-hydrogen (STH) conversion efficiency of 5 ~ 10 % shows the \$2.3 ~ \$1.6 per kg H_2. However, the calculated cost of hydrogen for other types which is complex absorber structures (e.g. dual photoactive particle structure) is in the range of \$3 - \$10. Even if we need to more realistic consideration to apply the various materials for photo-electrode, it needs to simplify the structure of PEC device (single absorber) with higher efficiency over 5 % to minimize the cost to achieve a practical application.

1.4 The methods of solar-light energy storage

The storage of solar-light energy to chemical can be achieved by two different approaches. These methods are fundamentally based on water-splitting to obtain H_2. First, it is simply realized with combination of photovoltaic (PV) solar cell and electrochemical cell consists of two metal electrodes as shown in Figure 1.7(a).[13-14] Water-splitting is performed by two metal electrodes which is same as general electrolysis. The only difference is that the voltage is supplied by PV solar cell. Here, the voltage has to be achieved over 1.23 V which is a necessary to decompose the water molecules thermodynamically. Since the solar cell with Si shows the photovoltage of around 0.6 V, it is not enough for driving water-splitting. Therefore, it is necessary to connect in series. Otherwise, multi-junction has to be proposed to overcome this difficulty. The operation of combination with PV and electrochemical cell is expressed with calculation of achievable STH efficiency in Section 3.3.3. The most important issue is that the operation balance has to be considered between electrochemical cell and solar cell. In this process, electricity loss which has to be reduced for efficient chemical storage can be occurred. Although high STH efficiency with special structure is currently achievable over 10 % with this method, the complex structure causing the fabrication cost is inevitably required to supply a sufficient photovoltage and minimize the loss of electricity. As different method, direct PEC process is realized for solar storage to chemical fuels from the water. Figure 1.7(b) shows the configuration of PEC cell with semiconductor and metal electrodes. Since Fujishima and Honda present the PEC water-splitting process by a titanium dioxide (TiO_2) semiconductor electrode, significant PEC technology has been developed.[15, 16] In this method, generated carriers at semiconductor electrode by solar-light are directly contributed to the electrochemical reaction. Therefore, the loss originated from mismatch of

operating point and maximum output point of solar cell in case of the PV combination can be negligible in direct PEC process. Also, STH efficiency over 10 % can be achieved with single photo absorber structure in case of proper semiconductor material. The proper semiconductor material will be discussed in Section 1.5.3. That is, direct PEC process with ideal semiconductor electrode is promising method as solar conversion storage technology. Although many researchers have approached to improve the efficiency of artificial photosynthesis with various designs and structures, it is still insufficient for ultimate target as discussed in Section 1.3.[17, 18]

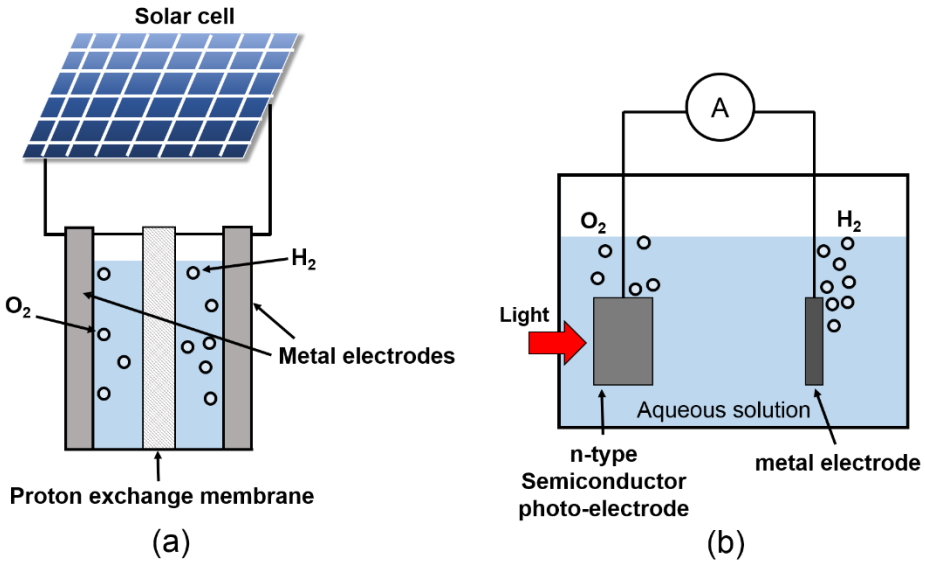

Figure 1.7. Representative configurations of hydrogen storage by water-splitting with solar-light energy. (a) Combination of PV solar cell and electrochemical cell, and (b) PEC cell with semiconductor photo-electrode and metal electrode. (Adapted from reference 17)

1.5 Principle of PEC process

1.5.1 Semiconductor/Electrolyte junction

The basic principle for PEC operation will be discussed with the energy level diagram of semiconductor and electrolyte. The PEC cell includes semiconductor electrode soaked in the aqueous solution forming the semiconductor/electrolyte junction. When n-type semiconductor immersed in electrolyte, the electrochemical potential of electrons in semiconductor side is considered as its Fermi level. The electronic property of electrolyte which is studied by Marcus and Gerischer is depicted in Figure 1.8. The oxidized species and reduced species are considered as acceptors and donors which corresponds to conduction and valance band of semiconductor electronic property. Here, the potential of electrolyte (E_{redox}) is described by Nernst equation as following.

$$E_{redox} = E^{0}{}_{redox} + (RT / zF)\ln(C_{ox} / C_{red}) \quad (1.1)$$

$E^{0}{}_{redox}$: standard redox potential of electrolyte

R : the gas constant

z : the number of electrons for the reaction

F : Faraday constant

C_{ox} : the concentration of oxidized species

C_{red} : the concentration of reduced species

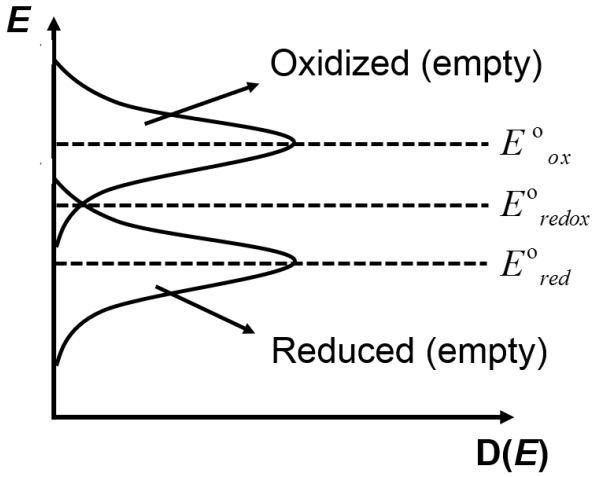

Figure 1.8. Energy diagram of electrolyte.

Figure 1.9 shows the change of band diagram between semiconductor and electrolyte. In the aqueous solution, electron transfer occurs at the interface between semiconductor electrode and electrolyte until the equilibrium state in which Fermi level of two phase is equal similarly to the principle of PN junction in semiconductor device. The electron transfer cause the charge distribution at the interface. As a result, conduction and valance band of semiconductor are bent while the space charge region is formed as shown in Figure 1.9(b) and (d). The width of depletion layer (W_{dep}) is given by:

$$W_{dep} = (2\varepsilon_s\varepsilon_0 V_B / qN_D)^{1/2} \quad (1.2)$$

ε_s : dielectric constant of semiconductor

ε_0 : permittivity of free space

V_B : potential drop at the depletion layer

q : electronic charge

Due to the difference of majority carriers in n- and p-type semiconductor, the direction of band-bending is opposite. Thus, n- and p-type semiconductors work as anode and cathode in the PEC cell composition, respectively. Also, charged layer which is called as Helmholtz layer is formed on the side of electrolyte as shown in Figure 1.9 (e). The ions in the electrolyte against the charge at the space charge region in semiconductor are gathered at the interface. As the result, the potential is distributed from the space charge region (V_{sc}) to double layer (V_H). However, its width is very thin known as few Å.[19] Because the capacitance of this component is serially connected to the semiconductor component, most electric field is distributed across the depletion layer (~ a few μm) in semiconductor side. Therefore, potential distribution in depletion region is the most determinant factors for separation of photo-generated carriers in PEC process.[20]

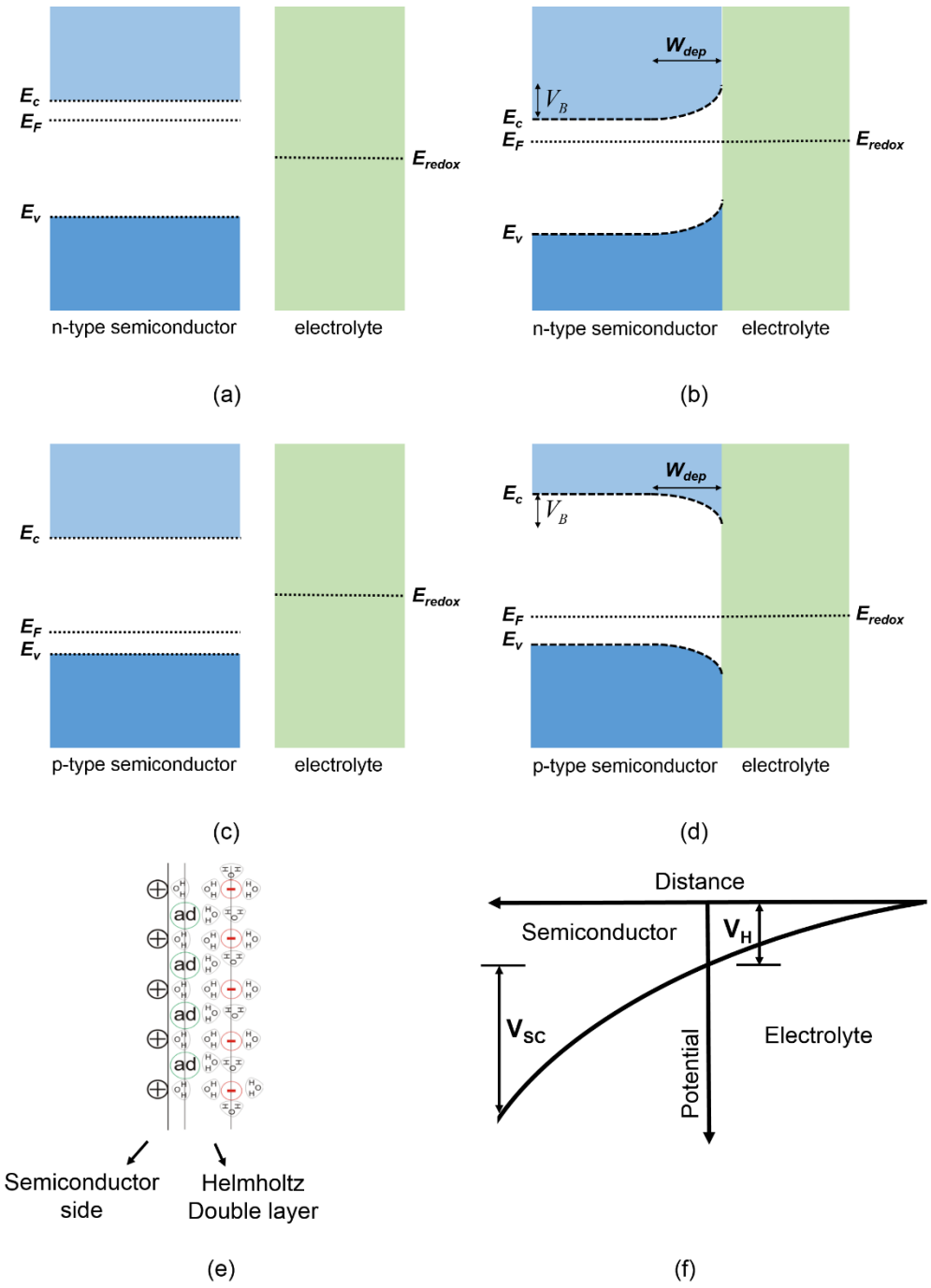

Figure 1.9. The formation of n- and p-type semiconductor/electrolyte junction. (a), (c) Separated band diagram for n- and p-type semiconductor, (b), (d) equilibrium condition between n- and p-type semiconductor and electrolyte, respectively, (e) Illustration of Helmholtz double layer on charged semiconductor surface, (f) Potential distribution at the interface between semiconductor and electrolyte.

1.5.2 PEC water-splitting and CO_2 reduction

Based on the basic theory for semiconductor/electrolyte junction, PEC cell which consist of an n-type semiconductor electrode and a metal counter electrode in aqueous solution as shown in Figure 1.10. Water-splitting reaction is presented as two different chemical equations with regards to the condition of pH as followings.

In case of the hydrogen ion (H^+) activity is 1 (pH = 0):

$$2H^+ + 2e^- \leftrightarrow H_2(g) \text{ (0 V vs. NHE)} \quad (1.3)$$

$$O_2(g) + 4H^+ + 4e^- \leftrightarrow 2H_2O \text{ (1.23 V vs. NHE)} \quad (1.4)$$

In case of the hydroxide ion (OH^-) activity is 1 (pOH = 1):

$$2H_2O + 2e^- \leftrightarrow H_2(g) + 2OH^- \text{ (-0.827 V vs. NHE)} \quad (1.5)$$

$$O_2(g) + 4e^- + 2H_2O \leftrightarrow 4OH^- \text{ (0.403 V vs. NHE)} \quad (1.6)$$

As expressed in above chemical equations, oxidation and reduction reaction are driven by the carrier transfer (electron) at anode and cathode side, respectively. The carriers can be generated at the semiconductor electrode by light illumination. Then, photo-generated carriers are separated and contribute the redox reaction at anode and cathode side. The important point is that the water-splitting reaction requires more than 1.23 V potential which is necessary Gibbs free energy (ΔG), 237 kJ/mol to break the water molecules. The overall water-splitting reaction in PEC cell is simply expressed by:

$$2H_2O \rightarrow 2H_2 + O_2 \ (\Delta G = 237 \text{ kJ/mol}) \quad (1.7)$$

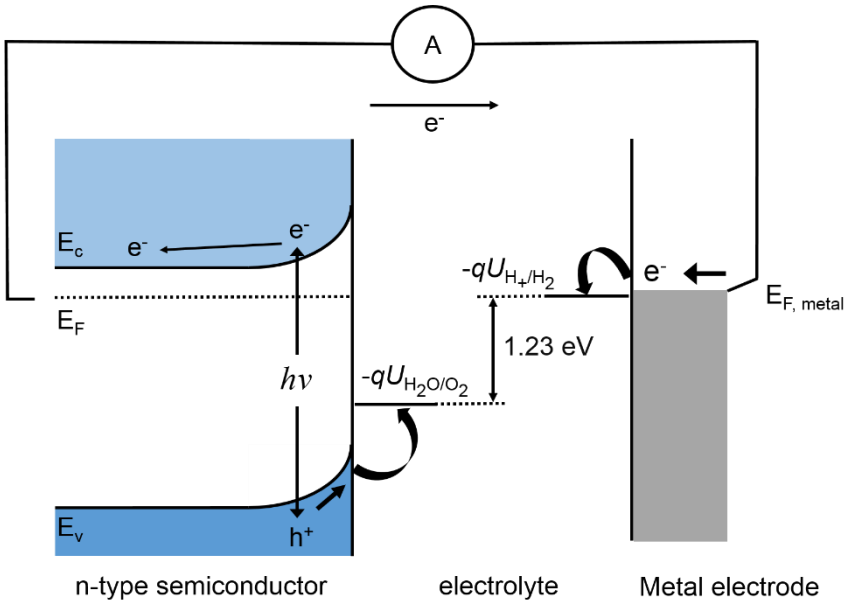

Figure 1.10. The energy diagram in electric connection of semiconductor and metal electrode for water-splitting. ($h\nu$: incident light energy (ν : light wavelength), $-qU_{H^+/H_2}$ and $-qU_{H_2O/O_2}$: the potential for water reduction and oxidation)

In order to drive PEC water-splitting, not only ΔG is required 1.23 eV at least but also the product evolving potential ($-qU$) is essentially satisfied. It depends on the property of semiconductor material itself and will be discussed in next section. Similarly, the PEC CO_2 reduction is practicable principally in the same configuration of PEC cell in Figure 1.10. Through the CO_2 reduction, diverse carbon-based materials can be obtained. The primary reactions at pH = 0 are shown below:[21]

$$CO_2 + H_2O + 2e^- = CO + 2OH^- \text{ (-0.52 V vs. NHE)} \quad (1.8)$$

$$CO_2 + 6H_2O + 8e^- = CH_4 + 8OH^- \text{ (-0.25 V vs. NHE)} \quad (1.9)$$

$$2CO_2 + 8H_2O + 12e^- = C_2H_4 + 12OH^- \text{ (-0.34 V vs. NHE)} \quad (1.10)$$

$$2CO_2 + 9H_2O + 12e^- = C_2H_5OH + 12OH^- \text{ (-0.33 V vs. NHE)} \quad (1.11)$$

As shown in Eq. (1.8) – (1.11), direct CO_2 reduction with water requires much large negative potential than water-splitting ($-qU_{H^+/H_2} = 0$ V vs. NHE). In addition to the potential, it needs more than 2 electrons transfer except for CO. These conditions indicates CO_2 reduction is very high challenging task as compared to water-splitting. The necessity of semiconductor materials for CO_2 conversion will be also discussed in next section.

1.5.3 Semiconductor materials choice for photo-electrode

Semiconductor material for PEC chemical fuel production by solar-light needs to fulfill several important properties. First, the materials have to utilize the solar-light efficiently. The higher ratio of absorption in whole solar spectrum can generate many carriers which would contribute the PEC reaction in semiconductor. Figure 1.11 shows the solar spectrum which is especially AM 1.5 G spectrum. About 47 % of whole solar spectrum is visible light range (380 – 750 nm). However, ultraviolet (UV) range below 380 nm occupies only 2 %. Due to this property of solar spectrum, we need the semiconductor materials which has smaller band-gap value to absorb the larger proportion of solar spectrum. Figure 1.12 shows the ideal maximum solar-to-hydrogen (STH) conversion efficiency of the semiconductors with various band-gap (E_g). The STH efficiency with AM 1.5 G is defined as following.

$$\mathrm{STH} = \left[\frac{\left| j_{sc}\,(\mathrm{mA\ cm^{-2}}) \right| \cdot 1.23\ (\mathrm{V})}{100\ \mathrm{mW\ cm^{-2}}} \right] \quad (1.12)$$

where j_{sc} is the ideal photocurrent, 100 mW cm^{-2} is power density of AM 1.5 G. 1.23 V is the potential for water-splitting. The calculation of Figure 1.12 is performed with an

assumption that each semiconductor material can generate exactly one electron-hole pair by excited one incident photon. We note that it is impossible to split water below 1.23 eV thermodynamically. Even in this impractical condition, the semiconductor with band-gap above 3 eV barely achieve 1 %. The band-gap of 1.5 eV can achieve 50 %. Generally, however, about 1.8 ~ 1.9 eV band-gap value is the minimum boundary for water-splitting application in consideration of common losses.[12, 22] For the rough choice of the band-gap range to achieve over 10 % of STH conversion efficiency, the material with 1.9 – 2.4 eV band-gap should be required to achieve DOE target hydrogen fuel cost as discussed in 1.3.[23]

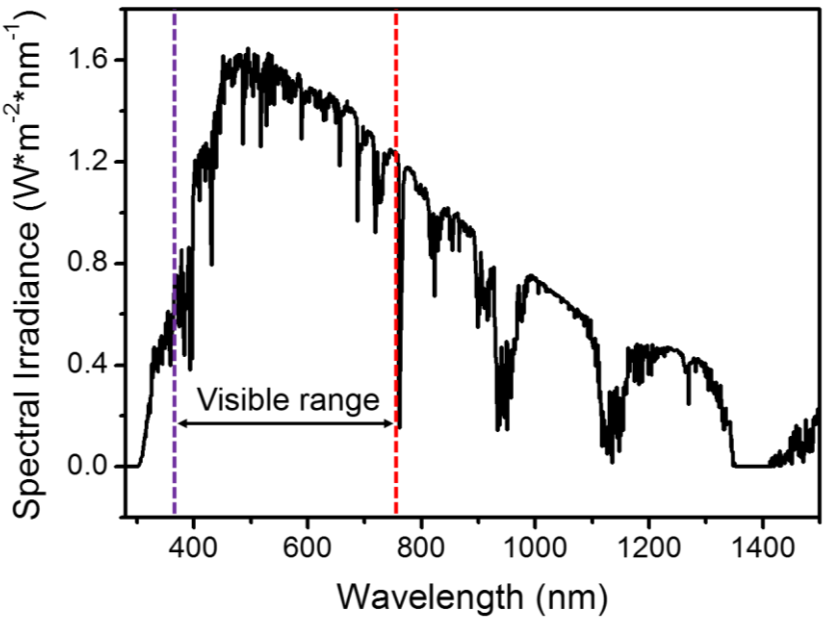

Figure 1.11. Solar spectrum (AM 1.5 G). The visible light range from 380 – 750 nm is indicated dotted vertical lines.

.

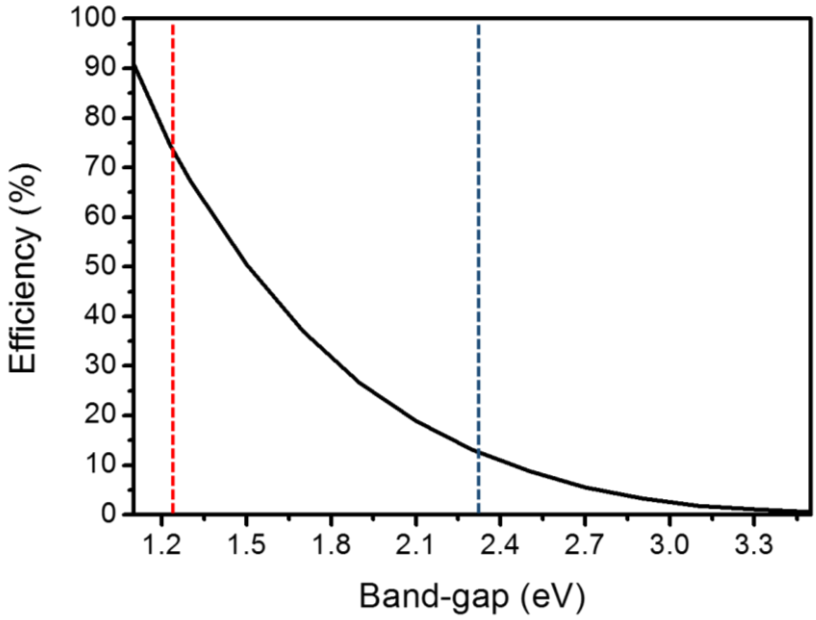

Figure 1.12. The relationship between STH efficiency and band-gap value. Red dotted line indicates minimum band-gap (1.23 eV) for water-splitting. Blue dotted line is for the band-gap of 3C-SiC (2.3 eV).

As indicated in Section 1.5.2, H_2 evolving potential (HEP) and O_2 evolving potential (OEP) are important for water-splitting. It is easily explained by comparing the level for band-edge structure of semiconductor and each potential. Figure 1.13 presents the band-edge structure of some representative semiconductors. According to the consideration about band-gap for water-splitting, a band-gap, 2.3 eV of Fe_2O_3 is suitable. The conduction band-edge of Fe_2O_3, however, is more positive than HEP (0 V vs. SHE). In this case, additional applied bias is needed to increase the band-edge. In short, conduction and valance band-edge have to be located at more negative and positive than HEP and OEP, respectively. Although GaN has a perfect band-structure to drive the water-splitting and even CO_2 reduction, it has

too large band-gap, 3.4 eV which limits the absorption of solar spectrum. Currently, there are few materials satisfying both requirements of band-gap and band-structure. Under these fundamental necessary conditions, efficient carrier transportation has to be achieved to drive electrochemical reaction for chemicals. Importantly, the semiconductor should be chemically stable because the reaction site is in aqueous solution. The environmental variation is fairly severe in PEC process caused by light illumination and chemical bias. It is the most important and necessary requirement for commercial usage in the future. Finally, the minimization of cost of the photo-electrode fabrication has to be considered for commercialization. Therefore, it is crucial issue to use and develop the suitable semiconductor materials for photo-electrode application.

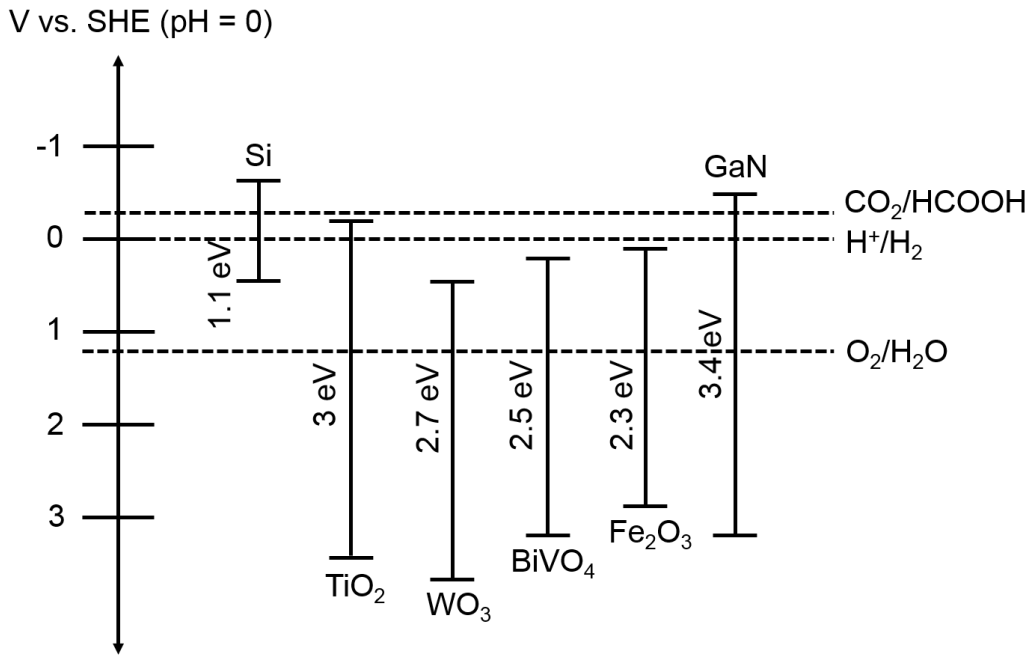

Figure 1.13. The band-edge structure of several semiconductor.

1.6 Review of previous researches

Since the TiO_2 photo-electrode as the beginning of PEC, many researchers have been investigated for improvement of the performance of photo-electrode. In broad terms, the type of materials can be divided to oxide-based semiconductors and inorganic semiconductors. Relatively, oxide-semiconductors have an advantage of durable property against PEC reaction. However, it has some drawbacks such as large band-gap and unsuitable band-position according to the materials.[15, 24-26] Especially, TiO_2 as the landmark of this research has been progressed with many approaches. Above all, it has a limitation for solar-spectrum with band-gap of 3.2 eV. So, band-gap engineering with chemical doping and combination with other narrow band-gap semiconductors has mainly studied.[25, 27-29] Representatively, R. Asahi *et al*. have developed the nitrogen-doped titanium oxides for visible-light absorption.[28] H. Cui *et al*. have prepared hydrogen doped titanium (black TiO_2) in nanotube arrays for improvement of solar absorption and charge transport.[27] On the other hands, other oxide semiconductors such as $BiVO_4$ and WO_3 do not have proper conduction band-edge.[26, 30] Hetero junction and nonporous structures have been investigated for improvement mechanism of PEC performance with these materials, it is theoretically limited for practical water-splitting without assistance of external bias.[31] In the case of inorganic semiconductors, Si has a very narrow band-gap of 1.1 eV which is the best for absorb solar-spectrum. However, we reviewed water-splitting requires 1.23 eV at least in thermodymic viewpoint. Also, it is very unstable in the aqueous solution. Accordingly, the method of surface passivation has been progressed. M. J. Kenneny et al proposed ultrathin nickel films passivation for Si photoanodes.[32] Therefore, it also needs hetero-structure for realization of water-splitting under ideal condition.[33] In contrary to Si, GaN which is wide band-gap semiconductor has been recently

focused due to its applicable band-structure for water-splitting and CO_2 reduction.[34, 35] Especially, there are few materials to satisfy the potential for CO_2 reduction.[35, 36] Despite of the potential for CO_2 reduction with GaN, band-gap engineering is also needed due to the wide band-gap of 3.4 eV for effective solar absorption.[34, 37] M. Deguchi *et al*. utilized the piezoelectric effect by using AlGaN/GaN hetero-structure for better charge separation.[38] As the stability issue, T. Hayashi et al. reported the improved life-time of GaN with NiO co-catalyst on surface preventing the surface dissolution.[37] In the broad review of the recent researches, solar-spectrum absorption has been considered as the most important issue for achieving practical device in common regardless of material type. However, it is self-limited by the property of material itself, band-gap. For inorganic semiconductor, stability problem has to be solved with passivation. In addition, a lack of the materials for CO_2 reduction with efficient solar absorption is one of the issues for actual artificial photosynthesis. In this context, the development of new promising material with both effective solar-light absorption and band-edge condition is required for practical device.

1.7 Research objectives

As reviewed about the requirements for semiconductor materials as photo-electrode, the choice of material are very important to aim the high performance photo-electrode. Although many researchers have proposed to overcome essential limitation of various materials, it is still far to achieve a practical level. The objectives of this thesis are divided into three parts. (1) The evaluation of SiC semiconductor for the application as photo-electrode for water-splitting and CO_2 reduction. As the choice of materials, silicon carbide (SiC) semiconductor is utilized due to its suitable property of band-structure for this

application. In the types of SiC, cubic type of SiC (3C-SiC) semiconductor has a band-gap of 2.3 eV considered as the most appropriate value. Despite of its attractive property for photo-electrode, the PEC performance of 3C-SiC has not been understood clearly. Therefore, it is necessary to demonstrate basic property of SiC. (2) The improvement of the solar-conversion efficiency and stability of SiC photo-electrode. Some strategies to overcome the limitations of 3C-SiC will be proposed. Especially, the proposed efforts are focused on overpotential to drive the water-splitting at the interface between 3C-SiC and electrolyte and electrochemical surface oxidation of SiC. (3) The realization of PEC CO_2 reduction system with 3C-SiC photo-electrode. The analysis of gas products from CO_2 reduction will be demonstrated. In summary, we have started this research from understanding on the basic properties of 3C-SiC including limitations as photo-electrode to development.

1.8 Thesis outline

This dissertation has total 7 chapters started from the research background and essential theory in Chapter 1. In Chapter 2, the experimental method which was mainly used in this research will be presented. The core topic in this thesis, 3C-SiC, will be introduced in Chapter 3. In this chapter, we will show the basic PEC properties and limitations of SiC photo-electrode for water-splitting and CO_2 reduction. Then, the future prospective will also presented here. From Chapter 4 to Chapter 5, the researches about Pt particle effect on the surface of 3C-SiC and epitaxial graphene layer fabricated on 3C-SiC will be discussed as the pathways to overcome the limitation of 3C-SiC. In Chapter 6, PEC CO_2 reduction by light-generated carriers 3C-SiC will be presented. Finally, the general conclusions of this work and some suggested future work will be shown in last Chapter 7.

Chapter 2
SiC semiconductor and Experimental methods

2.1 Cubic type of Silicon Carbide (3C-SiC)

2.1.1 The characteristic of 3C-SiC semiconductor

The SiC is classified by their different crystal structures called polytypes.[39] Although the SiC polytypes basically consist of silicon (Si) and carbon (C) atoms at a ratio of 50 %, over 100 polytypes exist according to the combination of arrangement for Si and C in SiC crystal lattice. However, a few polytypes of SiC such as 3C-SiC, 4H-SiC, and 6H-SiC which are shown in Figure 2.1 are the most commonly utilized for the electric semiconductor device. The difference among the polytypes of SiC comes from the stacking sequences of Si-C bilayers as shown in Figure 2.2. The structure of sequence is simply expressed with the letters ABC, ABCB, and ABCACB for 3C-, 4H-, and 6H-SiC, respectively. That is, the number of letters decides the name of polytype. Also, the other difference is determined by crystal lattice structure illustrated in Figure 2.3. While 4H- and 6H-SiC have a hexagonal lattice structure, 3C-SiC is only the form of a cubic crystal structure. According to this difference of structure, each SiC polytype shows a distinct characteristic as a semiconductor. The physical and electric properties of the most common SiC polytypes are described in the Table 2.1 in comparison with one of the Si. SiC is wide band-gap semiconductor and it has been generally considered as suitable material for the power device application due to their superior properties such as high breakdown electric field and thermal conductivity as compared to silicon-based device.[40] On the other hand, a band-gap value of the 3C-SiC, 2.3 eV is relatively smaller than others within SiC. It is more efficient for 3C-SiC to absorb the visible light range (~ 540 nm) in solar-spectrum as compared to 4H- (375 nm) and 6H-SiC (413 nm). Therefore, it has been regarded as material for solar-driven water-splitting and the photovoltaic and optical devices with some excellent electric properties.[41-43] In addition, the 3C-SiC is only

polytype that can be grown on the Si substrate heteroepitaxially due to the same crystal structure with Si and stability at low temperature during growth process.[44] Thus, it is possible to fabricate the 3C-SiC on large scale substrate. In this case, however, the mismatch of lattice constant (20 %) and the difference of thermal expansion coefficients causes a poor crystalline quality with many defects.[45]

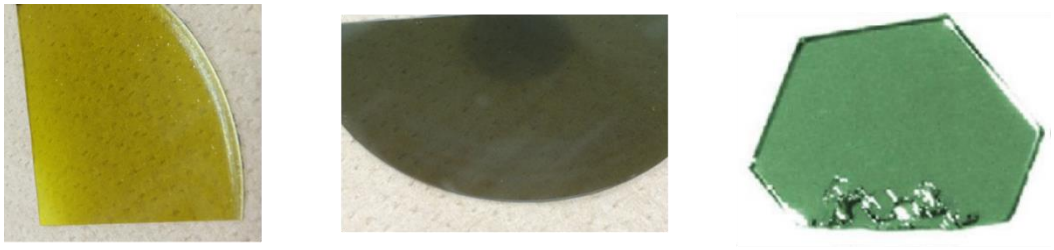

Figure 2.1. The photos of (a) 3C-, (b) 4H-, and (c) 6H-SiC wafers. (Adapted from the reference 40, partially)

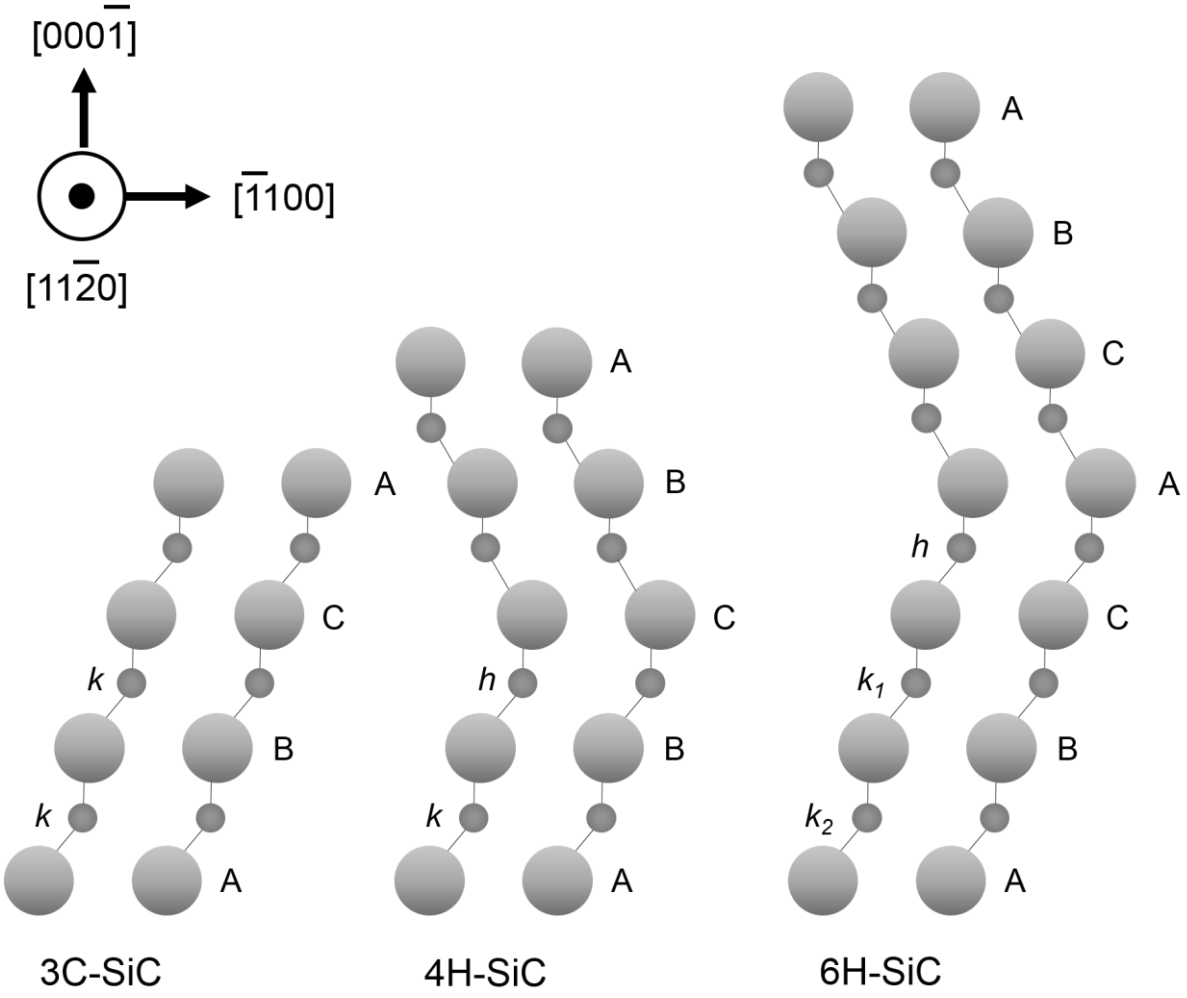

Figure 2.2. The stacking sequences in SiC viewed in the [1120] plane. The cubic and hexagonal symmetry points are defined as *k* and *h*, respectively. (Adapted from the reference 40)

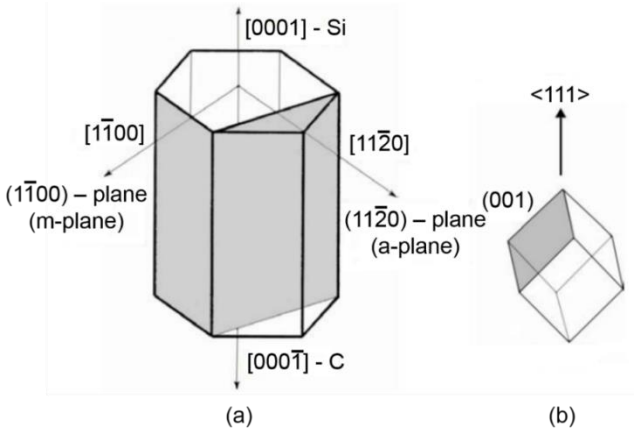

Figure 2.3. The (a) hexagonal and (b) cubic lattice structures of SiC. (Adapted from the reference 40)

Table 2.1. Physical and electric properties of the representative polytypes of SiC and Si.[46]

	3C-SiC	**4H-SiC**	**6H-SiC**	**Si**
Stacking order	ABC	ABCB	ABCACB	-
Crystal structure	Cubic	Hexagonal	Hexagonal	Cubic
Large area growth	○ (on Si)	Difficult	Difficult	○
Lattice constant (Å)	4.34	a = 3.073 c = 10.053	a = 3.08 c = 15.117	5.43
Dielectric constant, ε	9.72	9.66	9.66	11.7
Band-gap (eV)	2.3	3.3	3.0	1.12
Electron mobility, μ_n ($cm^2\ V^{-1}\ s^{-1}$) (at 300K)	≤ 1000	≤ 850	≤ 450	≤ 1400
Hole mobility μ_p ($cm^2\ V^{-1}\ s^{-1}$) (at 300K)	≤ 40	≤ 120	≤ 100	≤ 450
Thermal conductivity (W cm^{-1} ℃$^{-1}$)	3-4	3-4	3-4	1.3
Critical breakdown field strength, E_c (MV cm^{-1})	2	3	3	0.3

2.1.2 The heteroepitaxial growth of 3C-SiC

Due to the lattice mismatch between 3C-SiC and Si, planar defects are generated during epitaxial growth process. In order to remove the planar defects, the epitaxial 3C-SiC growth on the undulant-Si surface (001) substrate was proposed.[47] When a growth of specific domain is proceeded in the [110] direction, the adjacent domain should expand in the $[\bar{1}10]$ direction. This domain expansion has to be controlled to enhance the growth in a specific direction. The principle of domain expansion control with undulant structure of Si is shown in Figure 2.4(a). The sequence of fabrication process is shown in Figure 2.4(b). First, the surface of Si wafer is manufactured to undulant structure. Crystal defects originated from this process are mitigated by oxidizing the surface at 1100 ℃ in a dry-oxygen stream. Then, 200 nm oxidized layer in thickness is removed by HF solution. For the growth of 3C-SiC, a cold-wall-type, low-pressure chemical vapor deposition (LPCVD) was employed with a temperature of 1350 ℃. Before the growth process, the surface is carbonized in a flow C_2H_2 and H_2 to improve the crystal quality by forming thin 3C-SiC which accommodate the mismatch between 3C-SiC and Si. Then, 200 μm thick 3C-SiC epitaxial layer is grown and obtained by removing the Si substrate. Finally, 3C-SiC wafer is prepared after polishing treatment. For this research, the 3C-SiC wafers prepared in this method was donated by Hoya company.

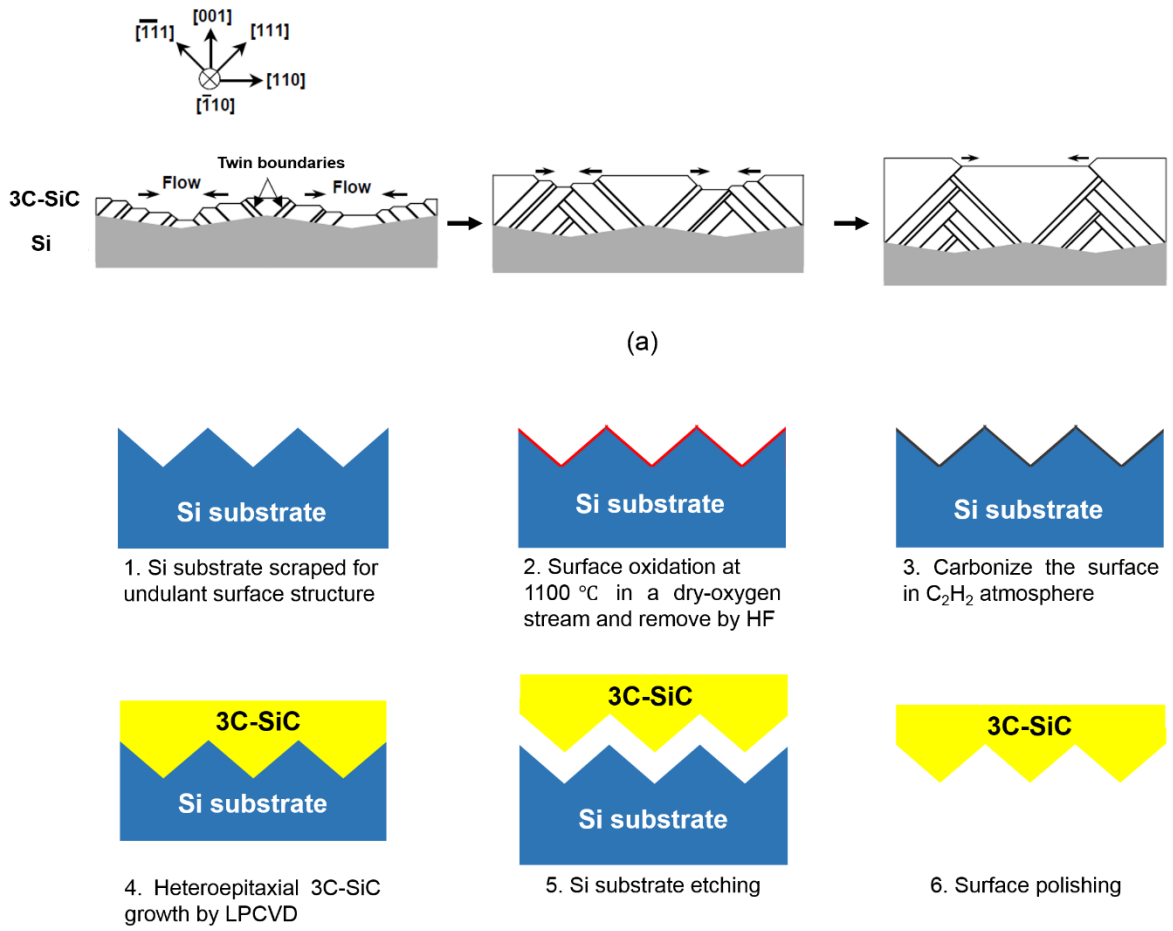

Figure 2.4. (a) The principle to reduce planar defect of 3C-SiC on Si substrate. (b) The fabrication process of 3C-SiC on Si wafer. (Partly adapted from the reference 47)

2.2 The analysis technique for electrochemical properties

2.2.1 The configuration of PEC cell

The PEC cell was designed to measure the characteristic of photo-electrode in various condition as shown in Figure 2.5. In this configuration, the prepared 3C-SiC photo-electrode is working electrode (W.E). As a counter and a reference electrode (C.E and R.E), the platinum wire (Pt) and Ag/AgCl (in saturated KCl) were used, respectively. These three electrodes were immersed in aqueous solution. As an aqueous solution, three types of electrolytes, 0.01 M HCl (pH 1.12), 0.1 M $KHCO_3$ (pH 8.36), and 0.1 M NaOH (pH 12.84) were prepared for different pH condition. Then, each electrodes are connected to the potentiostat (Princeton Applied Research VersaSTAT 3). For the light illumination on the photo-electrode surface, a 500 W Xe lamp (USHIO Optical ModuleX) and quartz window were employed as the light source and to minimize a loss of light power.

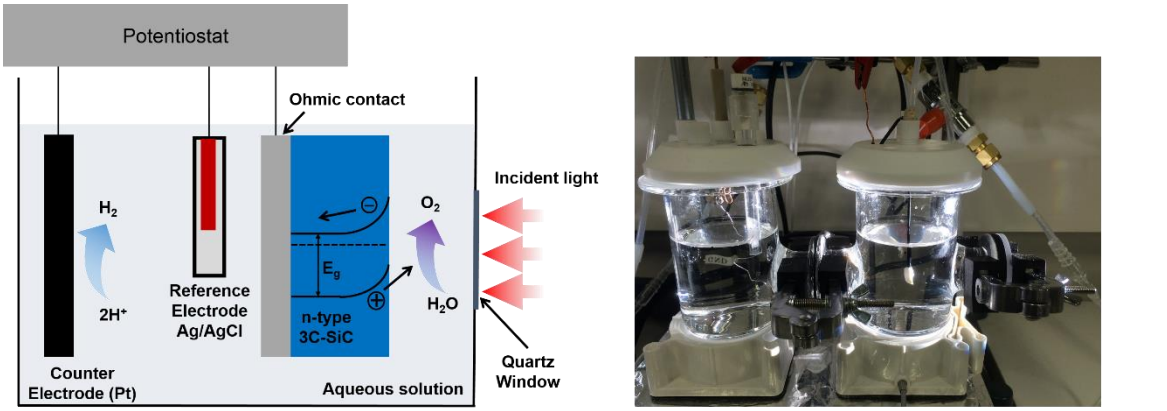

Figure 2.5. The basic composition of PEC cell for measurement.

In contrary to the general electrical measurement, the ground level cannot be considered as reference for the potential expression in the liquid state. Therefore, it is necessary to introduce a stable R.E. The potential of R.E is known in designated aqueous solution. As shown in Figure 2.6(a), the current through the W.E and C.E is recorded according to the potential difference between W.E and R.E. Ag/AgCl (in satd. KCl) reference electrode which is used in this research is the most common type due to the simplicity. The electrode reaction between electrode and electrolyte is as follows.

$$AgCl\ (s) + e^- = Ag\ (s) + Cl^- \quad (2.1)$$

This electrode potential in saturated KCl is almost 0.2 V relative to the standard hydrogen electrode (SHE) at room temperature. This three electrode system is applied to most photoelectrochemical analysis in this research. On the other hand, two electrode configuration without R.E in Figure 2.6(b) is a simple tool to evaluate the photo-electrode under only light illumination without an external bias or analyze the gas products as the PEC reaction between W.E and C.E.

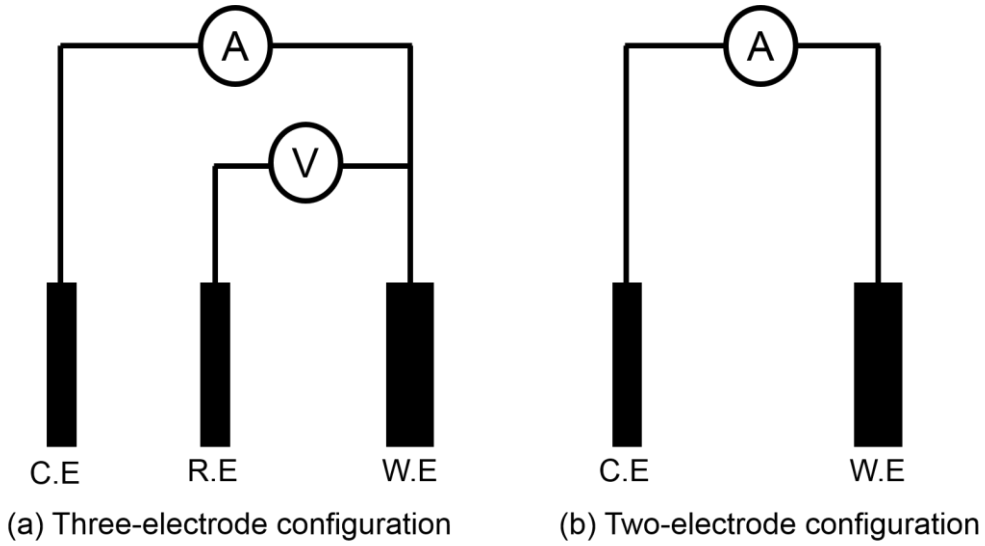

Figure 2.6. The type of electrode configuration for electrochemical measurement.

2.2.2 Cyclic Voltammetry method

Cyclic Voltammetry (CV) is a representative electrochemical measurement technique of the current in an electrochemical cell by controlling the potential cyclically. Figure 2.7(a) shows the transition of applied potential with time. The applied potential is swept from an initial potential (E_i) to a final potential (E_f) within two cycles. Figure 2.7(b) shows an example of the current observation during one cycle. In this graph, positive current indicates the oxidation reaction process while negative direction represents the reduction reaction. Many kinds of information such as redox potential of reactants and diffusion constant can be obtained with the CV measurement. In this study, CV method provides the current variation with and without light illumination on the photo-electrode surface and a turning-on point of potential to increase the amount of photocurrent. As a guide, photocurrent curve against potential will be generally expressed with the result of only a direction in one cycle in this thesis.

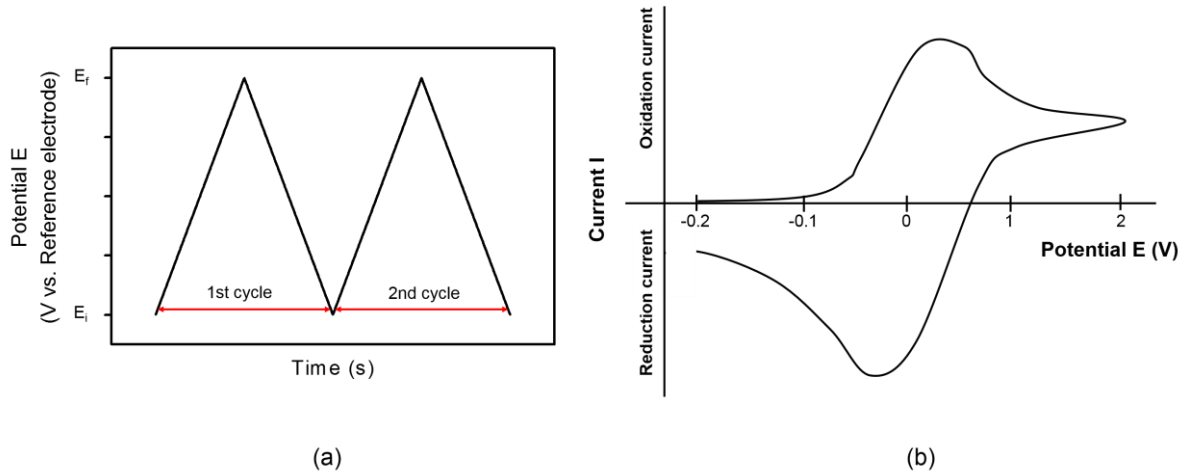

Figure 2.7. The transition of (a) potential in electrochemical cell during cycle voltammetry process, (b) Current curve according to the potential sweeping.

2.2.3 Chronoamperometry method

Chronoamperometry method is a technique to observe the current flow at a fixed applied potential. As shown in Figure 2.8(a), the initial potential in the electrochemical cell changed to the step potential (E_s) at t_0. After change, E_s is kept for the designated time (τ). The recorded current flow with the time is expressed in Figure 2.8(b). At t_0, current is temporarily overshot due to the charge of double layer between the electrode and electrolyte. This component of current is called to non-faradaic current because it does not accompany the exchange of electrons. (It is just caused by the movement of very small minority of ions.) That is, the faradaic current (actual current flow) is flowed from around t_s. This method is utilized as the stability examination of photo-electrode while comparing the current level with lasting the time.

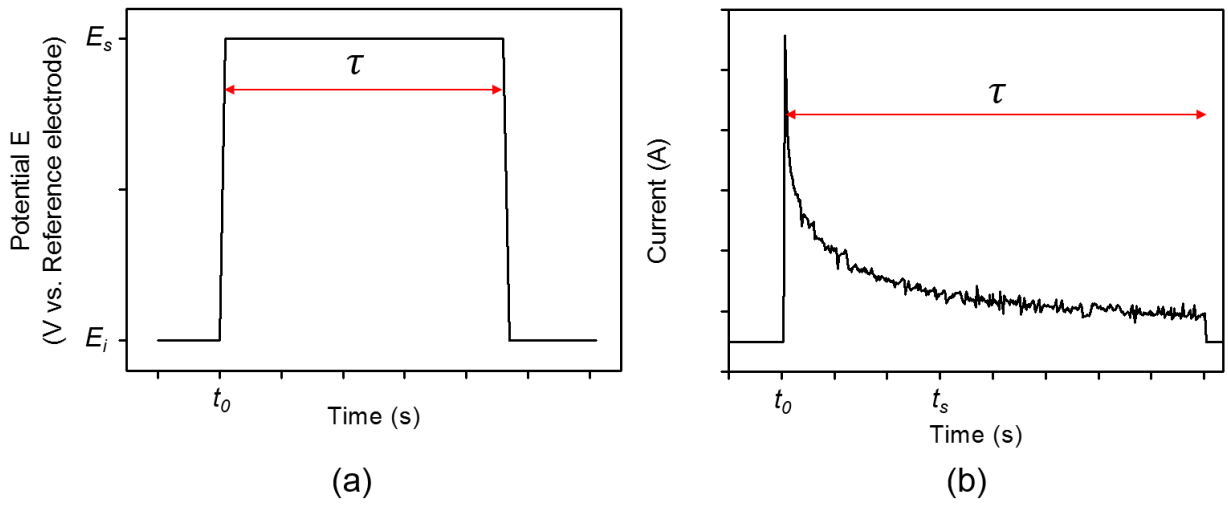

Figure 2.8. The transition of (a) potential in electrochemical cell of chronoamperometry method, (b) current flow with the elapsed time.

2.2.4 Electrochemical Impedance Spectroscopy (EIS)

Electrochemical impedance spectroscopy (EIS) is the tool to analyze the impedance of the electrochemical cell by applying the small AC signal. The impedance analysis is performed with the design of equivalent circuit which is representing the system. The equivalent circuit generally consist of the resistors and capacitors. From an obtained impedance spectrum (Form of Nyquist and Bode plot), it is possible to deduce the value of components in the equivalent circuit through the curve-fitting analysis. For the impedance analysis of SiC photo-electrode, the simplest equivalent circuit can be adopted as shown in Figure 2.9(a). This is a series network of one resistance (R_s) and a parallel capacitance (C_{sc}) and resistance (R_{sc}). Parallel component (R_{sc} and C_{sc}) represents a resistance and a capacitance in the space charge region of SiC photo-electrode. The R_s indicates the whole series resistance including one of the solution. The Nyquist plot of this equivalent circuit is exhibited in Figure 2.9(b). By this technique, the capacitance value of SiC photo-electrode is estimated to draw the Mott-Schottky plot which will be discussed in Section 3.3.1.

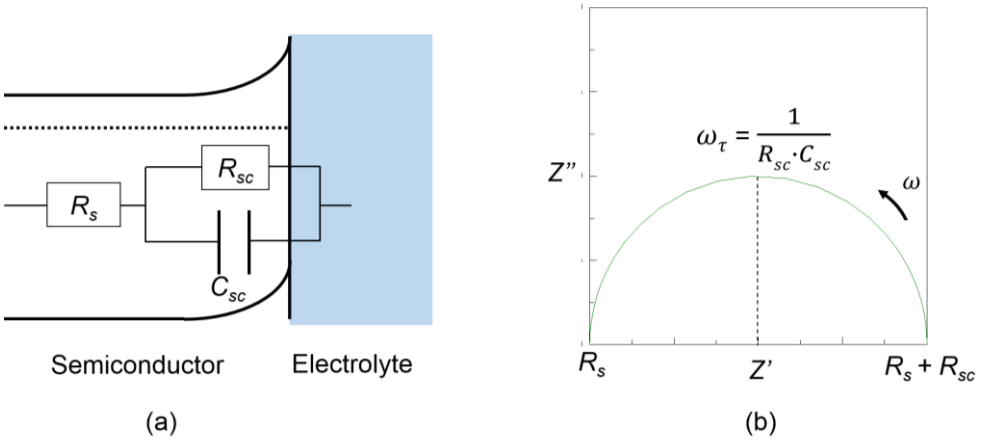

Figure 2.9. (a) The equivalent circuit of semiconductor photo-electrode in the electrolyte, (b) The Nyquist plot of this equivalent circuit. The both ends point of semi-circle refer to R_s and R_s+R_{sc}, respectively. A reciprocal of time constant (R_{sc} C_{sc}) points out the center of semi-circle line.

2.2.5 Gas chromatography system

Gas chromatography (GC) is the instrument to analyze components of a target gas which has mixed contents. Figure 2.10 shows the schematic structure of gas chromatography. As the analysis process, each components in the target are firstly vaporized by applying heat at the injection part. The vaporized components are transported into a column by carrier gas. Each transported component is separated in the column. The detector located at the last part of column recognizes the quantity of each component and change into electric signal. Finally, the component and quantity are expressed as the signal peak with retention time. Here, the important option for GC is the types of column and detector which determines detectable gas type and detectivity. Representatively, there are thermal conductivity detector (TCD), flame ionization detector (FID) as detector. The column is classified according to the material of them (Molecular Sieve or PLOT Q).

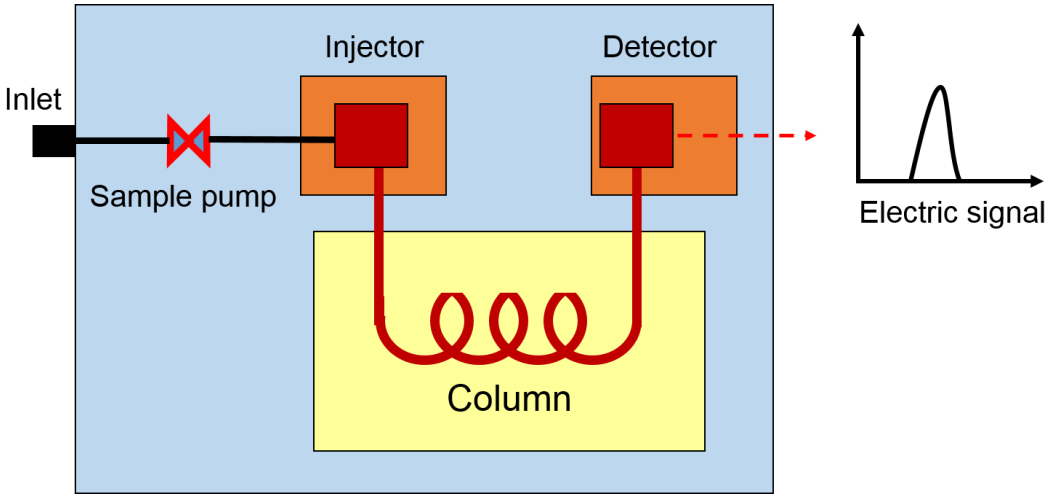

Figure 2.10. The structure of gas chromatography system.

The quantity of gas sample is analyzed by comparing the peak area of the electric signal with the measurement of standard gas. Figure 2.11 is the method for quantitative analysis. Because target component (H_2 gas in this example) is displayed in a fixed time, the ratio of peak for samples and standard gas at same retention time can be obtained. Then, the concentration of sample is calculated.

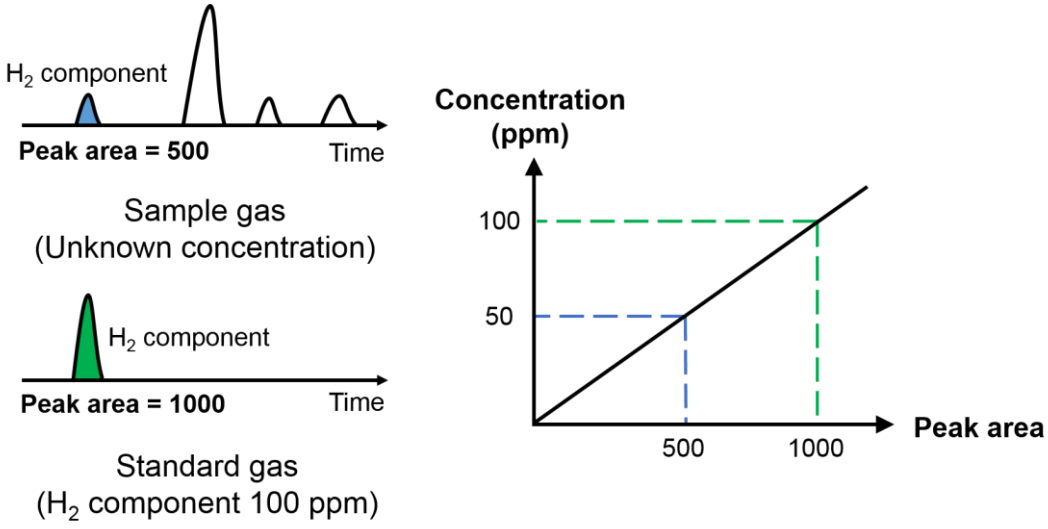

Figure 2.11. Quantitative analysis method for sample of unknown concentration.

The GC utilized in this research (Micro-GC 3000, Inficon) is equipped with TCD and the column produced with molecular sieve material. The detectable gas components are hydrogen (H_2), oxygen (O_2), nitrogen (N_2), methane (CH_4) and carbon monoxide (CO). The carrier gases are argon (Ar) for H_2 and helium (He) for the other except for H_2. The most advantages of this GC enables the time-dependent gas analysis with the characteristics described in Table 2.2. In the contrary to conventional GC, micro GC has minimized components such as injector and detector fabricated by microelectromechanical system (MEMS). In addition to the reduction of the instrument size with MEMS technology, narrower capillary columns combined with the detector properly provides rapid analysis and

high detectivity.[48] Most of all, syringe sampling is not required to inject a gas to GC. Due to the abilities of micro GC, we organized the PEC in direct connection to the injection part with gas flow valve for time-dependent measurement as shown in Figure 2.12(a). An example for H_2 gas detection is in Figure 2.12(b). After collecting H_2 gas produced from the PEC reaction between C.E and W.E, the measurement is started by opening the valve. Figure 2.12(b) is the result of sampling for 5 times without gas sampling pump. The analysis process for one sampling takes about 1 min. Because the gas diffuses from PEC cell to GC for a few minutes, the concentration of produced hydrogen increases after 3 min rapidly. In this way, time-dependent gas production analysis is possible during the process of PEC reaction. The analysis with micro GC system was performed for H_2 gas generation and CO_2 reduction with SiC photo-electrode.

Table 2.2. The comparison of conventional and micro GC system.[48]

Type of GC	Injection method	Detect limitation	Analysis time
Conventional GC	Syringe sampling	~ 10 ppm	10 min – 1 hour
Micro GC	Direct connection	2 ~ 3 ppm	30 s – a few min

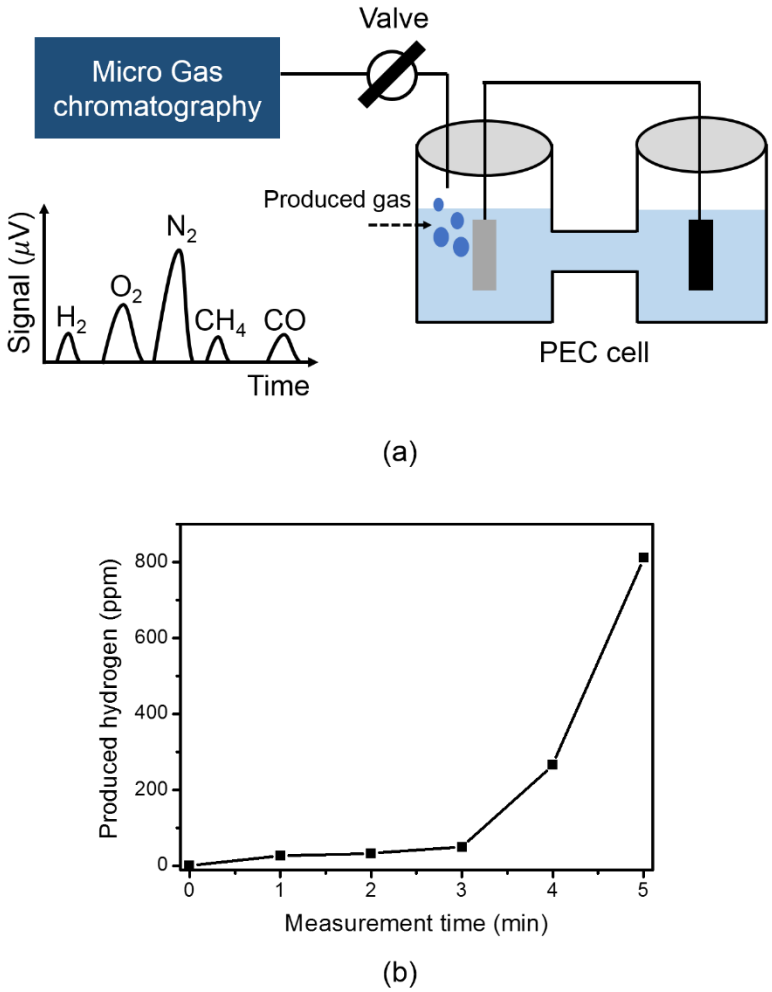

Figure 2.12. (a) Micro gas chromatography system in connection with PEC cell, (b) graph of example for H_2 gas measurement with time.

2.3 The evaluation of surface characterization

2.3.1 Atomic force microscope (AFM)

The AFM is the most common atomic microscope which can observe the surface characteristic in nano-size. This technology can analyze the surface roughness by scanning the surface with cantilever fabricated with micromachining. The common size is 100 μm × 10 μm × 1 μm (length × width × thickness). This very small cantilever can be bent by tiny force. The principle is explained with structure of AFM in Figure 2.13. As the cantilever approaches to the surface of sample, the attraction and repulsive force is interacted between the tip of cantilever and sample surface. At that time, photodiode can measure the reflected laser with changed angle. A cantilever movement of at least 0.01 nm is detectable in this method. Finally, topography for the sample is displayed as the result. The instrument of AFM (SPM-9700, Shimazu) is used in this work to investigate the Pt particle formation of the SiC surface.

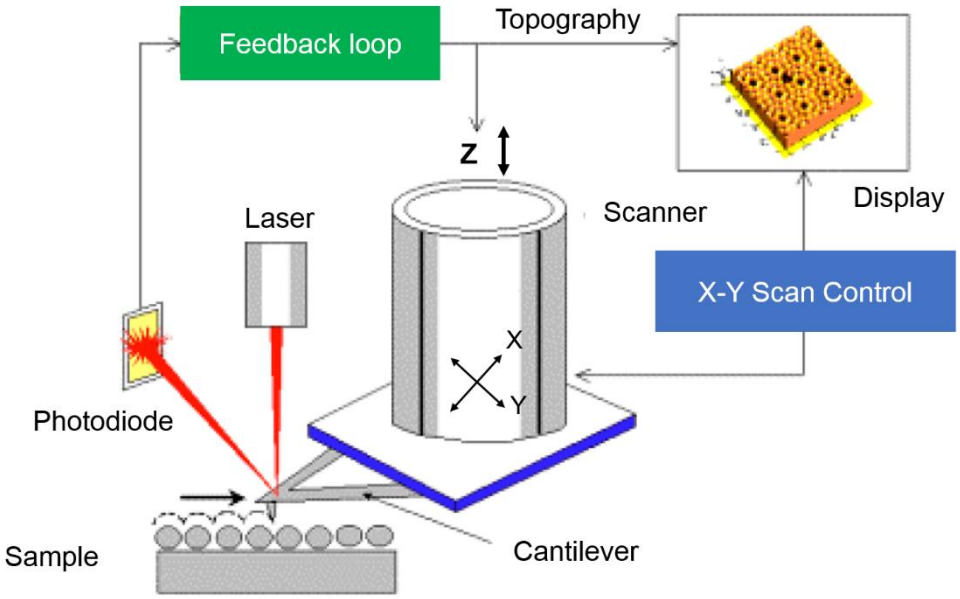

Figure 2.13. The schematic of structure for AFM. (Adapted from the reference 49)

2.3.2 Raman spectroscopy

Raman spectroscopy is a technique to probe the vibrational property by measuring the energy shift from the original incident light. An incident laser onto the sample surface is reflected off without change. A few proportion is scattered by interacting with the molecules of surface. This scattered light which is known as Raman effect is collected and provide a spectrum. The spectrum has unique characteristic associated with the material and can be considered as a fingerprint to identify the material. Raman spectroscopy allows non-destructive analysis of the materials such as solids, powders, liquids and gases with fast time. Figure 2.14 shows the actual image and schematic of Raman spectroscopy equipped with laser of 532 nm (inVia Raman spectroscopy) set-up utilized in this research. We used this instrument to investigate the surface state according to the Pt particle formation with different temperature in Chapter 4. Also, it is mainly focused on the graphene formation on the SiC photo-electrode in Chapter 5.

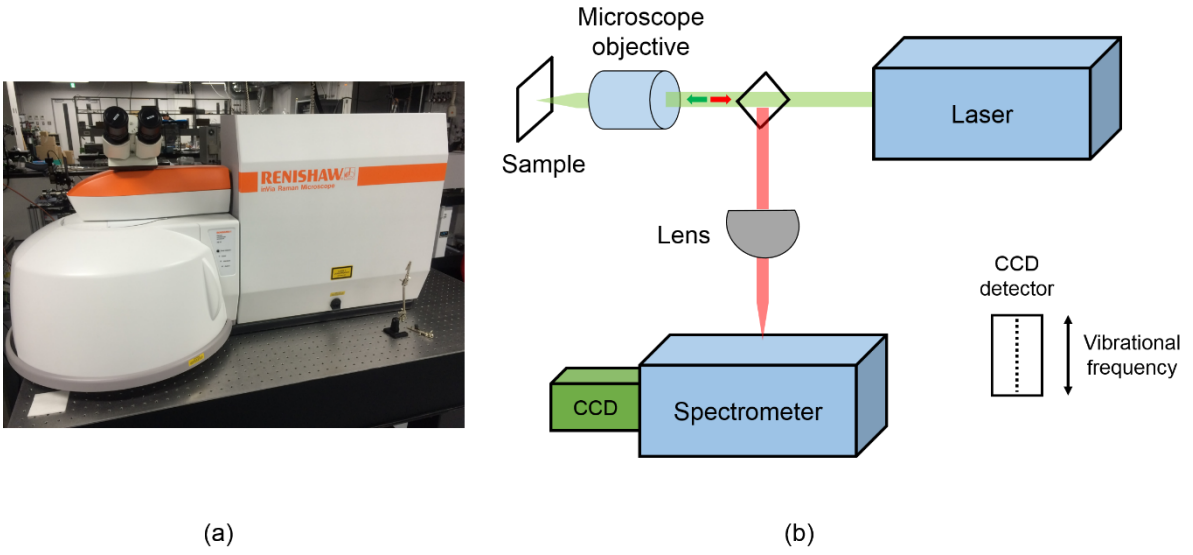

Figure 2.14. (a) Actual photo of Raman spectroscopy instrument used in this work, (b) The diagram of the instrument set-up. (Adapted from the reference 50)

2.3.3 X-ray photoelectron spectroscopy (XPS)

X-ray photoelectron spectroscopy (XPS) is a spectroscopic technique by x-ray in high vacuum chamber to analyze the chemical compounds of a sample surface. The principle is shown in Figure 2.15. It is based on simple two processes with the interactions between x-ray and electrons. First, incident x-ray collides inside electron located at core. The collided electron is ejected from the electronic shell with a kinetic energy (E_{kin}) related to the binding energy (E_b) in the atom. Secondly, the missing place in core part means an unstable hole. From the valance shell, an electron fills this hole to compensate energy. In these process, E_b is expressed as following equation.

$$E_b = h\nu - E_{kin} - W_f \tag{2.2}$$

where h is plank's constant and ν is the frequency of the incident x-ray. W_f is a work function dependent on both spectrometer and material. Through these two processes, the binding energy of the elements in the target sample can be obtained and used to distinguish the components. In this research, we investigated the surface of SiC with Pt particle according to the reaction of Pt and Si atom by the annealing process in Chapter 4.

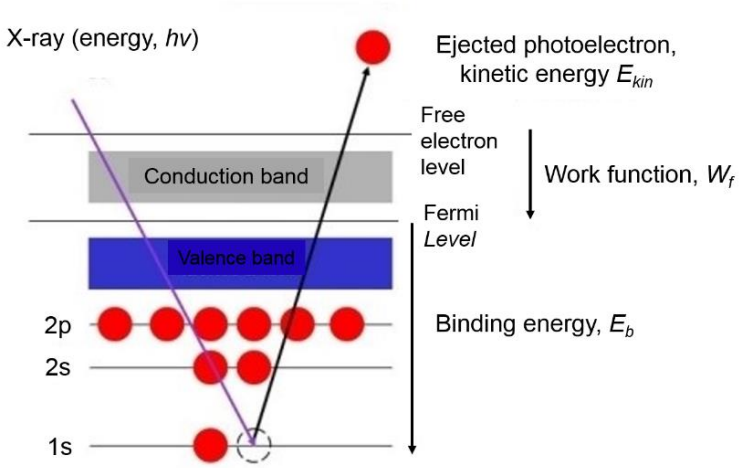

Figure 2.15. The principle of XPS. (Adapted from the reference 51)

Chapter 3
Fundamental property of SiC as photo-electrode and current limitations

Chapter 3. Fundamental property of SiC as photo-electrode and current limitations

3.1 Introduction

As reviewed in Chapter 1, the application of PEC water-splitting and CO_2 reduction requires the promising semiconductor material which has available band-structure in the viewpoint of electrochemical potential and proper band-gap to utilize the solar-light spectrum efficiently. Herein, cubic type silicon carbide (3C-SiC) attracts attention with its wide band-gap, 2.3 eV as the photo-electrode. However, few reports on PEC properties for this application have been found previously.[42, 52, 53] In this chapter, the 3C-SiC semiconductor is evaluated as photo-electrode for artificial photosynthesis with discussion about the current limitation lowering performance.

3.2 Photo-electrode sample fabrication

The n-type 3C-SiC wafers (with a lightly (1.0×10^{16} cm^{-3}) and highly (3.6×10^{18} cm^{-3}) nitrogen doping concentration) were prepared for the photo-electrode. For the comparison n-type 4H-SiC (2.18×10^{16} cm^{-3} nitrogen doping density) with an epitaxial layer of 8 μm in thickness on 4H-SiC substrate. Here, nitrogen is the dopant for both 3C-SiC and 4H-SiC. The wafers were separated to the form of small pieces in the size of from 5 mm^2 to 10 mm^2. These prepared pieces were cleaned by acetone and isopropyl alcohol (IPA) with ultrasonic agitation equipment to remove organic contaminants and some unnecessary particles for 5 minutes in each solvents. Then, the native oxide layer was etched by 100:1 mixture of deionized (DI) water:hydrofluoric acid (HF) for 5 minutes. In order to form the Ohmic contact, the aluminum (Al) layer 200 nm or aluminum (Al)/gold (Au) layer 200 nm in thickness was deposited by sputtering on the backside of the samples. Metal-deposited

sample was sintered at 600 ℃ under Ar at a pressure of 10 kPa for 10 minutes for better contact. Then, the copper (Cu) wire was attached on the Ohmic contact layer with silver paste, and the back and sides of the SiC sample piece were covered by the adhesive (Cemedine Super X 8008) which is stable during the PEC reaction for insulation. The exposed part of Cu wire in the solution is protected by rubber insulator. In Figure 3.1, the cross-sectional diagram of the completed sample is shown with real photos.

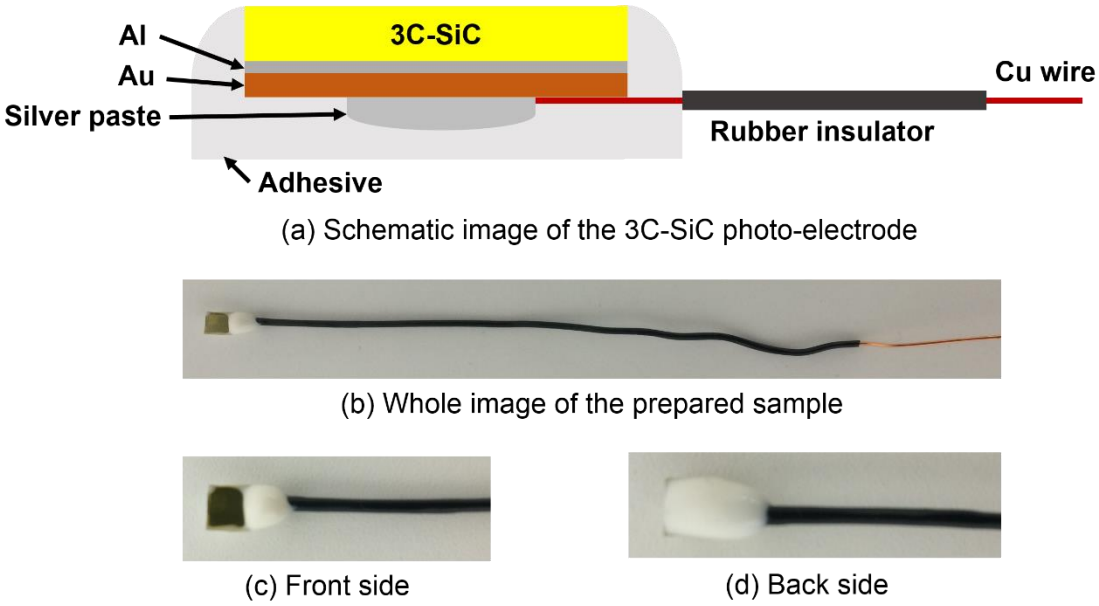

Figure 3.1. Completed SiC photo-electrode sample.

3.3 Prospective of SiC semiconductor as photo-electrode

3.3.1 Basic properties of 3C-SiC towards artificial photosynthesis

As discussed about the condition of semiconductor material for water-splitting and CO_2 reduction in Section 1.5.3, there are few materials which satisfy two necessary conditions of the enough potential to raise the water-splitting reaction and absorption of visible light range previously. In this section, the basic properties of 3C-SiC semiconductor is evaluated as photo-electrode. First, absorption spectrum is investigated by UV-Vis spectrometer (Shimizu UV-3150) in Figure 3.2. It is confirmed that 3C-SiC (lightly doped (1.0×10^{16} cm^{-3}) sample) can absorb the light with wavelength shorter than 545 nm corresponding to energy, 2.28 eV which is almost same with the band-gap (2.3 eV). Here, the range below 545 nm is considered as effective range for light absorption.

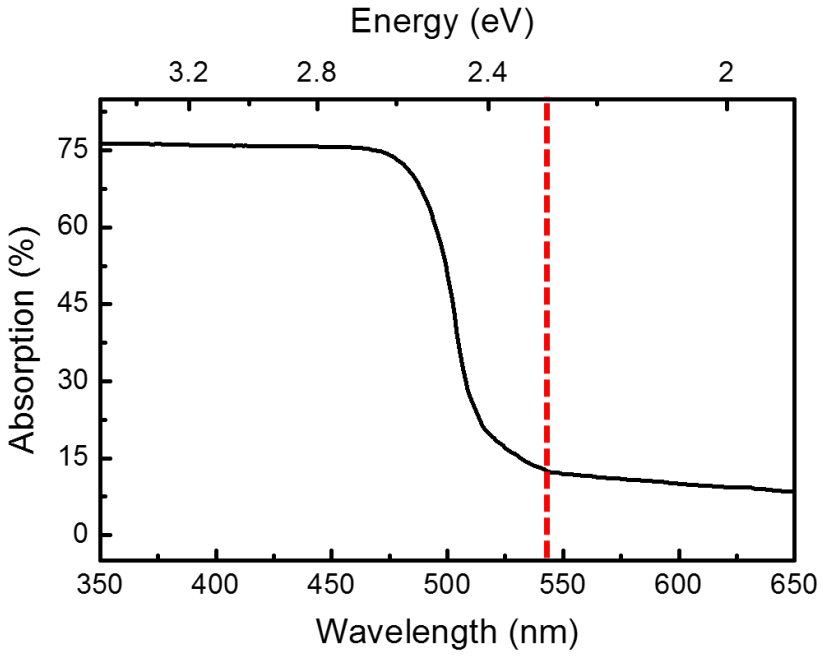

Figure 3.2. Absorption spectrum of the 3C-SiC sample. Red dotted line indicates the threshold energy for band-gap transition, 545 nm (2.28 eV).

Chapter 3. Fundamental property of SiC as photo-electrode and current limitations

In order to demonstrate the band-structure of 3C-SiC which is important to show the possibility of water-splitting and CO_2 reduction with solar-light energy, impedance measurement was performed to obtain the Mott-Schottky plot. Figure 3.3(a) shows the band energy scheme of n-type SiC with various condition of an applied bias. The direction of band-bending changes based on the flat-band potential (V_{FB}). By controlling the applied voltage less and more than V_{FB}, the impedance of 3C-SiC photo-electrode was measured in the frequency range from 0.1 Hz to 20 kHz. Figure 3.3(b) is a Mott-Schottky plot for n-type 3C-SiC obtained from -2.6 to -0.7 V (vs. Ag/AgCl) in the electrolytes of pH 1.12, 8.36 and 12.84. We applied the equivalent circuit which consists of the series resistance (R_s), depletion region resistance (R_{sc}) and capacitance (C_{sc}) as shown in Figure 2.9(a). The intercept points of linear fitted lines and x-axis correspond to flat-band potential according to the following equation.

$$\frac{1}{C^2} = \left(\frac{2}{q\varepsilon_0 \varepsilon N_D}\right)\left(V - V_{FB} - \frac{kT}{q}\right) \tag{3.1}$$

C : capacitance at the space charge region

V : applied voltage

q : electronic charge

ε : dielectric constant of the semiconductor

ε_0 : permittivity of free space

N_D : donor concentration

T : absolute temperature

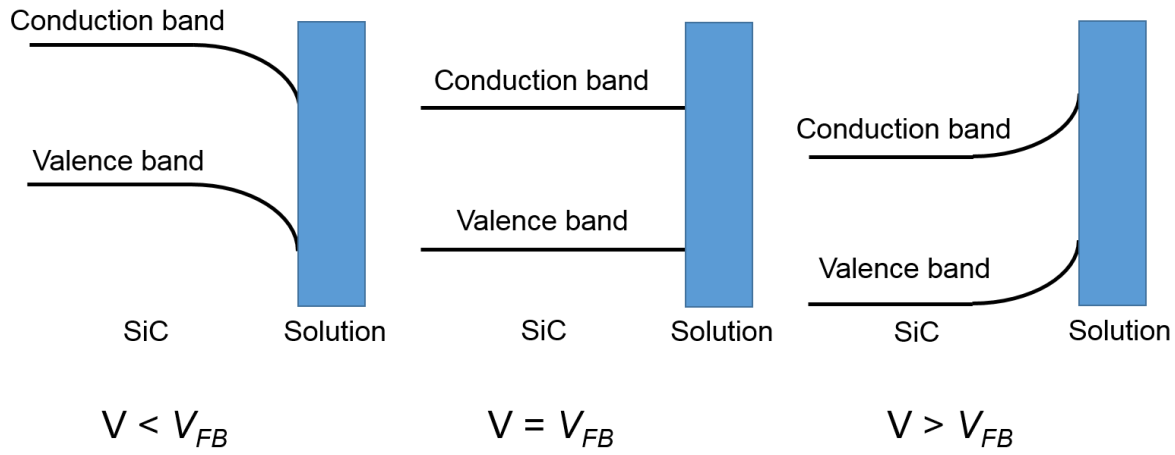

(a)

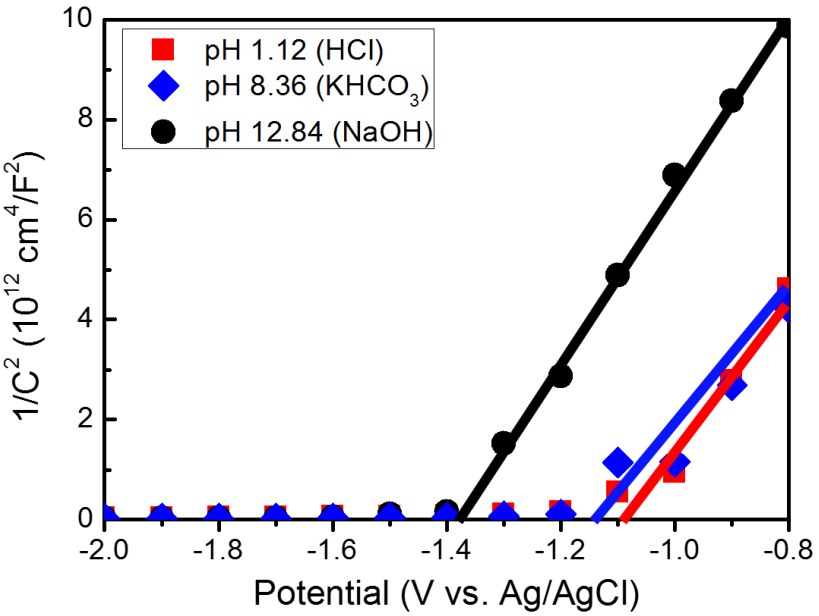

(b)

Figure 3.3. (a) Band energy scheme of the SiC photo-anode in junction with aqueous solution. The formation of bended band at the interface varied with an applied bias against flat-band potential (V_{FB}), (b) Mott-Schottky plots for n-type 3C-SiC obtained from an impedance measurement in different electrolytes. The linearly fitted line is drawn to calculate flat-band potential (V_{FB}) (intercepts at x-axis).

From the graph, we obtained the values of V_{FB}, -1.1 V, -1.15 V, and -1.4 V for pH 1.12, 8.36 and 12.84, respectively. Then, the band-edge potential can be obtained by measured V_{FB} with using the equation as following.

$$E_c = V_{FB} - \frac{kT}{q}\ln(\frac{N_c}{n}) \tag{3.2}$$

where E_c is the potential level of conduction band edge of the n-type semiconductor with the net carrier concentration, and N_c is the conduction band effective density of states explained in Eq. (A.6). The parameters of 3C-SiC semiconductor is found in the reference 54. As the result of this calculation, the band-edge of 3C-SiC is drawn as shown in Figure 3.4. Conduction band-edge is more negative than hydrogen-evolving potential (H_2/H^+) and valence band-edge is more positive than oxygen-evolving potential (H_2O/O_2). This result means 3C-SiC photo-anode is basically applicable for direct electro-photolysis to generate H_2 by only solar-light. In addition, the necessary potential level for reducing the CO_2 to HCOOH and CO is also expressed in Figure 3.4. The conduction band-edge is located at the more negative than the level to produce the HCOOH meaning that 3C-SiC has a sufficient energy to drive the electrons for the reaction of CO_2 reduction. These results are very significant that 3C-SiC has the merit of band-structure against both water-splitting and CO_2 reduction potential level with even proper band-gap for absorbing the visible range of solar-spectrum.

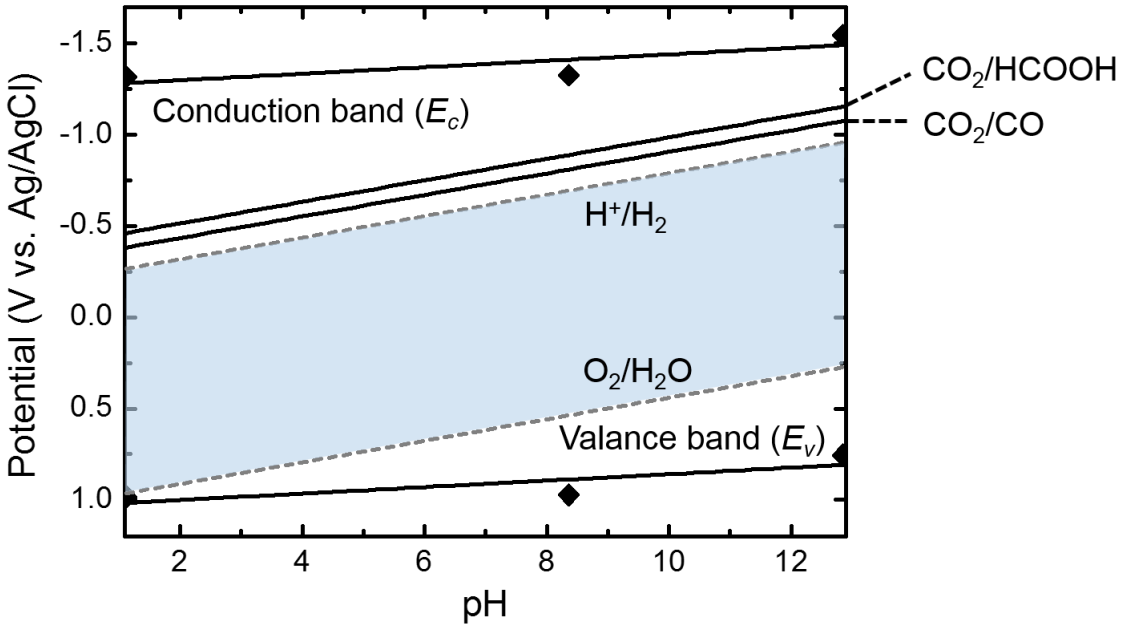

Figure 3.4. n-type 3C-SiC band-edge position as a function of pH. (0.01 M HCl (pH 1.12), 0.1 M $KHCO_3$ (pH 8.36) and 0.1 M NaOH (pH 12.84))

3.3.2 The photo-response characteristic of 3C-SiC photo-anode

The photo-response of 3C-SiC photo-anode is confirmed by CV method with and without light illumination. Figure 3.5 shows the result of the measurement. When the light is illuminated on the surface, it shows the photocurrent of 0.209 mA/cm^2 at 1 V (vs. Ag/AgCl) and 0.006 mA/cm^2 at 0 V, while no photocurrent is observed at the positive bias range when the light is turned off. Additionally, the photocurrent with an ultraviolet (UV) filter which cut the wavelength below 400 nm is compared. The photocurrent dropped to 70 % of the case without UV filter. It means that 3C-SiC can normally show the photo-response at the oxidation reaction side and generate the carriers with only visible region of the light.

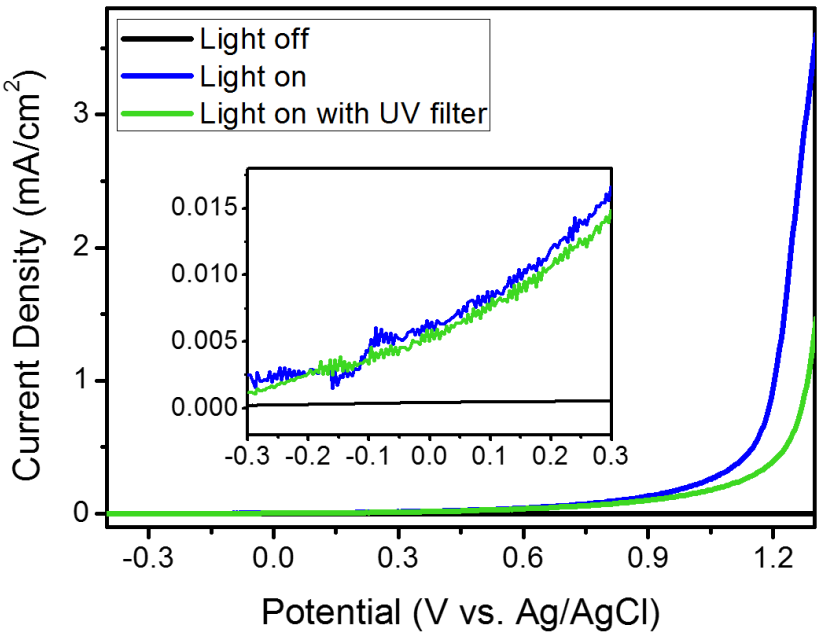

Figure 3.5. The confirmation of 3C-SiC photo-response in comparison with and without light illumination. The green line indicates the photocurrent with an UV cut filter. The inset is the magnified graph in the range from -0.3 V to 0.3 V. The applied power density of lamp is 994 mW/cm^2. (The electrolyte of HCl, pH 1.2)

3.3.3 The evaluation of ideal solar-conversion efficiency with 3C-SiC photo-electrode

Based on the applicable property of 3C-SiC as photo-electrode, the potential for highest performance with simple modeling of PEC cell. Figure 3.6 shows the band diagram of PEC cell with expression of some processes at interface. First of all, free-energy losses generally determined by entropy, carrier mobility, recombination, and light trap efficiency occurs inside device. Due to this loss, an available photovoltage (open circuit voltage) is finally less than actual band-gap value. Also, another losses can be existed during the process of charge transfer from the bulk of material to electrolyte. This is directly related to the

overpotential for oxidation and reduction reaction. Although there can be shunt losses originated from defect or grain boundary of crystal lattice, we will focus on the free-energy and kinetic losses issue.[22]

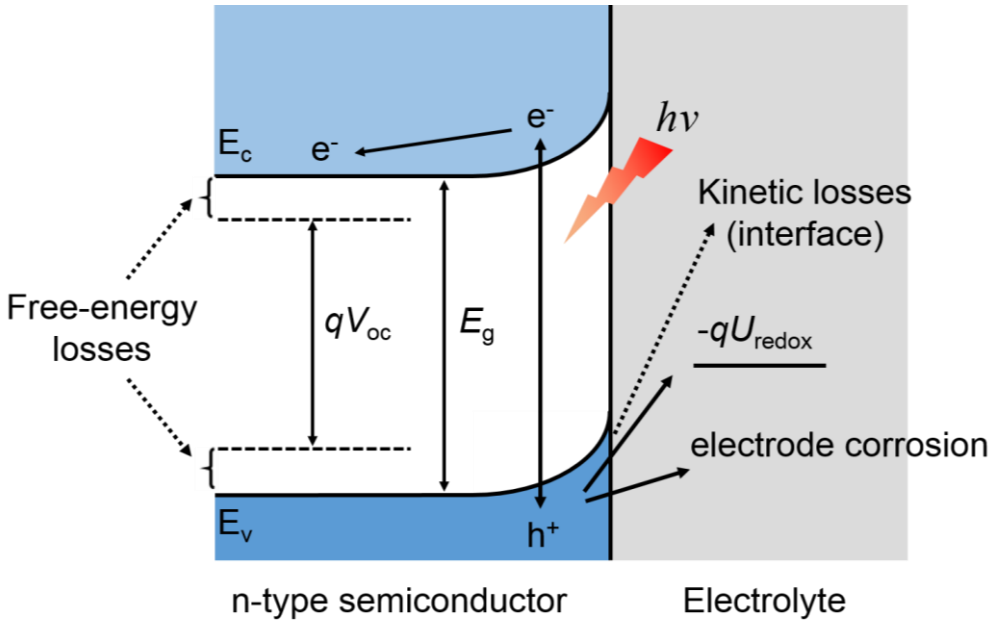

Figure 3.6. Energy band diagram of semiconductor/electrolyte junction for PEC water-splitting showing representative losses.

Open circuit voltage consideration

Under ideal condition, 13.1 % (10.74 mA/cm^2) is calculated as achievable maximum STH efficiency by 3C-SiC with 2.3 eV. For more practical expectations for 3C-SiC, we studied the effect of open circuit losses by using PN junction diode modeling which is considered as same condition with semiconductor/electrolyte junction without kinetic losses. Figure 3.7 shows the J-V characteristic of PN junction diode. When light is illuminated, saturation current (J_{sc}) increases to J_{ph}. At that time, a voltage value to flow no current is open

circuit voltage. The diode current equation and open circuit voltage (V_{oc}) is expressed as followings.[55]

In dark state,

$$J(V_a) = J_0[\exp(\frac{qV_a}{kT}) - 1] \tag{3.3}$$

where J_0 is saturation current density of PN junction, and V_a is an applied bias.

Under light illumination,

$$J(V_a) = J_0[\exp(\frac{qV_a}{kT}) - 1] - J_{ph} \tag{3.4}$$

Where J_{ph} is the photo-generated current density.

$$V_{oc} = V_a(J = 0) \tag{3.5}$$

By using the Eqs. (3.5) and (3.6), the relationship of V_{oc} and J_{ph} is obtained.

$$V_{oc} = V_a(I = 0) = \frac{kT}{q} \cdot \ln(\frac{J_{ph}}{J_s} + 1) \approx \frac{kT}{q} \cdot \ln\frac{J_{ph}}{J_s} \tag{3.6}$$

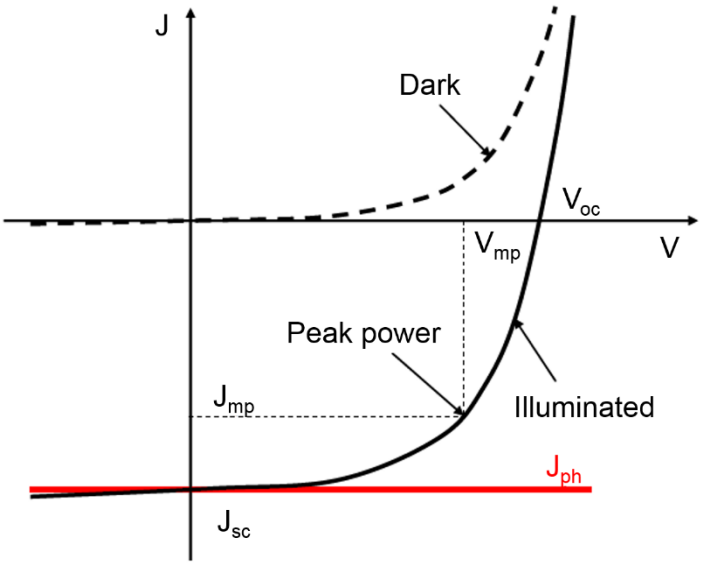

Figure 3.7. J-V characteristics of PN junction diode in comparison of dark and light illumination state. (Adapted from the reference 55)

Figure 3.8 is the result of a calculated relationship between free-energy losses value and maximum efficiency especially about band-gap of 2.3 eV for 3C-SiC. For saturation-current density (J_0) is 3×10^{-31} mA/cm^2.[56] When the open circuit losses is 0.5 V, the photocurrent of 5.87 mA/cm^2 with 7.21 % in STH efficiency is achievable. However, the maximum photocurrent is greatly decreased to 0.13 mA/cm^2 and STH efficiency is 48 times lower, 0.15 % as compared to open circuit loss of 0.5 V. The open circuit voltage is a measure of the amount of recombination in device.[57, 58] The recombination factor is largely affected by the type of band to band transition (direct or indirect). Especially, free-energy losses of indirect band-gap semiconductors has been reported to be about 0.6 V indicating it needs to reduce the free-energy loss for 3C-SiC.[57] Therefore, it needs to reduce the free-energy loss of 3C-SiC.

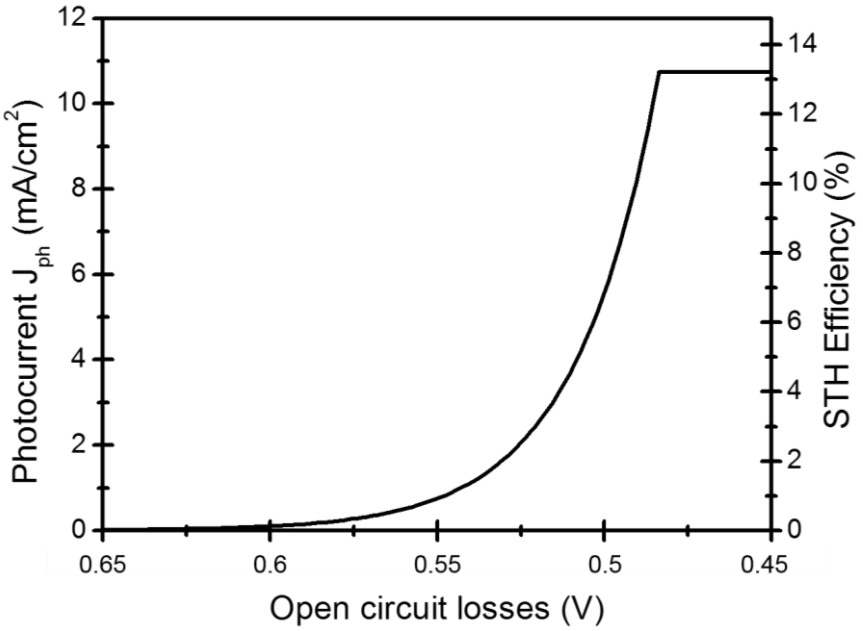

Figure 3.8. Maximum photocurrent and STH efficiency as function of open circuit losses for the band-gap of 2.3 eV.

Kinetic losses issue

Kinetic losses occurs at the interface between semiconductor and electrolyte during charge transfer process. For gaining a relevant current flow for practical STH efficiency, overpotential is certainly required as shown in Tafel equation given by:

$$i = i_0 \exp(\alpha \frac{zq\eta}{kT}) \tag{3.7}$$

i_0 : exchange current density

α : charge transfer coefficient

z : valance number

η : overpotential

The overpotential for oxygen evolving reaction (OER) and hydrogen evolving reaction (HER) is different with regards to the catalyst type as shown in Figure 3.9. The overpotential corresponding to operating current for various catalyst material is determined by Butler-Volmer equation. For sufficient current flow, overpotential is exponentially increased. In this research, inorganic semiconductor which has not high catalytic ability is used as photo-electrode.[59] Therefore, it is expected to be necessary to introduce some co-catalytic material for promoting the redox reaction at the interface.

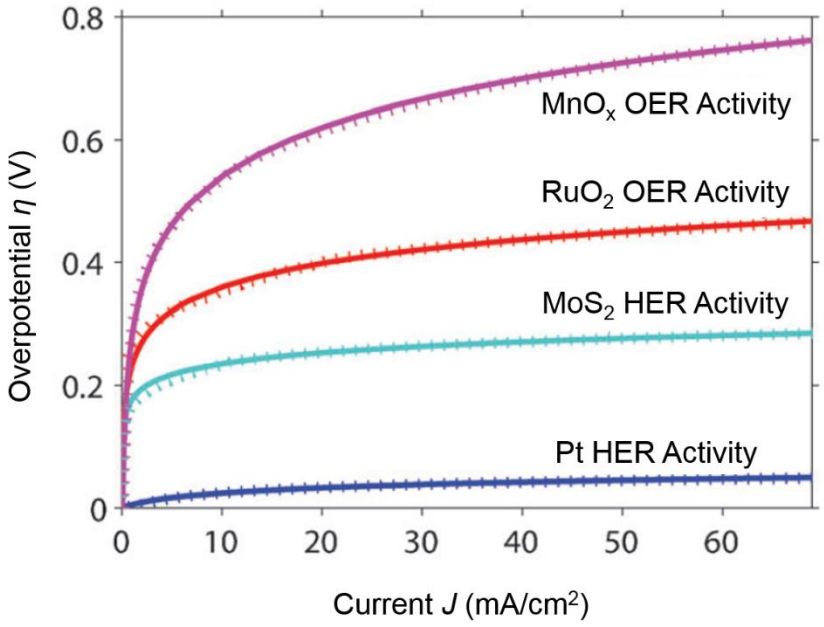

Figure 3.9. Overpotential and current relationship for various catalytic materials. (Adapted from the reference 22)

The operation of electrochemical cell combined with PV solar cell

For comparison of the two system for solar-to-chemical conversion system in viewpoint of achievable efficiency as discussed in Section 1.4, the electrochemical system

combined with PV solar cell is considered here. The merit of this method is that developed PV solar cell which has high solar-to-electricity conversion efficiency over 20 %. However, it needs to consider some conditions for water-splitting in this method. First, photovoltage has to be obtained over 1.23 V to drive water-splitting reaction. Figure 3.10 shows photocurrent curve with applied voltage for typical polycrystalline Si (c-Si) solar cell and electrochemical cell with general metal electrodes, separately. I-V curve for solar cell is obtained from the ideal diode equation with using the presented specification (open circuit voltage (V_{oc}) and short circuit current (I_{sc})) of c-Si in reference 13. The operation of electrochemical cell is expressed by Tafel equation eq. (3.7) with i_0 of 10^{-6} A and η of 1.3 V. Figure 3.10(a) is the I-V graph in the case of single structure of c-Si solar cell. In order to operate the combined cell, there must exist intersection point of each I-V graph. However, it cannot be fundamentally operated due to the insufficient V_{oc} for c-Si solar cell regardless of solar to electricity conversion efficiency of solar cell. The connection of c-Si solar cell in series is shown in Figure 3.10(b) to generate large V_{oc}. Accordingly, two I-V curves intersects at (1.60 V, 183.9 mA). In this operation point, STH conversion efficiency is calculated to about 7 %. As different way, concentrated photovoltaic (CPV) solar cell can be used for water-splitting as shown in Figure 3.11. Almost whole solar spectrum can be absorbed with tandem structure and solar to conversion electricity efficiency is improved with combination of light concentrating structure.[111] Due to the sufficient V_{oc}, this combined cell is operated at (1.55 V, 26.8 mA) without series connection. The STH efficiency at this point is 14 %. In this results, it is confirmed that relatively high STH efficiency can be achieved with PV solar cell improved to generate large V_{oc}. However, the problem is that STH efficiency for both series connection of c-Si and CPV is lower than maximum solar conversion to electricity efficiency of solar cell itself. It is known that solar cell provides a maximum

power output at the knee point of I-V curve.[13] Therefore, it is necessary to adjust operation point with some methods such as series connection or DC-to-DC converter to minimize this critical loss which is the largest obstacles of efficient solar storage. These additional method should cause further loss in solar conversion process with increasing cost. Because of this issue, direct solar-to-chemical conversion system with 3C-SiC is should be promising with simple structure.

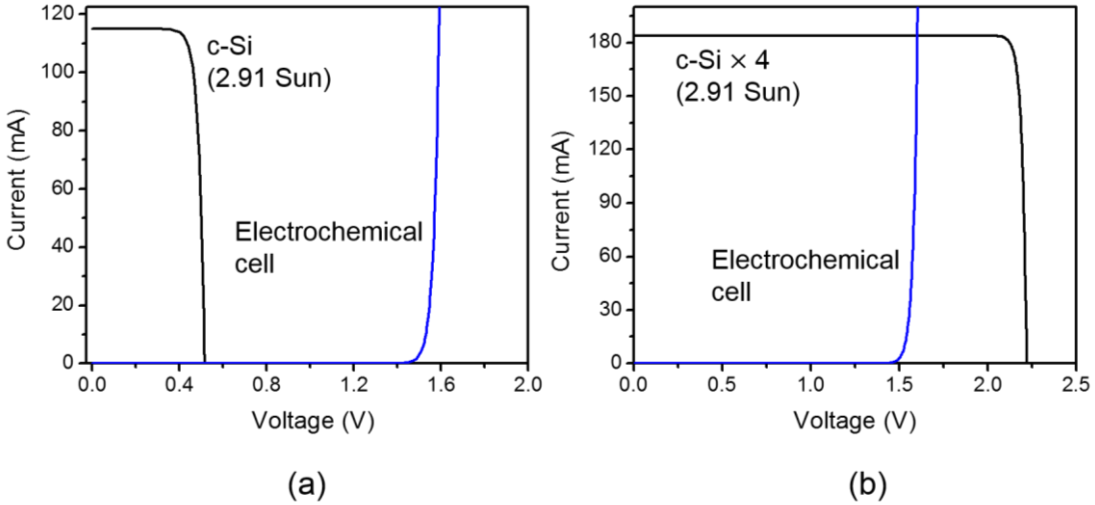

Figure 3.10. I-V curve for c-Si solar cell and electrochemical cell, separately under 2.91 Sun (291 mW/cm^2). (a) single structure of c-Si solar cell (Area = 6.1 cm2, *Isc* = 115.6 mA, *Voc* = 0.513 V, Maximum solar to electricity conversion efficiency = 3 %) and (b) 4 series connection of c-Si solar cell. (Area : 20.3 cm2 × 4, *Isc* = 183.9 mA, *Voc* = 2.21 V, Maximum efficiency = 9.6 %)

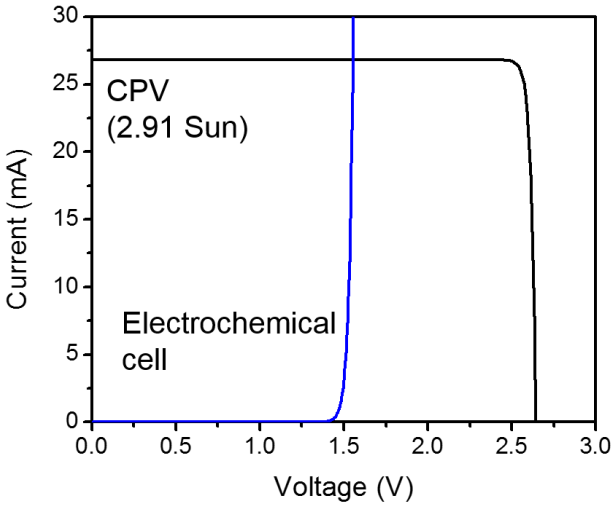

Figure 3.11. I-V curve for CPV solar cell and electrochemical cell under 2.91 Sun (291 mW/cm^2) (Area : 1 cm^2, I_{sc} = 26.8 mA, V_{oc} = 2.64 V, Maximum efficiency = 23 %)

3.4 The current limitation against high performance

3.4.1 High overpotential for the reaction

Some kinds of losses causing the decrease of the solar-conversion efficiency were discussed in Section 3.3.3. Although the improvement of open circuit voltage is important, the overpotential is necessarily investigated to aim high efficient PEC performance. In common, many types of inorganic semiconductors have been studied in combining with catalyst materials.[60, 61] Therefore, it is important to consider the overpotential for reaction. Figure 3.12 shows the comparison of photocurrent characteristic between an ideal and a typical photo-electrode.[62] Ideally, photocurrent is started to increase at V_{FB} while V_{onset} is shown at the more positive point with the typical photo-electrode. Here, the overpotential for oxidation reaction (η_{ox}) is simply estimated by comparing the onset potential (V_{onset}) which is the point to increase the photocurrent and V_{FB} of semiconductor/liquid junction as following.

$$\eta_{ox} = V_{FB} - V_{onset} \tag{3.8}$$

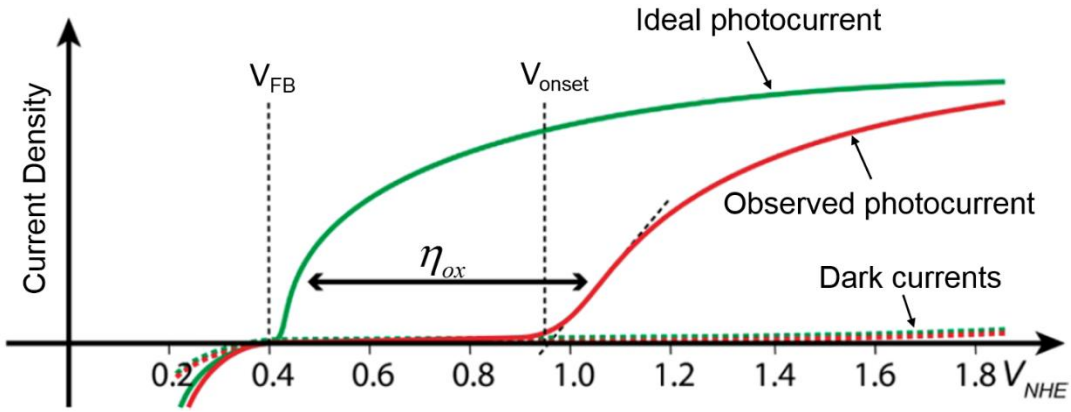

Figure 3.12. The comparison between the ideal photocurrent and the observed photocurrent curve. η_{ox} indicates the overpotential for oxidation reaction. (Adapted from the reference 62)

Under this scheme, we could investigate the estimated overpotential of 3C-SiC photo-anode from the Figure 3.13. In Figure 3.13(a) and (b), the photocurrent characteristics of highly-, lightly-doped 3C-SiC, and n-type 4H-SiC are exhibited. For 3C-SiC, the photocurrent density (J_{ph}) for the lightly-doped sample (1 mA/cm^2 at 0.5 V) is higher than that of highly-doped one (0.4 mA/cm^2). 4H-SiC shows the lower photocurrent of 0.24 mA/cm^2 at 0.5 V than 3C-SiC mainly because of light absorption limitation by larger band-gap, 3.3 eV. In comparison of V_{onset}, which is the intercept with potential axis of the line for linear part of the curve, the lightly-doped 3C-SiC has - 0.1 V lower than 0.1 V for the highly-doped. These difference between lightly- and highly-doped one should originate mostly from extended carrier life-time inside bulk the width of depletion layer formed at the interface between photo-anode and electrolyte. Especially, this width (W_{dep}) can be calculated by V_{FB} from the Mott-

Schottky plot in Figure 3.13(b) with Eq. (1.2). In Eq. (1.2), V_B can be calculated by following equation.

$$V_B = V_{redox} - V_{FB} \tag{3.9}$$

where V_{redox} is the potential of redox couples. All numerical values from this result is summarized in Table 3.1. W_{dep} for lightly-doped 3C-SiC shows almost 10 times wider, and the life-time for the light-generated minority carrier, holes is roughly 100 times longer under general relationship of carrier life-time and doping density resulting in higher photocurrent.[63] On the other hand, V_{onset} of 4H-SiC is -1.33 V, greatly lower than 3C-SiC whereas it has almost similar width of depletion layer with lightly doped 3C-SiC. The difference between 4H-SiC and 3C-SiC is investigated through carrier life-time measurement by the microwave-photconductivity decay (μ-PCD) method. As the result of measurement, the change in concentration of excess carriers excited by laser pulse with the wavelength of 349 nm is observed by microwave reflectivity as shown in Figure 3.14. Carrier life-time is considered as same with microwave reflectivity time. Here, we firstly note that laser excitation for 4H-SiC sample can be affected from bulk part not only from epitaxial layer which is mainly utilized for photo-electrode application although 4H-SiC was measured as reference sample. Therefore, the life-time for 4H-SiC (~ 0.3 μs) should be shorter than lightly doped 3C-SiC (~ 1 μs). In this result, however, the most important point is the time from the point of 1/e to $1/e^2$ that is slower component of the photoconductivity decay curve. This time is 0.088 and 0.023 μs for 3C-SiC and 4H-SiC. It was reported that this slow component is caused by a defect which provides trap level.[64, 65] Under the assumption that the capture cross section of majority carrier is even smaller than minority carriers, the defects trap excess minority carriers and do not easily release to recombine with majority carriers. Therefore, a longer slow

component indicates the larger density of defects. Based on this reports, 3C-SiC is expected to have a much higher density of defects because 3C-SiC was grown on Si substrate. In the PEC performance, these kinds of defects would be considered as surface state which disturbs carrier transfer and chemical reaction at the interface as shown in Figure 3.15. The effect of surface state for 3C-SiC and 4H-SiC is evaluated with transient photocurrent characteristic when light illumination starts on the sample. In Figure 3.16(a), the spikes of photocurrent level at 60 s for 3C-SiC are obviously observed for 0 and 0.3 V (vs. Ag/AgCl). This phenomenon occurs because some fraction of light-generated holes traveled to the surface of the photo-electrode accumulate because of high kinetics of oxidation reaction or can be trapped at surface states or inside bulk.[66] For 3C-SiC, the ratio of spike part in the whole curve area for 0.3 V is 1.7 %, whereas it is 9.5 % for 0 V. It indicates that larger applied bias promotes carrier transfer at the interface. In Figure 3.16(b), the photocurrent curve of 4H-SiC almost does not show the spike. At 0 V, very small spike is shown having a ratio of 0.7 % in whole area. However, no spike is shown at 0.3 V. It indicates that many surface states should exist on 3C-SiC more than 4H-SiC. Finally, it is demonstrated that surface state affects the overpotential to drive water-splitting. Whereas 4H-SiC has η_{ox} of 0.41 V, it is calculated to 1.45 and 1.2 V for highly- and lightly-doped sample by V_{onset} and V_{FB}. Fairly large overpotential is currently required for 3C-SiC due to the existence of lots of surface state. Therefore, it needs some strategies for not only improvement of catalytic ability but also suppress of surface state effect in order to enhance the whole electrochemical reaction with 3C-SiC photo-electrode.

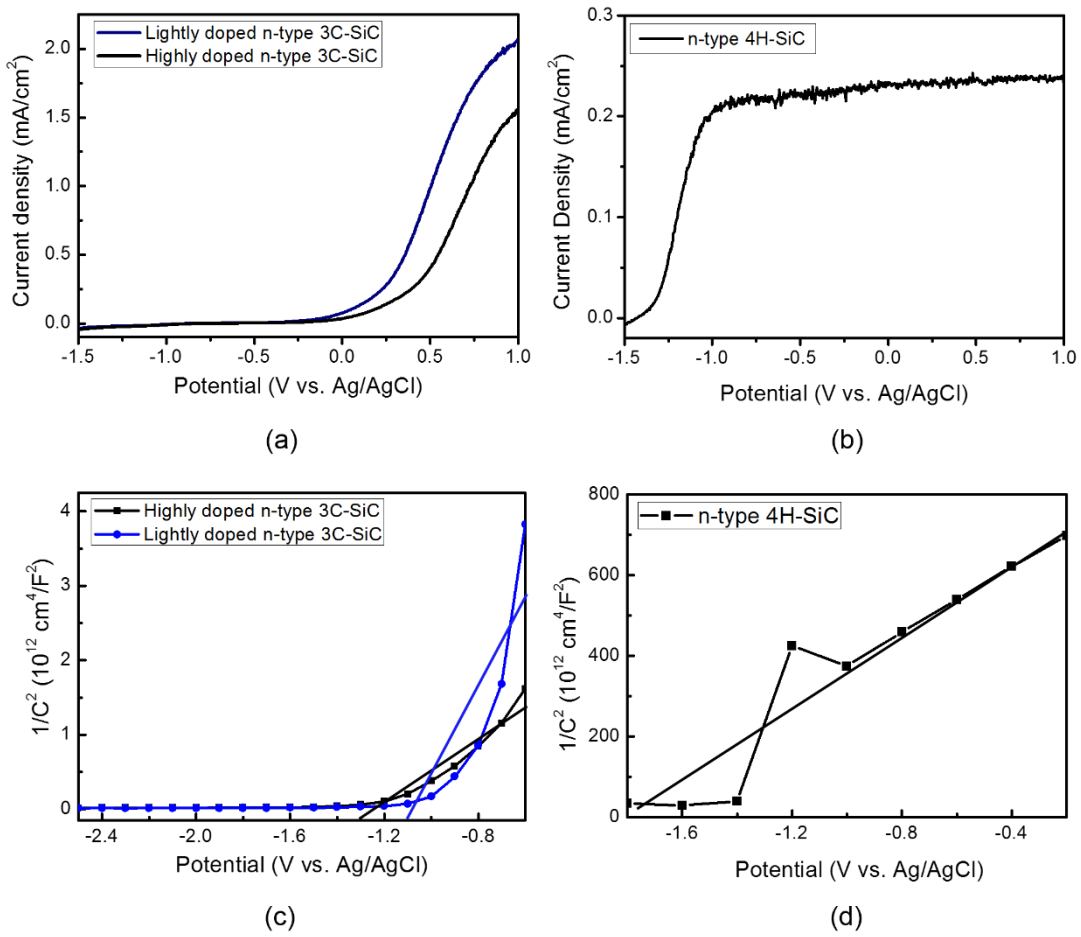

Figure 3.13. Photo-current density vs. potential for (a) the highly and lightly doped 3C-SiC and (b) 4H-SiC (Light illumination of 100 mW/cm^2) and Mott-Schottky plot for (a) highly and lightly nitrogen-doped 3C-SiC in NaOH aqueous solution (pH 13).

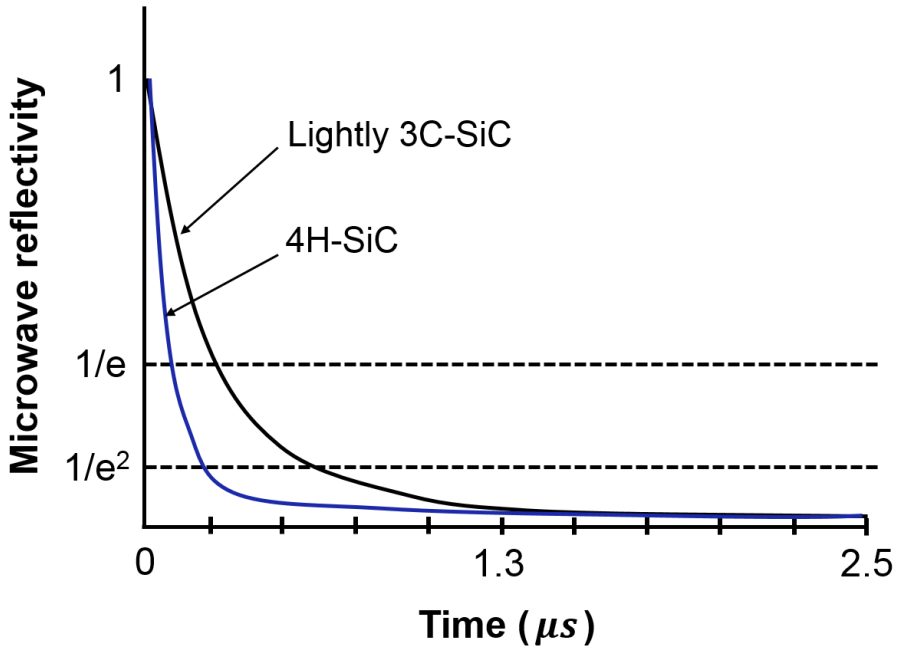

Figure 3.14. Photoconductivity decay curves for lightly doped 3C-SiC and n-type 4H-SiC samples. The life-time of excessive carriers is defined as the time at which microwave reflectivity is decayed from 1 to 1/e. (Laser wavelength is 349 nm.)

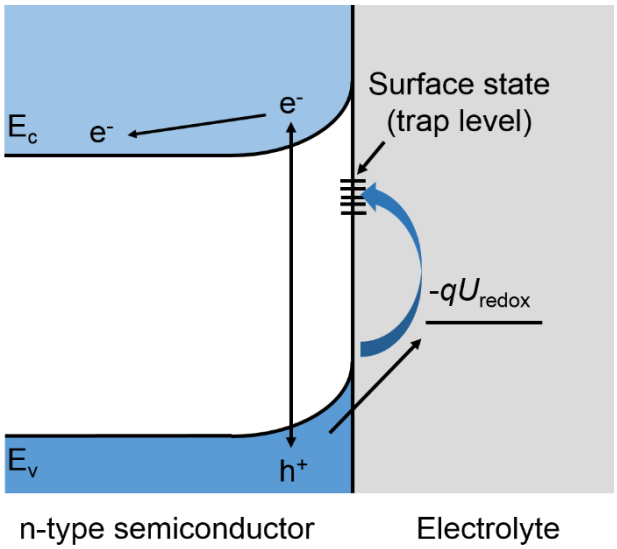

Figure 3.15. Schematic illustration of surface state at the interface between semiconductor and electrolyte junction. Reached holes to the surface of semiconductor have a probability to be trapped at surface states without chemical reaction.

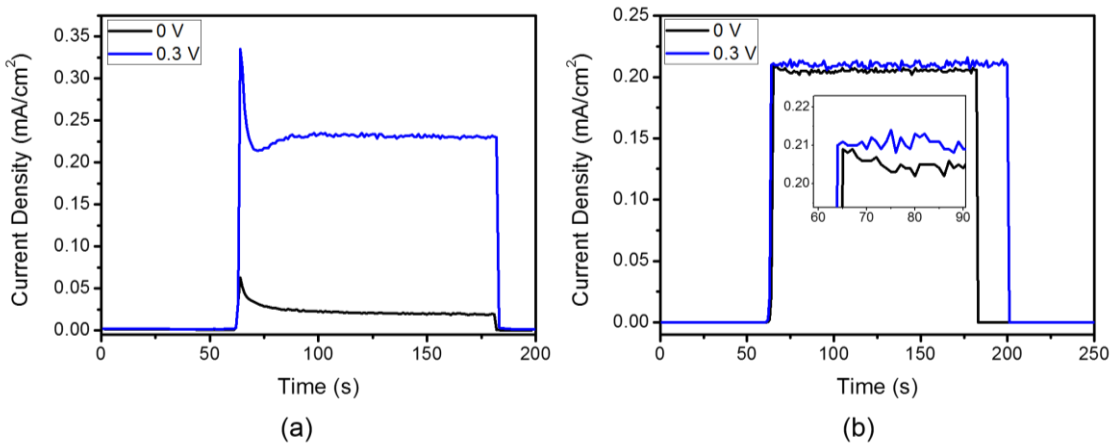

Figure 3.16. Observation of photocurrent flow at fixed bias of 0 and 0.3 V (vs. Ag/AgCl) for (a) lightly doped 3C-SiC and (b) 4H-SiC. Light is turned on at 60 s and turned off at around 180 – 200 s. (Electrolyte : NaOH (pH 13) and Light power : 100 mW/cm^2)

Table 3.1. Several properties of SiC photo-electrodes obtained from Figure 3.13 and Figure 3.14.

Sample type	V_{onset}	J_{ph} **(at 0.5 V)**	W_{dep}	**Carrier life-time**	V_{FB}	η_{ox}
Highly 3C-SiC	0.1 V	0.4 mA/cm^2	0.3 μm	N/A	-1.35 V	1.45 V
Lightly 3C-SiC	-0.1 V	1 mA/cm^2	3.7 μm	1 μs	-1.10 V	1.20 V
n-type 4H-SiC	-1.33 V	0.24 mA/cm^2	3 μm	0.3 μs	-1.74 V	0.41 V

3.4.2 Surface corrosion of the SiC photo-electrode

For commercialization of the photo-electrode, the long stability is strongly necessary during the electrochemical reaction. In order to examine the surface corrosion, surface components of 3C-SiC (lightly doped) are analyzed by Time-of-Flight Secondary Ion Mass Spectrometry (TOF-SIMS) after the PEC reaction for 3000s at an applied bias of 2 V (vs. Ag/AgCl) in the electrolyte of HCl. Figure 3.17 shows the analysis result of 3C-SiC in comparison between before and after PEC reaction. The most different thing is the profile of SiO_2. It is known that SiC is dissolved by oxidation reaction and SiO_2 formation occurs from the following reaction.[67]

$$2SiC + 6H_2O + 12h^+ = SiO_2 + CO_2 + SiO + CO + 12H^+ \quad (3.10)$$

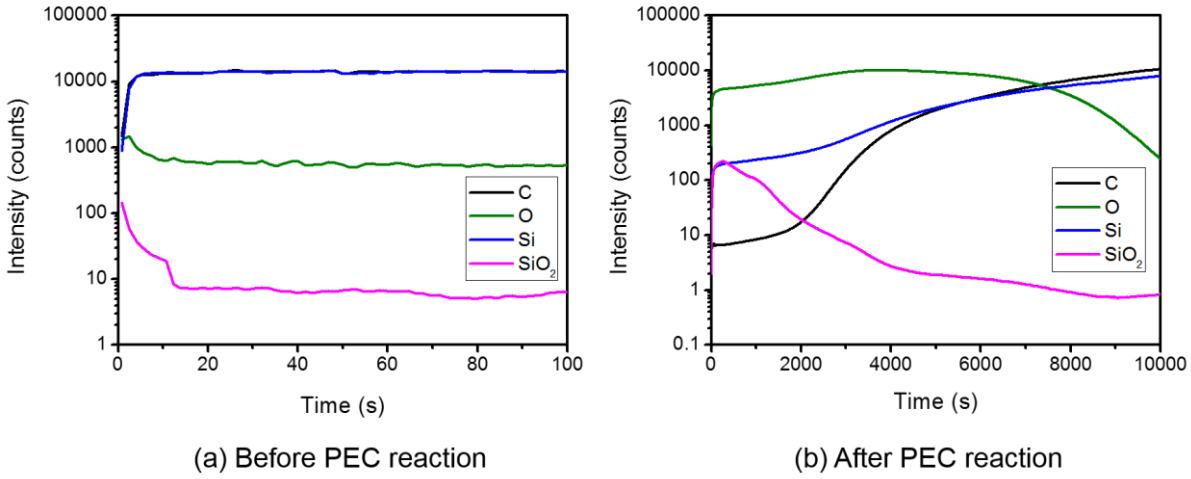

Figure 3.17. The SIMS profile of 3C-SiC surface.

Figure 3.18 shows the optical microscope image of the 3C-SiC surface before and after the PEC reaction. After the reaction, surface is severely corroded with formation of SiO_2. The line on the surface after the reaction might be originated from preferential oxidation at the stacking faults of the 3C-SiC growth process.[68] As shown in Figure 3.19, stacking faults evolved during growth process should exist. Because the surface oxidation is preferentially occurred at this defects. Therefore, it is expected that electrochemical etching might continue from point 1 to point 2 and in other ways along stacking faults. That is, surface oxidation is occurred at surface itself and inside substrate along the defects. As a result, it causes the degradation of the photo-anode performance with water oxidation reaction.

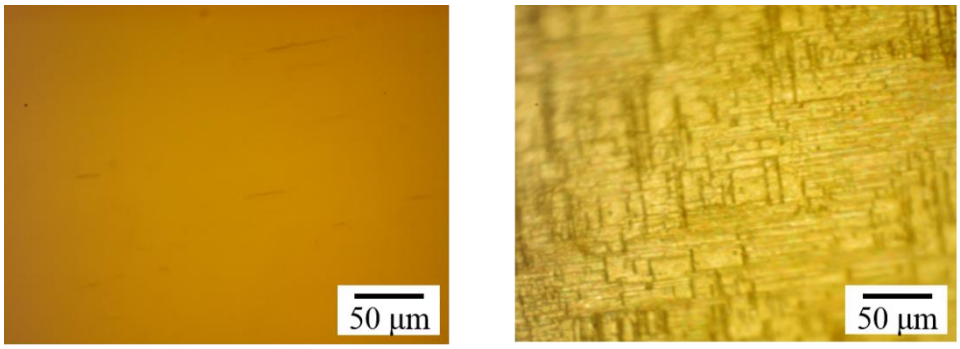

Figure 3.18. The image of the 3C-SiC surface by optical microscope.

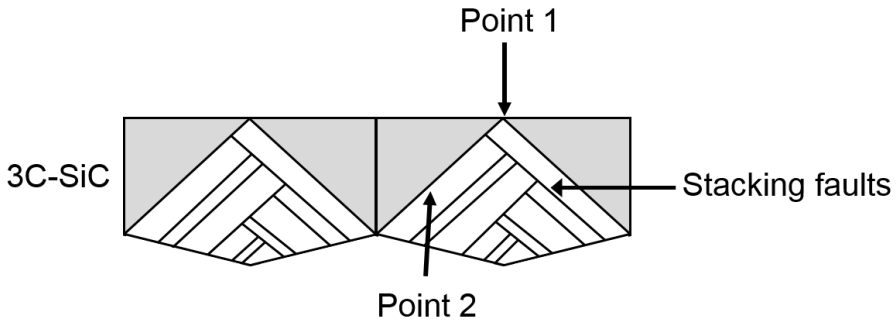

Figure 3.19. Cross-sectional view of 3C-SiC photo-electrode with shown stacking faults.

3.5 Conclusion

In this chapter, we demonstrated both prospective and current limitation of 3C-SiC as photo-electrode. In the Section 3.3, we confirmed that 3C-SiC has the band-structure for both water-splitting and CO_2 reduction. Also, important issues affecting PEC performance of 3C-SiC such as free-energy loss and kinetic loss are reviewed. In the Section 3.4, actual limitation lowering the PEC performance of 3C-SiC is investigated. First, the overpotential for oxidation reaction affect the degradation for high solar-conversion efficiency. Specifically, the main reason of high overpotential for 3C-SiC is revealed large density of surface state which is kinds of semiconductor defects by measurement of μ-PCD in comparison of 4H-SiC. Thus, carrier transfer from the 3C-SiC to the solution side should be disturbed by the surface state. Second, surface oxidation reaction of 3C-SiC itself occurs during PEC reaction. It results in short stability due to the formation of SiO_2 on the surface with severe corrosion. Therefore, it strongly needs to overcome the overpotential and corrosion at the surface. In the next Chapter 4 and Chapter 5, the methods for solution of these problem will be discussed.

Chapter 4
The improvement of photoelectrochemical property of 3C-SiC with Pt particles

Chapter 4. The improvement of photoelectrochemical property of 3C-SiC with Pt particles

4.1 Introduction

We demonstrated that the problem of high overpotential for oxidation reaction with 3C-SiC photo-electrode is one of the large obstacles towards realization of artificial photosynthesis in Section 3.4.1. The effect of surface state of SiC photo-electrode needs to be minimized for removing the losses. In order to solve this problem, another materials with high catalytic ability is necessary on the surface of 3C-SiC against surface state and low catalytic ability. Generally, transition metals are known to have a high catalytic functionality. Among those materials, Pt is not only very stable metal against corrosion but also has high work function of 5.4 eV, which is sufficient to form band-bending at the interface with 3C-SiC (work function of 4 eV).[69] In this chapter, we fabricate and characterize the effect of Pt particles on the surface of 3C-SiC with aiming the improvement of performance.

4.2 The effect of Pt for the 3C-SiC photo-electrode

4.2.1 Potential induction at the interface

Figure 4.1 shows the mechanism of charge separation of Pt/3C-SiC photo-electrode and redox reaction at the surface of the electrode. The products of water oxidation reaction at the surface of the photo-electrode should be O_2. At the opposite side (counter electrode), H_2 gas is generated by reduction reaction.[43] Pt particles on the surface of 3C-SiC are expected to enhance the PEC reaction by formation of band-bending at the interface between 3C-SiC photo-electrode and Pt particles. As a result, facile hole-transfer from 3C-SiC to the electrolyte via Pt NPs with reducing recombination is achieved at the valence band side for the oxidation reaction. The decreased recombination should lead to the enhancement of PEC reaction.[70]

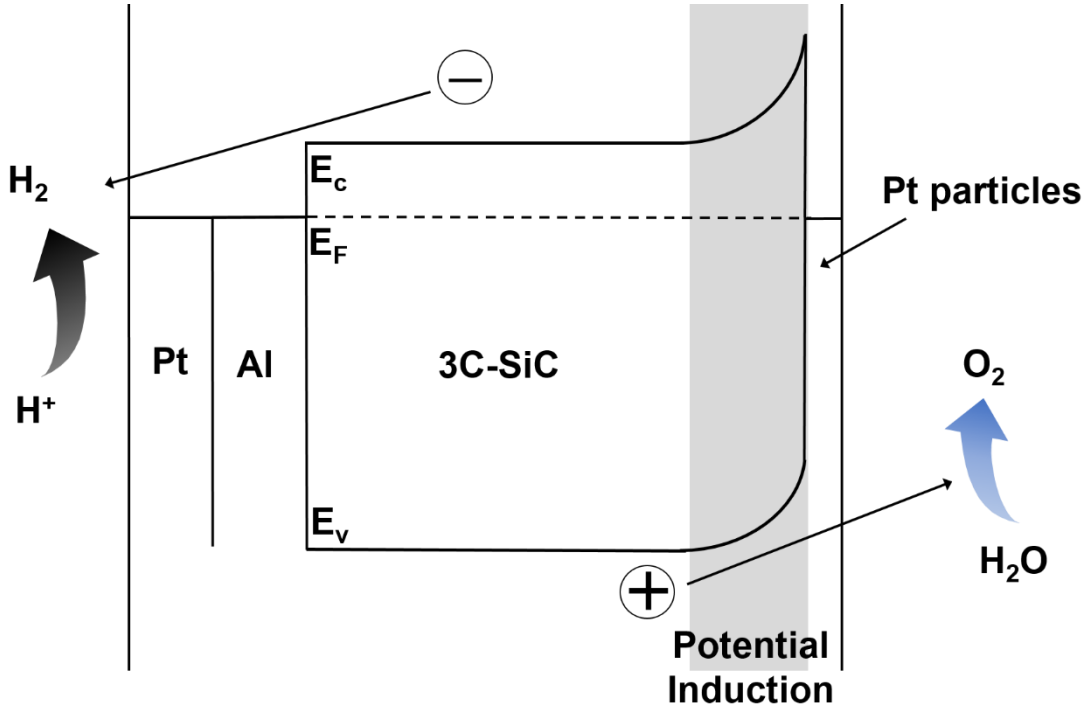

Figure 4.1. Schematic illustration of excited charge carrier separation in the Pt particle/3C-SiC photo-electrode.

4.2.2 Suppression of the corrosion

In addition to the induced potential by Pt particles, it is also expected to keep durability of 3C-SiC surface as shown in Figure 4.2. As indicated in Section 3.4.2, excited holes in the 3C-SiC occurs not only water oxidation but also oxidation of the 3C-SiC surface itself, causing the formation of SiO_2. In the case of 3C-SiC with Pt particles, however, the carriers are induced to be transferred through the Pt particles preferentially. Finally, the oxidation of 3C-SiC surface is suppressed. Thus, better stability of the 3C-SiC photo-electrode might be achieved with Pt particles.

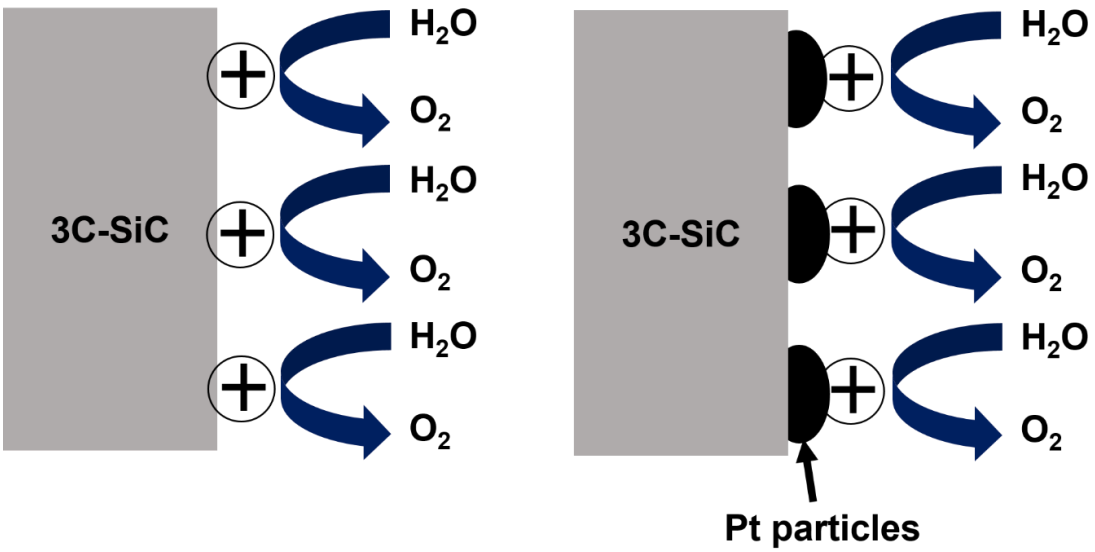

Figure 4.2. Schematic illustration of excited charge carrier separation in the Pt particle/3C-SiC photo-electrode.

4.3 The fabrication of Pt particles

Figure 4.3(a) shows the fabrication process of the Pt particles on 3C-SiC. First, a Pt layer ~2 nm in thickness was deposited by RF-sputtering on the surface of bare 3C-SiC (Lightly (1.0×10^{16} cm^{-3}) nitrogen-doped sample). The Pt-deposited 3C-SiC sample was annealed at 400 ℃ for 30 min under Ar at a pressure of 10 kPa to form particles. In detail, the annealing temperature increases to 400 ℃ at a rate of 100 ℃ /m and is kept for 30 min as shown in Figure 4.3(b). The particle formation was confirmed by AFM as shown in Figure 4.4. Pt particles with size of ~3 nm in height were formed on the surface.

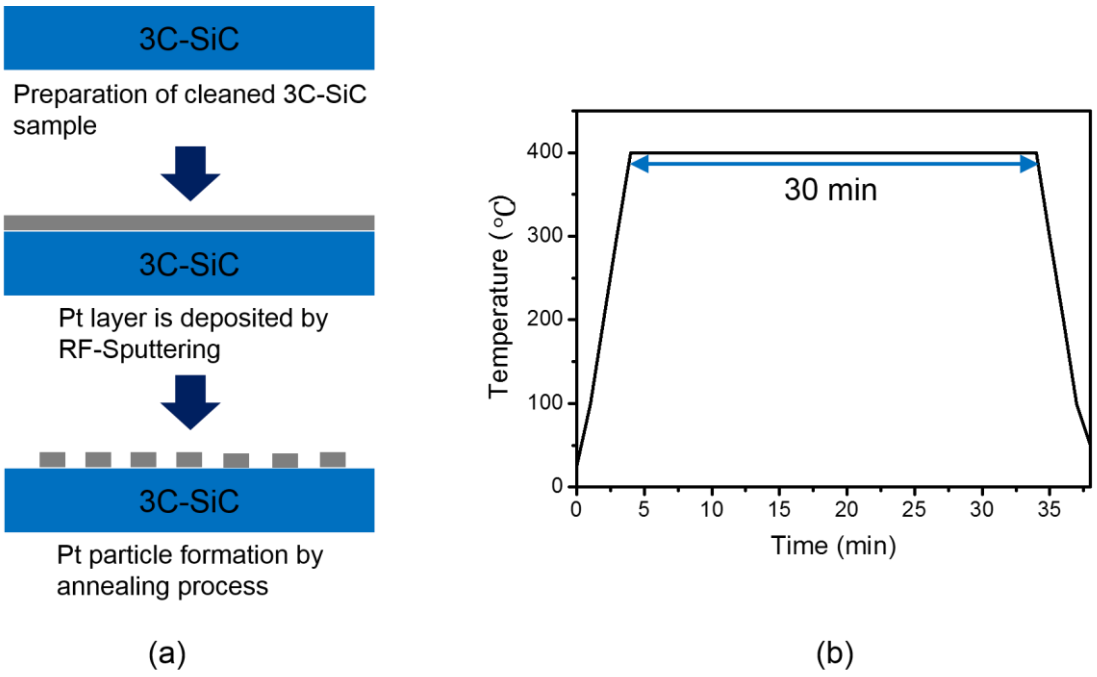

Figure 4.3. (a) Fabrication process of Pt particles, (b) Illustration of the temperature control.

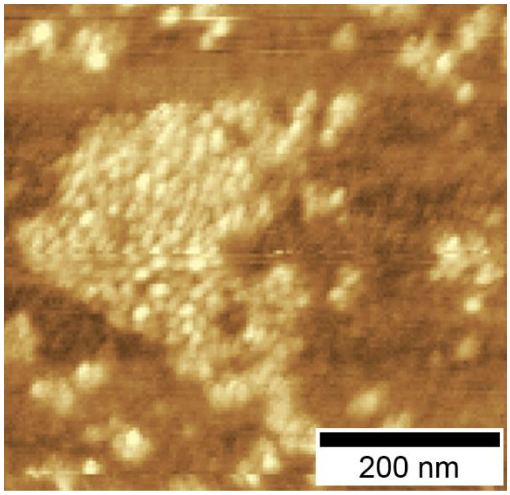

Figure 4.4. The AFM image for the surface of the sample with Pt particles.

4.4 The evaluation of PEC property with Pt particles

4.4.1 The result of photocurrent characteristic

Figure 4.5 shows the photocurrent characteristic of bare 3C-SiC and 3C-SiC with Pt particles (Pt particles/3C-SiC). While bare 3C-SiC shows the photocurrent density of 0.02 mA/cm^2 at 0.83 V (vs. Ag/AgCl), it dramatically increases to 0.7 mA/cm^2 in the case of Pt particles/3C-SiC. The onset potential (V_{onset}) is also shifted to 0.7 V, lower than ~1.1 V without the Pt particles. The STH conversion efficiency (η) at an applied bias is also estimated by using the following equation.[71]

$$\eta = \frac{i(1.23 - E)}{P_{in} A} \times 100 \qquad (4.1)$$

where i (A) is a photocurrent obtained after stabilizing photocurrent with time at an applied bias, E (V) converted to reversible hydrogen electrode (RHE) scale via Nernst equation from measured potential vs. Ag/AgCl for pH independence. P_{in} (W/cm^2) is the power density of incident light source, and A (cm^2) is the working electrode surface area. The calculated efficiency is described in Table 4.1 with other photocurrent properties. As a result, the solar-conversion efficiency at an applied bias of 1.1 V (vs. RHE) becomes about 33 times greater than bare 3C-SiC.

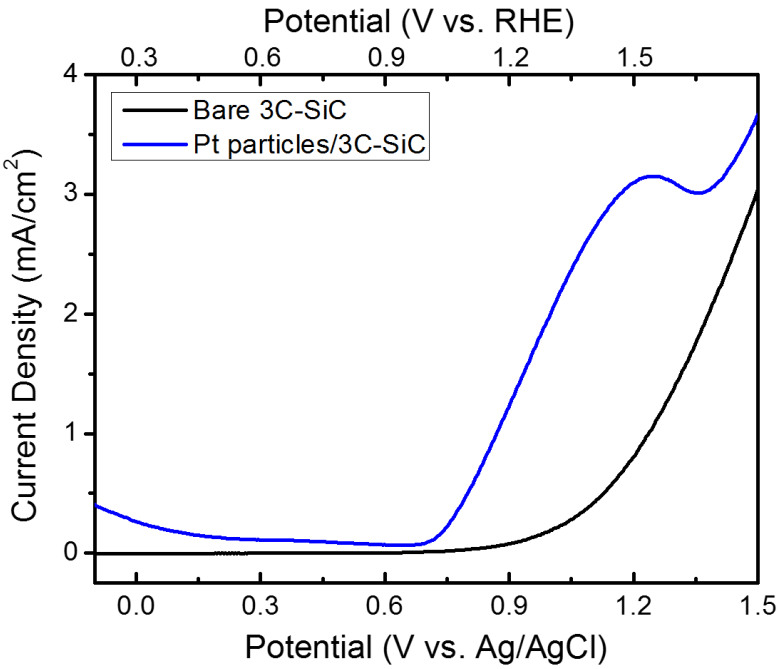

Figure 4.5. Photocurrent density vs. potential for comparing bare 3C-SiC and Pt particles/3C-SiC. (355 mW/cm^2 of the light power, HCl (pH 1.12))

Table 4.1. The comparison of photocurrent properties for 3C-SiC with and without Pt particles.

Sample	**Onset potential**	**Current (at 0.83 V)**	**η (at 0.83 V)**
Bare 3C-SiC	1.1 V	0.02 mA/cm^2	0.003 %
Pt particles/3C-SiC	0.7 V	0.7 mA/cm^2	0.1 %

4.4.2 Incident photon-to-current efficiency (IPCE)

We investigated UV-Vis absorption and IPCE to clarify the reason of improved efficiency by Pt particles as shown in Figure 4.6. UV-Vis absorption property is compared between bare 3C-SiC and Pt particles/3C-SiC in Figure 4.6(a). In Section 3.3.1, the effect range ($<$ 545 nm) to absorb the light was discussed for bare 3C-SiC corresponding to the band-gap value. Although UV-Vis absorption for Pt particles/3C-SiC is higher than bare 3C-SiC above the 503 nm, UV-Vis absorption of Pt particles/3C-SiC becomes lower than bare 3C-SiC in wavelength shorter than 503 nm in the effective range. It means the improvement of PEC property by Pt particles is not caused by absorption effect. Next, we show the IPCE results as shown in Figure 4.6(b). The photocurrent for IPCE was collected under 1 V (vs. Ag/AgCl) bias. IPCE can be defined as

$$\mathrm{IPCE}(\lambda) = \frac{\left| j_{ph}(\mathrm{mA/cm^2}) \right| \times 1239.8(\mathrm{V} \times \mathrm{nm})}{P_{mono}(\mathrm{mW/cm^2}) \times \lambda(\mathrm{nm})} \tag{4.2}$$

where P_{mono} and λ are power density and the wavelength of the monochromated incident light, respectively, j_{ph} is the photo-current density, and 1239.8 is the multiplication of h (Planck's constant) and c (velocity of light). While UV-Vis absorption for Pt particles/3C-SiC is lower than bare 3C-SiC, Pt particles/3C-SiC shows 0.2 - 0.8 % higher IPCE in the range of wavelength of 412 – 550 nm. The integration of the spectrum for Pt particles/3C-SiC in 400 – 550 nm is ~40 % larger than that of bare 3C-SiC, indicating that contribution to much higher efficiency in visible range. Consequently, the enhanced PEC property is caused by not absorption effect, but improved carrier transport due to band-bending between 3C-SiC and Pt particles. Also, the higher IPCE by Pt particles in visible light range means Pt particles/3C-SiC should more efficiently use the spectrum of solar-light lamp which contains 40 % visible

light in the range of 200 - 800 nm. Namely, Pt NPs hinder the photon absorption, but contribute to improve the PEC reaction in the visible range.

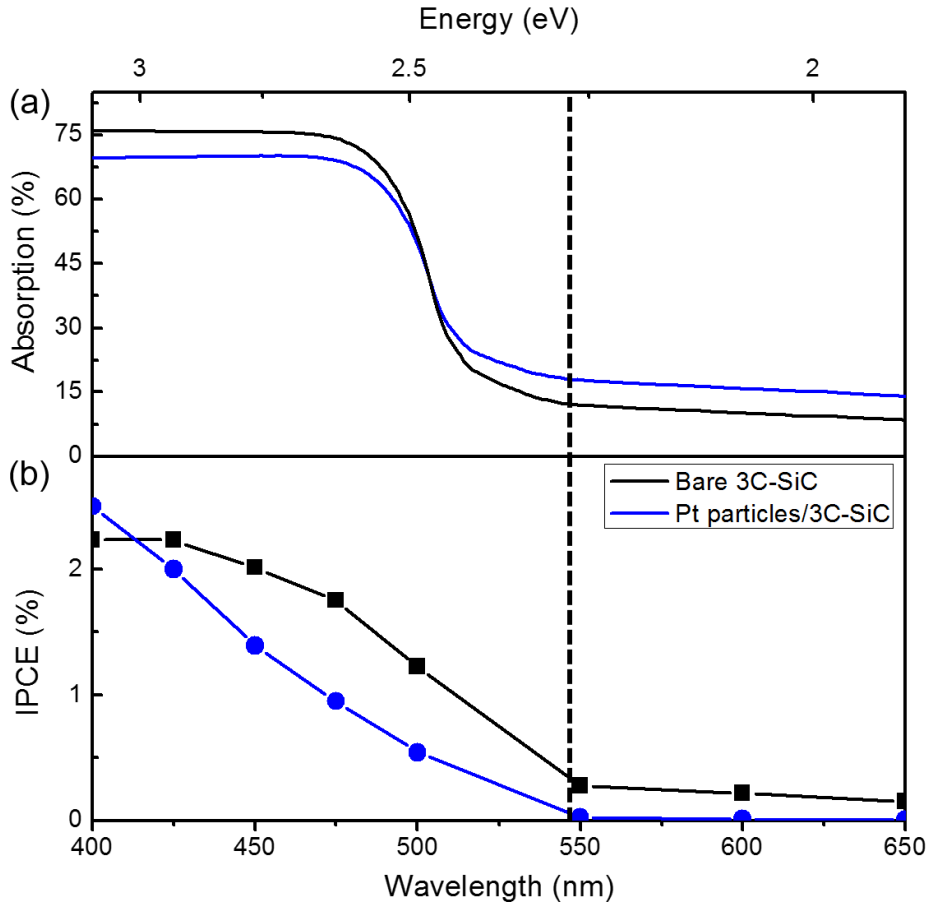

Figure 4.6. Comparison of UV-Vis absorption (a) and IPCE (b) spectra for bare 3C-SiC and Pt particles/3C-SiC. Photocurrent was measured at 1 V (vs. Ag/AgCl) bias for IPCE. Black dotted line indicates the band-gap, 545 nm (2.28 eV).

4.4.3 Gas production analysis

Figure 4.7 shows the results of H_2 gas production amount after PEC reaction with bare 3C-SiC and Pt particles/3C-SiC photo-electrode. Produced H_2 gas were collected after PEC reaction for 10 min at an applied bias of 1 V (vs. Ag/AgCl) with varying incident light power density, separately. The H_2 gas production amount increases linearly with elevation of the light power density for both bare 3C-SiC and Pt particles/3C-SiC proving that the H_2 generation occurs by the PEC reaction. Apparently, the amount of H_2 generation for Pt particles/3C-SiC is larger than bare 3C-SiC. Under the incident light with power density of 492 and 628 mW/cm^2, we obtained about 6.5 times higher H_2 gases for Pt particles/3C-SiC. The difference should mostly come from negligible measurement errors. Even at a lower power density of 355 mW/cm^2, Pt NPs/3C-SiC shows assurable H_2 generation, 2.4 μmol/cm^2, while bare 3C-SiC produces little amount of H_2 gas due to insufficient amount of current flow to measure all generated gas. In addition, Faradaic efficiency of H_2 generation is also improved by Pt particles from 67 % to about 70 %. This improvement should come from the preferential reaction through the Pt particles with suppressing the surface oxidation reaction with Pt particles. Therefore, it is clearly demonstrated that Pt particles contribute improvement of PEC properties for H_2 production.

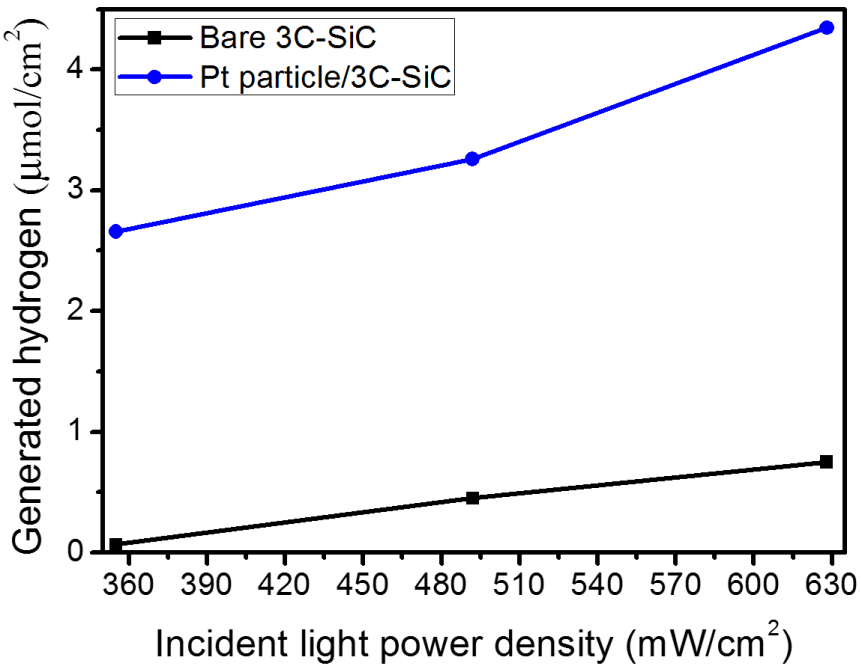

Figure 4.7. Hydrogen production amount generated from counter electrode side in accordance with incident light power density. Incident light power density is 355, 492 and 628 mW/cm^2.

4.5 The evaluation of stability

The time-dependent measurements under light illumination were performed for about 5 hours in order to investigate the stability of bare 3C-SiC and Pt paticles/3C-SiC sample. The dissolution of SiC by surface oxidation reaction was reviewed in Section 3.4.2. In this measurement, bare 3C-SiC and Pt particles/3C-SiC samples were applied by 1.3 V and 1 V (vs. Ag/AgCl), respectively, for comparing two samples in similar electric charge quantity at the same elapsed time. The result of time-dependent measurement is shown in Figure 4.8. The total quantity of electric charge after 5 hours for the bare 3C-SiC is 7 C, same with total

quantity after 2.4 hours for Pt NPs/3C-SiC sample. In spite of lower electric charge flow for bare 3C-SiC, photo-current densities without Pt particles after reaction for about 5 hours decrease by 93 % much higher than 65 %, which is decrease rate for Pt particles/3C-SiC. The photocurrent finally decreases to 0.5 and 0.1 mA/cm^2 with and without the Pt particles, respectively. The state of surface corrosion is also confirmed by optical microscope as shown in Figure 4.9. It is shown that etched groove is formed on surface of the sample without the Pt particles after reaction for 30 min, while surface with the Pt particles shows no damage. Even if the surface with Pt particles shows the corrosion phenomenon after 5 hours corresponding to the decrease of photocurrent with time, it is less severe than bare 3C-SiC. In the result, the degradation is effectively suppressed due to the preferential oxidation reaction at the Pt particles surface.

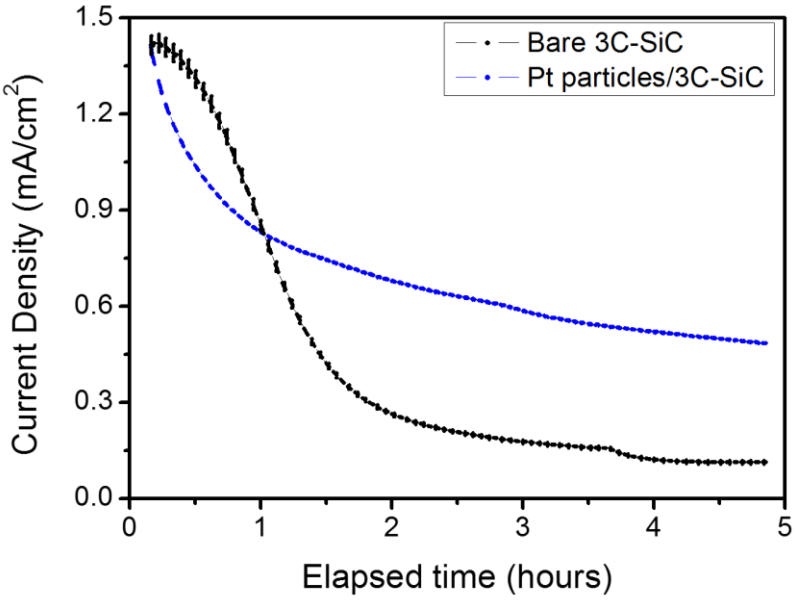

Figure 4.8. Photocurrent density vs. elapsed time for the stability examination of 3C-SiC photo-anode. In order to neglect irrelevant initial reaction, photocurrents after 10 min are considered in this graph (Error bar is expressed (± 0.2 % of currents in precision)).

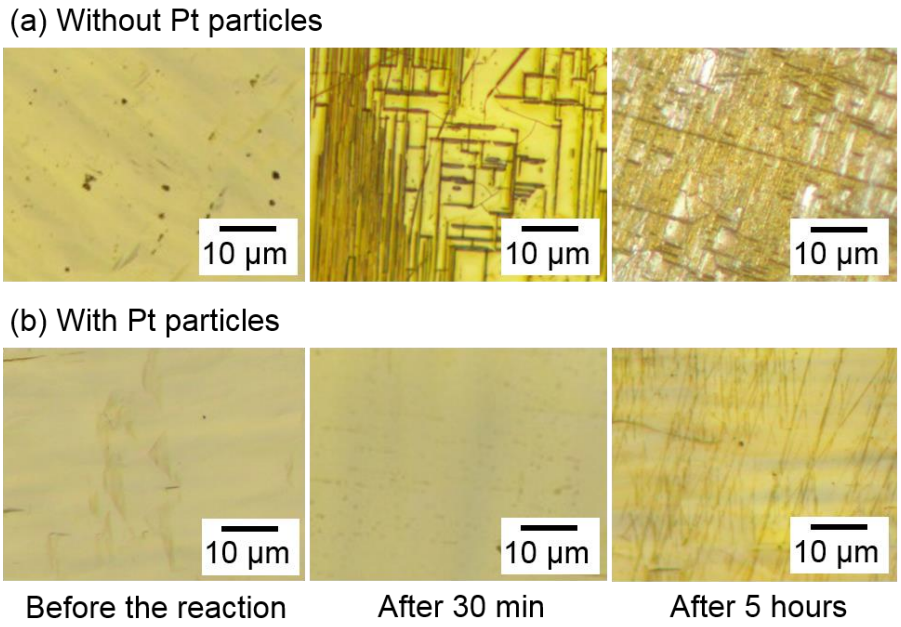

Figure 4.9. Microscope image of the 3C-SiC without and with Pt particles before and after the PEC reaction.

4.6 The effect of annealing condition for Pt particles

4.6.1 The formation of Pt particles with different temperature

In order to investigate the variation of PEC property with Pt particles according to the annealing temperature, we compared the 3C-SiC photo-electrode with Pt particles formed at various temperatures. Figure 4.10 shows the AFM images of the 3C-SiC with Pt samples (Pt/3C-SiC) without and with annealing at various temperatures. From here, Pt/3C-SiC indicate the sample which contains Pt component with layer or particles. A Pt thin film is formed on the surface of Pt/3C-SiC after RF-sputtering without annealing as shown in Figure 4.10(a). After thermal annealing at 500 and 700 ℃, the Pt particles are clearly formed. The characteristic of particles (size and arrangement) depends on the annealing temperature. At the higher temperature, the size becomes larger, exhibiting that the height of Pt particles at 500 and 700 ℃ are approximately 17 and 30 nm, respectively. In contrary, the Pt particles agglomerate completely losing particle structure under the temperature of 900 ℃, which would be caused by the reaction with 3C-SiC and carbon compounds formation as discussed in Section 4.6.3.[72]

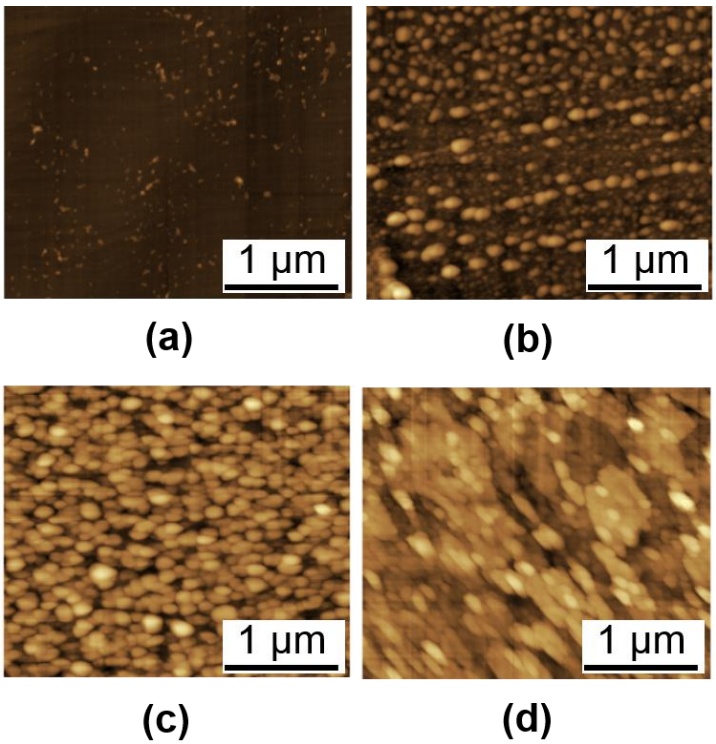

Figure 4.10. AFM images for the comparison of the Pt particle/3C-SiC samples surface state after annealing: (a) no annealing, (b) 500 ℃, (c) 700 ℃, and (d) 900 ℃.

4.6.2 The result of photocurrent characteristic

The samples were evaluated by the voltammetry method and the photocurrents were recorded as a function of potential as shown in Figure 4.11. The photocurrent density of bare 3C-SiC is 0.13 mA/cm^2 at an applied bias of 1 V (vs Ag/AgCl). Bare 3C-SiC has an onset potential of 0.85 V, defined as intercept point of potential axis and fitted line for linear range of the photocurrent curve. Here, Pt/3C-SiC (no annealing) shows a higher photocurrent of 0.87 mA/cm^2 at 1 V and a slightly reduced onset potential of 0.83 V as compared to bare 3C-SiC. Furthermore, the Pt effect is improved by annealing the samples. The Pt/3C-SiC (500 ℃) exhibits the greatest photocurrent, 3.47 mA/cm^2 at the bias of 1 V. The onset potential is lower value, 0.74 V than 0.85 V for bare 3C-SiC. However, the photocurrents in whole

potential range decrease for the samples annealed at 700 ℃ and higher, compared to the Pt/3C-SiC (500 ℃). Although the photocurrent of Pt/3C-SiC (700 ℃) is lower than Pt/3C-SiC (500 ℃), it still shows the higher photocurrent density, 1.19 mA/cm^2 at 1 V and a bit lower onset potential, 0.81 V, than bare 3C-SiC. On the contrary, the Pt/3C-SiC (900 ℃) shows further decrease, 0.07 mA/cm^2 at 1 V, even lower than 0.13 mA/cm^2 for bare 3C-SiC. The onset potential of Pt/3C-SiC (900 ℃) is also larger, 0.97 V, than bare 3C-SiC. Thus, the Pt effect for improving the PEC property disappears at 900 ℃. Here, we discuss the relation between the annealing temperature and photo-activity of Pt/3C-SiC. From the photocurrent measurements, it is shown that PEC properties of Pt/3C-SiC (500 and 700 ℃) are improved compared with Pt/3C-SiC (no annealing). However, annealing at 900 ℃ results in the degradation, showing a lower photocurrent than bare 3C-SiC. First, the enhancement is attributed to the formation of the Pt particles after annealing treatment. Small (~5 nm) and sparse scattered (more than 20 nm) metal particles on the semiconductor electrode have been reported to improve the photo-activity compared to large particles or continuous metal layer on the surface.[73-75] The distribution of particles besides might enhance the light absorption with surface plasmon phenomenon at specific wavelength. Generally, however, Pt is not considered as metal for occurring plasmon effect to enhance light absorption. For detail, we observed the surface structure for the samples with respect to the temperature. The particles at 500 ℃ are the smallest and scattered discretely as shown in Figure 4.10(b). This structure is close to the best case for the metal co-catalyst effect according to the result of above-mentioned previous report.[74, 75] The surface of other samples annealed at higher temperatures becomes complicated with agglomerated structure which would cause the decreased photo-activity.

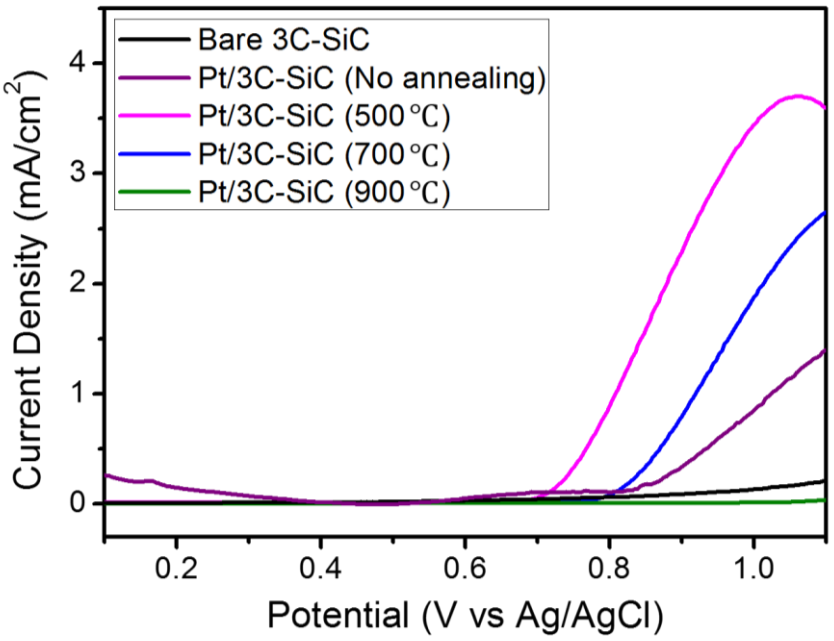

Figure 4.11. Photocurrent vs. potential curves of bare 3C-SiC and Pt/3C-SiC without annealing and with annealed at 500, 700, and 900 ℃. (355 mW/cm^2 of the light power, HCl (pH 1.12))

4.6.3 The analysis of surface state

To reveal the annealing effect on the surface states, we performed XPS measurements as shown in Figure 4.12. The Pt 4f peaks are fitted using a Doniach-Sunjic line shape. Pt/3C-SiC (no annealing) has metallic Pt $4f_{7/2}$ and Pt $4f_{5/2}$ peaks at 71 and 74.3 eV, respectively.[76] It is confirmed that two Pt peaks shift to higher binding energies, 72 – 72.1 eV and 75.3 – 75.5 eV, respectively for all annealed samples. Pt/3C-SiC (500 ℃) have also metallic Pt $4f_{7/2}$ (blue line) and Pt $4f_{5/2}$ (brown line) peaks located at 71.3 and 74.6 eV while Pt/3C-SiC (700 and 900 ℃) show only the completely shifted peaks. These chemical shifts imply the formation of Pt_2Si which is produced by the reaction between Pt and Si in 3C-SiC.[77] It was reported that the Pt_2Si formation at the interface between Pt and SiC resulted in good Schottky

barrier for electrons.[78] It leads to the band-bending for photo-excited holes to transfer to the Pt NPs at a faster rate for the oxidation reaction. Thus, it is considered that Pt/3C-SiC (500 ℃) has optimal contact by proper Pt_2Si formation with showing remarkably diminished onset potential. However, Pt/3C-SiC (no annealing) shows almost same onset potential (0.83 V) as bare 3C-SiC (0.85 V) indicating inappropriate contact without the Pt_2Si formation. Also, the photo-activity performance of Pt/3C-SiC (700 and 900 ℃) with the only Pt_2Si peaks declines as compared to Pt/3C-SiC (500 ℃). Even though Pt/3C-SiC (700 ℃) shows improved photocurrent, it has a similar onset potential of 0.81 V with bare 3C-SiC (0.85 V). Especially, the photocurrent of Pt/3C-SiC (900 ℃) becomes lower than the sample without annealing and even bare 3C-SiC. To investigate the reason of the degradation by high temperature annealing, we carried out Raman spectroscopy measurements (Figure 4.13). Pt/3C-SiC (no annealing) has the same spectrum as bare 3C-SiC. It is confirmed that tiny change at position of G peak (~1590 cm^{-1}, the in-plane stretching of C-C bonds) and a D peak (~1350 cm^{-1}, induced from the disorder at the crystallite boundaries) appear at 500 ℃. Furthermore, the spectrum of Pt/3C-SiC (700 and 900 ℃) clearly have G, D, and 2D (2700 cm^{-1}, the second-order scattering of two-phonon with opposite momenta) peaks, meaning that a considerable amount of carbon materials such as graphite is produced.[79] The increase of the G peak intensity indicates that a higher amount of carbon compounds is synthesized at high temperatures. These carbon compounds should be produced by the remaining carbon (C) from the reaction of Pt with Si in 3C-SiC.[72] The formation of the carbon compounds should occur in the vicinity of the Pt particles, and thus, their excessive evolution causes the destruction of the band-bending at the interface between Pt and 3C-SiC. Therefore, the immoderate high temperature treatment leads to loss of the Pt effect and then the low photo-activity.

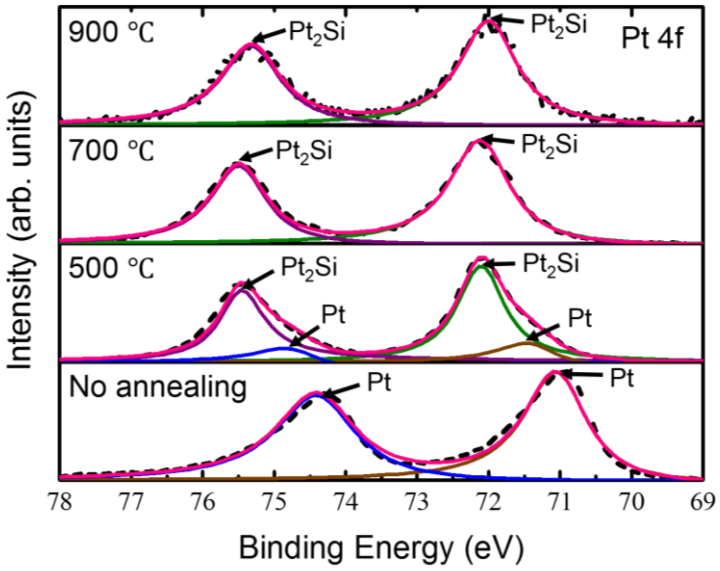

Figure 4.12. Pt 4f XPS spectra with fitting analysis from the samples annealed at different temperatures. The black dotted lines are the original plots from the XPS measurement and the pink lines denote the convolution of fitting curves. (Pt components: brown and blue line, Pt_2Si components: green and purple line)

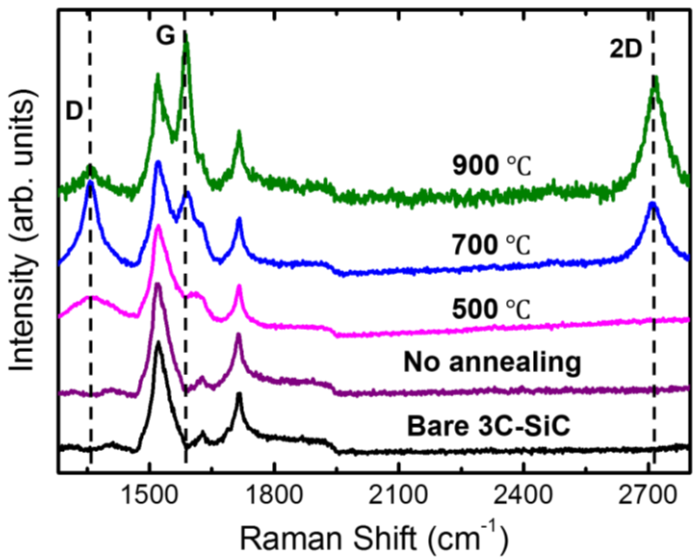

Figure 4.13. Raman spectra of bare 3C-SiC, Pt/3C-SiC (no annealing), and Pt/3C-SiC prepared at different annealing temperatures.

The factors affecting photo-anode properties caused by different annealing temperatures for the Pt effect are summarized with the model of band-diagram in Figure 4.14 as follows: (1) The Pt particles structure: The existence of Pt on the surface induce the Schottky barrier resulting in improved photocurrent (Figure 4.14(a)). Thermal annealing treatment results in the formation of Pt particles structure inducing the improved PEC reaction compared to the sample without annealing. Also, the different particle size and gap between the particles should affect different behavior. Pt/3C-SiC (500 ℃) has the optimized Pt particles structure with showing the greatest PEC property. (2) The production of Pt_2Si at the interface: Onset potential of Pt/3C-SiC (no annealing) is not reduced noticeably as compared to bare 3C-SiC due to the lack of the Pt_2Si formation. The moderate Pt_2Si formation (at 500 ℃) leads to good Schottky barrier for electrons and then band-bending between Pt and 3C-SiC for facile transfer of holes, meaning the enhanced PEC reaction (Figure 4.14(b)). The temperature at 700 ℃ and higher causes the excessive Pt_2Si formation. As a result, the onset potential of Pt/3C-SiC (700 ℃) becomes almost same as bare 3C-SiC despite of improved photocurrent (Figure 4.14(c)). (3) The evolution of carbon compounds: Excessive high temperature causes agglomeration of Pt particles and immoderate evolution of carbon compounds (at 900 ℃), which might hinder the Pt particles effect eliminating the formation of band-bending at the interface between Pt and 3C-SiC (Figure 4.14(d)).

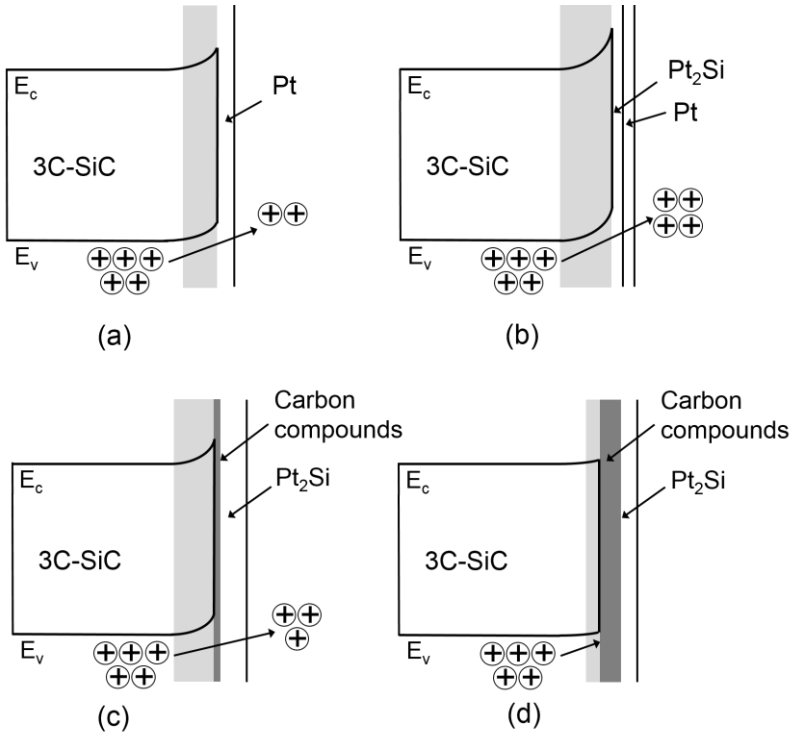

Figure 4.14. Band diagram model of 3C-SiC/Pt sample by various annealing temperature. (a) Potential is induced by Pt deposition on 3C-SiC in case of no annealing, (b) Pt_2Si is produced by annealing at 500 ℃ forming better Schottky barrier, (c) Pt_2Si is excessively formed decreasing the barrier at 700 ℃ (start to form the carbon compounds), and (d) Thick carbon compounds evolve at 900 ℃ and disturb the charge transfer at the interface.

4.7 Suggested future works

As we reviewed about ideal solar-efficiency in Section 3.3.3, there are two large factors affecting the photo-electrode performance inside semiconductor electrode and at interface between semiconductor and electrolyte. In this Chapter, we approach to improve the limitation at interface with Pt particles effect by inducing the potential at the interface of 3C-SiC photo-electrode due to the large overpotential limitation of n-type 3C-SiC semiconductor

for water-splitting. As the result, STH efficiency is improved by 33 times at 1.1 V (vs. RHE) at this moment. However, the STH is still below 0.01 % without applied bias. The ideal efficiency calculation in Section 3.3.3 shows that the efficiency under the consideration for only free-energy loss can be increased from 0.15 % at the loss of 0.6 V to 7.2 % at 0.5 V. Although kinetic loss is certainly important factor for electrochemical reaction, but it shows the generation of photovoltage can be also worked critically. In order to reduce the recombination to minimize the open circuit loss, nanofabrication on the SiC surface can be applied. Second, additional supply of photovoltage with PV can help to improve the total efficiency.[80] In the viewpoint of stability, Pt particles passivate the surface of n-type 3C-SiC against the surface oxidation. However, imperfect passivation is not complete solution because preferred oxidation at defects as discussed in Section 3.4.2. Thus, some exposed surface without Pt particles can be oxidized and it can affect the inside substrate. Finally, it seems that the degradation would be kept even with Pt particles. We need to control the preferred oxidation reaction at stacking fault of 3C-SiC indicating almost 100 % coverage passivation layer. Therefore, Gr passivation layer is expected to be solution for this issue.

4.8 Conclusion

In order to enhance the performance of 3C-SiC photo-anode, it is found that Pt particles as co-catalyst on 3C-SiC surface is attributed to improve carrier transport and stability. Although absorption becomes lower with Pt particles, IPCE is improved in the visible light range. Therefore, the solar-conversion efficiency at applied bias of 1.1 V (vs. RHE) is enhanced by 33 times with Pt particles. Accordingly, H_2 gas generation amount by Pt particles is grown by about 6.5 times with improved Faradaic efficiency from 67 % to 70 %.

Furthermore, Pt particles effectively inhibit degradation of 3C-SiC. In addition, it is demonstrated that the effect of various annealing temperature for Pt particle effect on 3C-SiC photo-anode. The PEC property of Pt/3C-SiC (no annealing) is improved showing a photocurrent of 0.87 mA/cm^2 at 1 V. The annealing process leads to the formation of Pt particles and Pt_2Si resulting in enhancement of the photo-activity with having good contact between Pt and SiC. The sample annealed at 500 ℃ has the maximized photocurrent at 1 V, 3.47 mA/cm^2 and the lowest onset potential, 0.74 V due to the optimal particle structure and contact condition. On the other hands, the sample annealed at 700 ℃ results in lower improvement due to the excessive Pt_2Si formation. Besides, no Pt effect is shown at 900 ℃. It might come from the immoderate evolution of carbon compounds. In conclusion, the Pt particles suggest significant advantages for visible light driven PEC reaction for H_2 generation on 3C-SiC photo-anode with the optimization by annealing temperature. As the future works, the STH efficiency can be further enhanced with improved open-circuit voltage by such a combination of PV structure supplying an additional potential to the PEC device.

Chapter 5
The improvement of stability of 3C-SiC with graphene passivation layer

5.1 Introduction

Most inorganic semiconductors studied for photo-electrode such as Si, GaAs and GaN have suffered from photo-corrosion.[81] According to this problem, various strategies have been proposed for long-term stability. The most widely studied method is to coat the very thin passivation layer which is durable against PEC reaction. It has been reported that thin film passivation of Pd, Pt, NiO, and TiO_2 is effective to yield higher stability.[32, 37, 82] In Chapter 3, it is demonstrated that 3C-SiC photo-electrode is also suffered from the surface oxidation reaction during PEC process. The dissolution of SiC forming SiO_2 causes the degradation of the photocurrent with time. In Chapter 4, Pt particle formation on the surface provides a kind of bypass from the bulk to electrolyte to avoid SiC surface corrosion. Although it is effective to suppress the degradation, it still shows a degradation of photocurrent probably due to some still exposed SiC surface without covered by Pt particles. This result indicates a passivation layer with 100 % coverage is required. In previously studied materials as mentioned above, metal layers generally form improper barriers resulting in negative effects[75, 83]. In the cases of other oxide materials, relatively thick layers required for complete passivation disturb the light absorption. Thus, tunneling barrier is needed for transfer without reducing light absorption. In this context, graphene (Gr) which has been focused with its unique properties for electronic devices is considered as promising material for passivation. It was reported that Gr films can serve corrosion prevention layer of metal surface in the air and solution condition.[84] Also, a layer of Gr has excellent optical property with the transparency of ~ 97 % in the visible light range.[85] Above all, the most beneficial characteristic of Gr for SiC photo-electrode is possibility of epitaxial fabrication on the whole surface of SiC by eliminating Si atom at the high temperature above 1400 ℃.[86-90] Therefore,

Chapter 5. The improvement of stability of 3C-SiC with graphene passivation layer

we investigated the effect of Gr layer on the 3C-SiC photo-electrode as passivation layer in this chapter.

5.2 The expected role of graphene layer

As mentioned in Section 5.1, we need promising passivation layer for the surface of 3C-SiC photo-electrode to prevent SiC surface dissolution. Figure 5.1(a) is schematic of 3C-SiC photo-electrode in aqueous solution with expected PEC process according to the surface condition. Gr layer is formed on the right side of 3C-SiC photo-electrode surface, while it is bare state on the left side. We showed the PEC corrosion reaction on the bare 3C-SiC resulting in SiO_2 formation and etched cracks. The band energy for Gr covered 3C-SiC photo-electrode is modelled as shown in Figure 5.1(b) with work function for Gr of ~4.5 eV (4 eV for 3C-SiC).[91] Therefore, photo-generated carriers in 3C-SiC are expected to pass through the Gr layer which has an excellent carrier transport property (20,000 cm^2/Vs) to the electrolyte. In this way, Gr can serve as a passivation layer against corrosion reaction while minimizing the charge transfer at the interface.

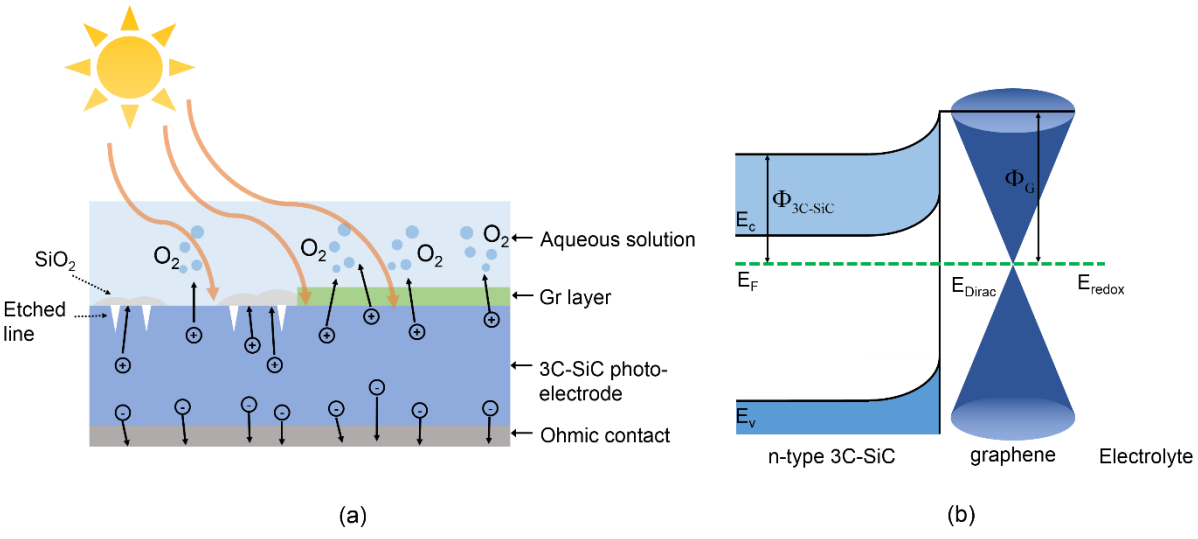

Figure 5.1. (a) Cross-sectional schematic of 3C-SiC photo-electrode in comparison between Gr passivated-surface and exposed-surface to solution. (b) Model of the interface for graphene covered-3C-SiC photo-electrode in solution (**Φ** : work function).

5.3 Epitaxial graphene layer fabrication

Several methods such as micro-mechanical cleavage, exfoliation of graphite, and chemical vapor deposition (CVD) on metal have been reported and developed to the graphene on specific substrates.[92] Although these methods have some advantages, the difficulty to fabricate on large surface or the problem of contamination remain as limitation. In contrary, epitaxial graphene growth on SiC has been focused as promising route for practical application.[87, 89, 93] The process of epitaxial graphene growth is performed by sublimating the Si atoms from SiC with high temperature annealing above the melting point of Si (mainly 1400 – 1650 ℃). Then, remaining C atoms which have much higher melting point (3650 ℃) than Si arrange subsequently with forming graphene layer. The most beneficial issue of this technology is a possibility to cover the graphene passivation layer is realizable on whole SiC surface which is main photo-electrode material in this research. Accordingly, graphene passivation layer were fabricated on the 3C-SiC semiconductor in this research and the properties were investigated.

As the detail of epitaxial graphene growth for photo-electrode, lightly doped 3C-SiC sample was prepared in size of 5 mm × 5 mm. High vacuum chamber with Infrared guide heating system (Thermo Riko) was used for annealing process. Before annealing process, the vacuum degree was set to the 5×10^{-5} Pa. During the process, the atmosphere is varied to the vacuum or the Ar environment (4 kPa of pressure). The temperature of the process is controlled as shown in Figure 5.2. The temperature of chamber increases to 1450 ℃ which is considered as effective temperature for epitaxial graphene growth in 2 min. Then, it is kept for designated time depending on samples and decreased to room temperature with a step of

100 ℃/min (the setting value of control program). We prepared some annealed samples with different atmosphere and annealing time to investigate the effect.

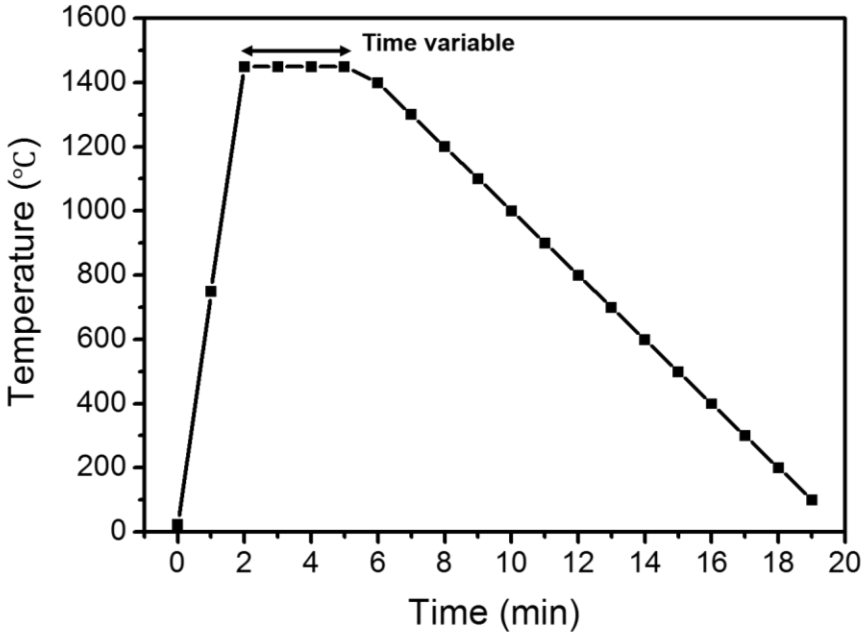

Figure 5.2. The control of temperature during thermal annealing process.

5.4 Surface graphitization by excessive annealing

Figure 5.3 is the Raman spectra of bare 3C-SiC and annealed sample at 1450 ℃ in vacuum state for 30 min. It is shown that 3C-SiC shows the representative peaks at around Raman shift of 1520 cm^{-1} and 1715 cm^{-1} with a few small peaks as shown in Figure 5.3(a). After annealing process, D, G, and 2D peaks which evolve from the graphite are shown with strong intensity while no peak from 3C-SiC is found in Figure 5.3(b). From this result, excessive annealing process forms thick graphite on the surface of 3C-SiC. Figure 5.4 shows the photocurrent characteristic of the graphitized sample by excessive annealing. Basically, it does not show photo-responsivity with no change regardless of light illumination. Also,

the current flows at more than about 1.2 V (vs. Ag/AgCl) even without light illumination. This phenomenon should be originated from the thick graphite which is a kind of metallic layer. Therefore, it suggest we need thin graphene layer for purpose of passivation without disturb the PEC reaction.

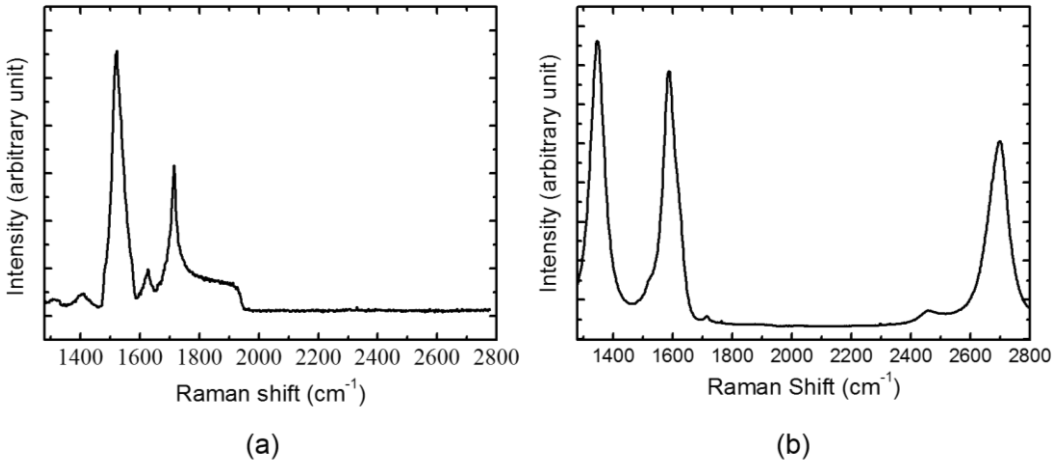

Figure 5.3. Raman spectra of (a) bare 3C-SiC, and (b) thermal annealed 3C-SiC sample in vacuum state for 30 min.

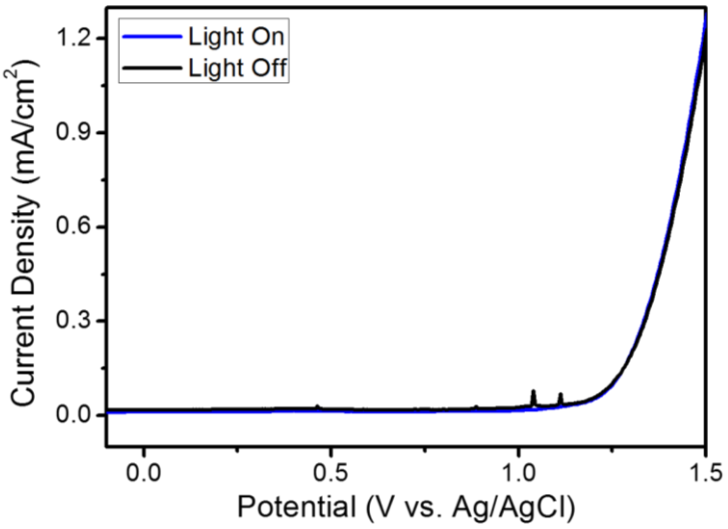

Figure 5.4. Photocurrent vs. potential graph of the annealed sample at 1450 ℃ in the vacuum for 30 min. (HCl electrolyte (pH 1.12), Light power of 355 mW/cm^2)

5.5 The formation of thin graphene layer

5.5.1 The fabrication and analysis of sample

In order to obtain an optimal graphene layer, the annealing process time is shortened to 1, 3, and 5 min. The name of samples are designated by Gr1, Gr3, and Gr5 according to the time from now on. In addition, we performed the annealing process in the Ar atmosphere with pressure of 4 kPa. The presence of the Ar leads to improvement of surface morphology during epitaxial graphene growth. The reason is that a separated Si atoms from the substrate can collide with the Ar atoms and returns to the substrate with finite probability. Thus, the Si evaporation rate will be reduced.[88] The results of Raman spectra for the samples are shown in Figure 5.5. In contrary to the graphitized sample in Section 5.4, the peak from 3C-SiC substrate is observed for all samples. While it is hard to distinguish the G peak, graphene formation can be confirmed by 2D and D peaks. The D peak is shown only for Gr1 and Gr3 with the relative intensity I(SiC)/I(D) of 10.7 and 10.2, respectively. The difference of thickness is roughly judged by comparing I(SiC)/I(2D) of all samples, 22.4, 17.2, and 11.6 for Gr1, Gr3, and Gr5, separately. It indicates Gr5 is estimated to have the lowest defect and the thickest Gr layer among as compared to other samples. For Gr1 and Gr3, annealing time might not be enough to cover the substrate with Gr layer. As a result, discontinuity of graphene sheet (the Gr sheets can be disconnected on some parts) can be a reason of defects. Gr5 can be formed for relatively enough annealing times to reduce the discontinuity for low defects. Here, a clear difference among three samples is distinguished from the Raman shift of 2D peak. As the annealing time increases, 2D peak is red-shifted with annealing time. (Gr1: 2731.8 cm^{-1}, Gr3: 2702.65 cm^{-1}, Gr5: 2688.24 cm^{-1}) It is speculated that it comes from

the improved interaction with substrate while reducing the strain on graphene sheet at longer annealing time.[94]

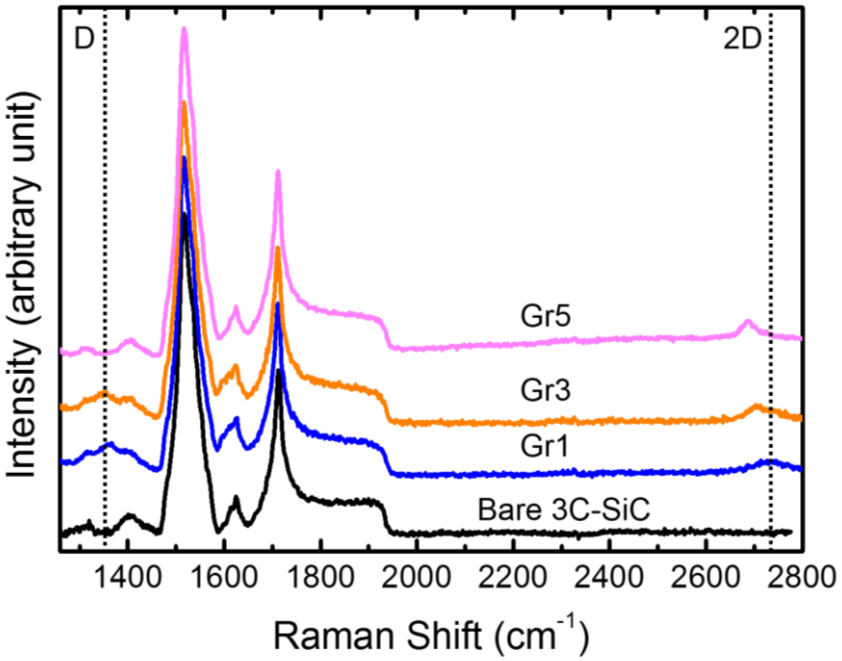

Figure 5.5. Raman spectra of thermal annealed 3C-SiC sample in Ar atmosphere at pressure of 4 kPa with various process time.

In order to understand the uniformity of graphene formation on the whole surface of 3C-SiC, the Raman spectral maps reflecting a distribution of 2D peak intensity (1610 cm^{-1} – 1760 cm^{-1}) for Gr1, Gr3, and Gr5 are acquired before the PEC reaction as shown in Figure 5.6(a) – Figure 5.8(a). The Raman spectra of three labeled points in the map are exhibited in the Figure 5.6(b) – Figure 5.8(b). In the Table 5.1, the relative intensity values of *I*(SiC)/*I*(2D) for each sample are described. In the point 3 of Gr1, it is difficult to calculate the value of *I*(SiC)/*I*(2D) due to almost no 2D peak. Approximately 70 % of whole surface for Gr1 is

covered with the region (black ~ blue color) as shown in Figure 5.6. In case of Gr3 (Figure 5.7), most region (67 %) has I(SiC)/I(2D) of ~ 22 while black colored part (point) also shows a weak 2D peak intensity (I(SiC)/I(2D) of ~ 51). In Figure 5.8 for 5 min of annealing time, the intensity of 2D peak increases all over the region. At the point 1 (red color), the intensity of 2D peak is considerably 5~7 times higher (I(SiC)/I(2D) = ~ 2) as compared to the highest 2D peak in other two samples. I(SiC)/I(2D) of the weakest 2D peak in whole area is calculated to be ~ 8 indicating thicker graphene layer formation than Gr1 and Gr3. Therefore, Gr1 and Gr3 are confirmed to have large area with weak 2D peak while thicker graphene layer is formed on the surface of Gr5 with extended annealing time.

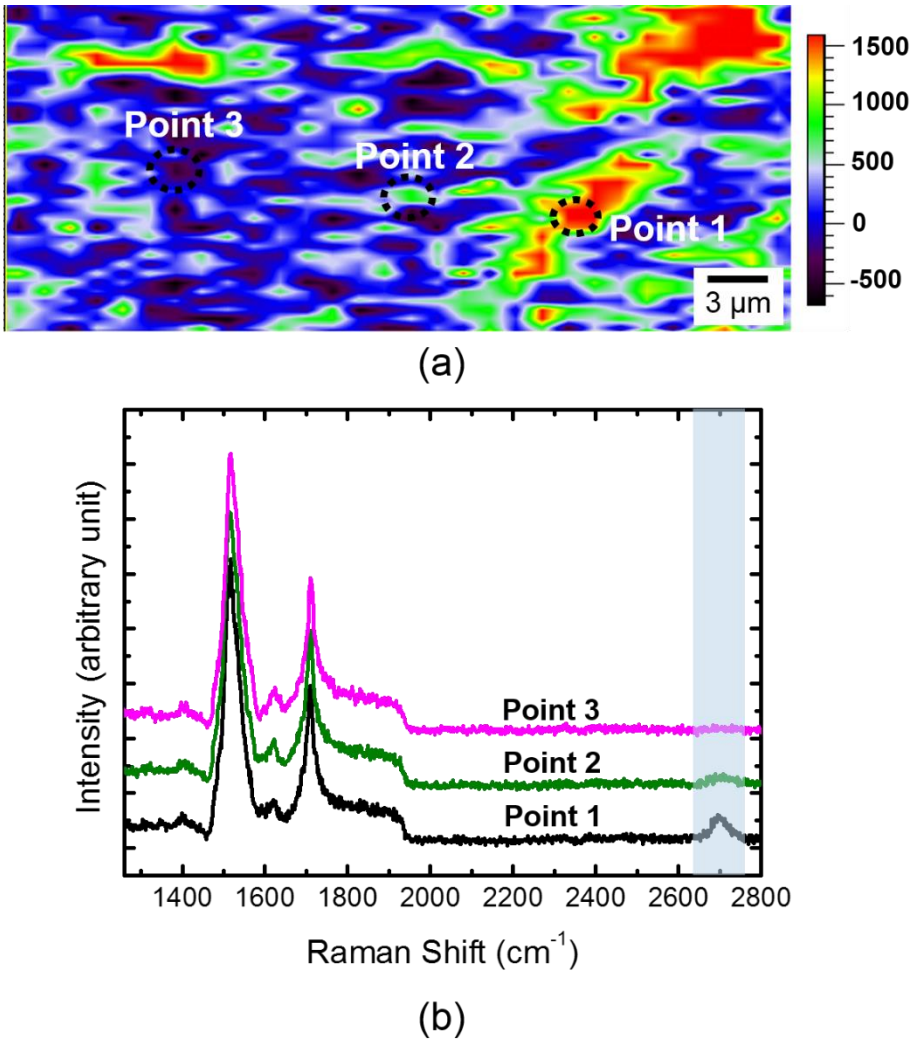

Figure 5.6. (a) Map of the surface for Gr3 reflecting the distribution of 2D peak intensity in the range of 1610 cm^{-1} – 2760 cm^{-1}. (b) Raman spectra corresponds to the labeled three points in the map.

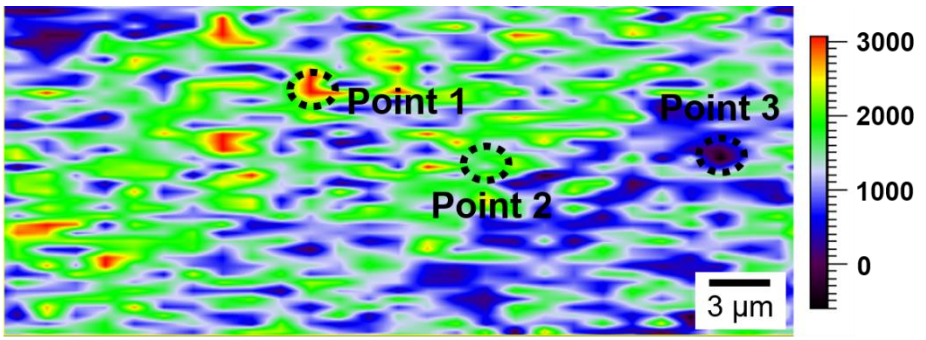

(a)

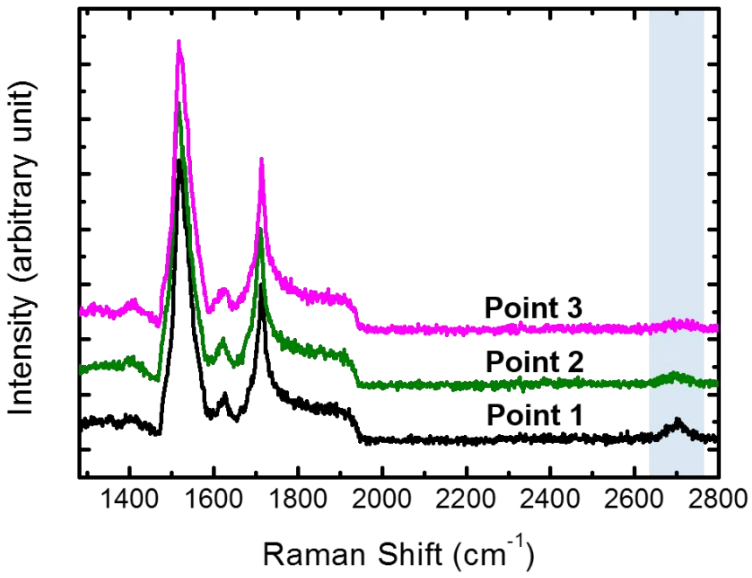

(b)

Figure 5.7. (a) Map of the surface for Gr3 reflecting the distribution of 2D peak intensity in the range of 1610 cm^{-1} – 2760 cm^{-1}. (b) Raman spectra corresponds to the labeled three points in the map.

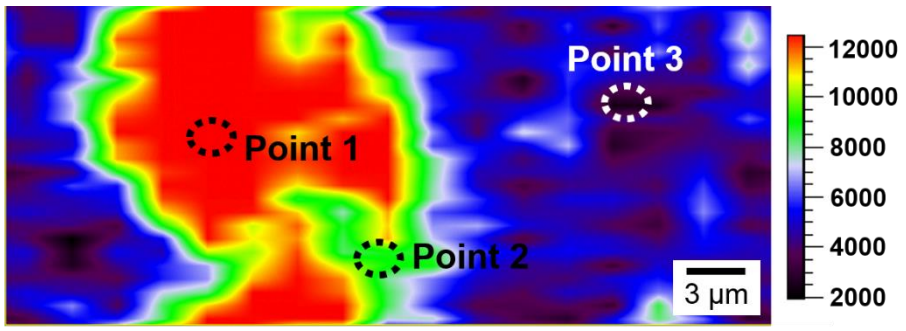

(a)

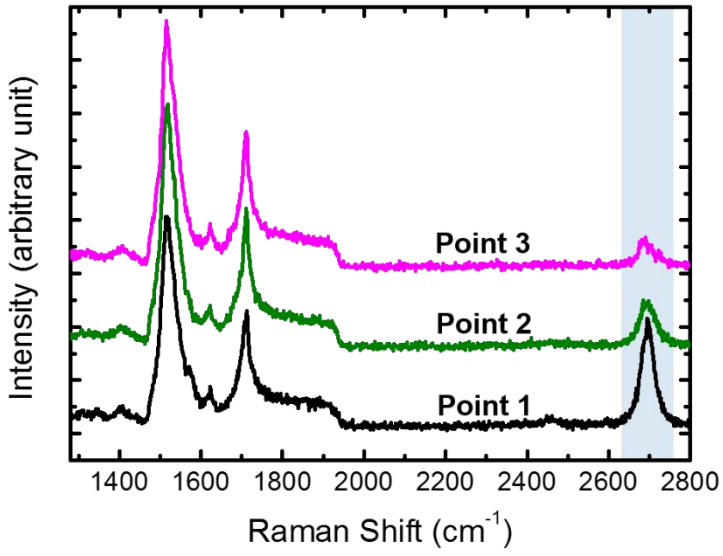

(b)

Figure 5.8. (a) Map of the surface for Gr3 reflecting the distribution of 2D peak intensity in the range of 1610 cm^{-1} – 2760 cm^{-1}. (b) Raman spectra corresponds to the labeled three points in the map.

Table 5.1. The comparison of *I*(SiC)/*I*(2D) for each samples from the result of mapping analysis.

Samples	**Gr1**	**Gr3**	**Gr5**
I(SiC)/*I*(2D) for point 1	11	13	2
I(SiC)/*I*(2D) for point 3	19	22	5
I(SiC)/*I*(2D) for point 5	-	51	8

5.5.2 Photocurrent characteristic of the samples

We investigated the photocurrent characteristic of the samples annealed at the Ar atmosphere in 0.1 M aqueous phosphate solution buffered to pH 7 (KH_2PO_4 + Na_2HPO_4) as shown in Figure 5.9. We note that dark current is almost zero for all samples. Graphene-covered 3C-SiC samples show the degradation of PEC performance at oxidation side. Whereas the onset potential of bare 3C-SiC is 0.5 V (vs. Ag/AgCl), Gr1 and Gr3 show the onset potential of 0.75 V and Gr5 has a 0.65 V. Also, three samples exhibits lowered photocurrent flow than bare 3C-SiC. It is also found that the cathodic currents largely flowed below 0.2 V for Gr5. At more negative bias around -0.3 V, Gr1 and Gr3 has a negative currents while almost no cathodic currents flows for bare 3C-SiC in this range. (Almost similar level of cathodic currents flow under dark condition indicating it is not photocurrents) The larger onset potential and cathodic currents for graphene-covered sample should come from the Fermi-level pinning phenomenon. As shown in Figure 5.10(a), band-bending is ideally formed with general work function of 4 eV for 3C-SiC and 4.5 eV for Gr as discussed in Section 5.2.[91] However, Fermi level has a high probability to be pinned at the surface state in case of semiconductor/metal or epitaxial graphene as shown in Figure 5.10(b).[95] This phenomenon results in degraded PEC performance disturbing carrier transport at lower

potential. It is considered as similar effect with Pt particles annealed at 900 ℃ as discussed in Section 4.6.3. In case of interface of epitaxial graphene and SiC, the reason can be considered as the weak interaction between graphene and substrate due to the lattice mismatch of 3C-SiC (Cubic) and graphene (Hexagonal). Accordingly, buffer layer should be formed at the interface between 3C-SiC and graphene while decoupling the interface during the growth process.[86, 87] As the other reason for the degradation, carrier transportation can be limited at the interface between graphene layer to solution side because graphene material which has a hydrophobic property is unfavorable for direct water-splitting.[96]

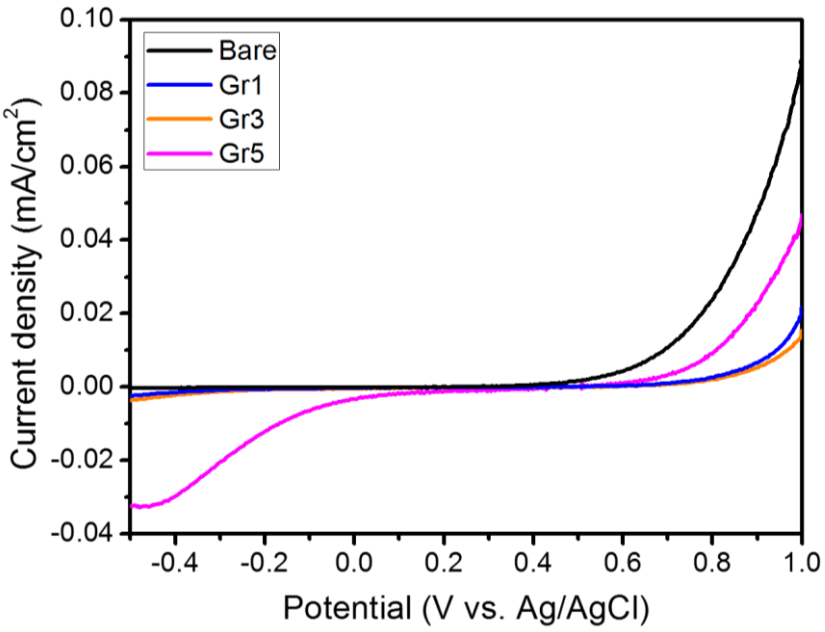

Figure 5.9. Photocurrent characteristics of the bare 3C-SiC and graphene-covered samples. (in electrolyte of phosphate buffer solution (pH 7) and Light power of 100 mW/cm^2)

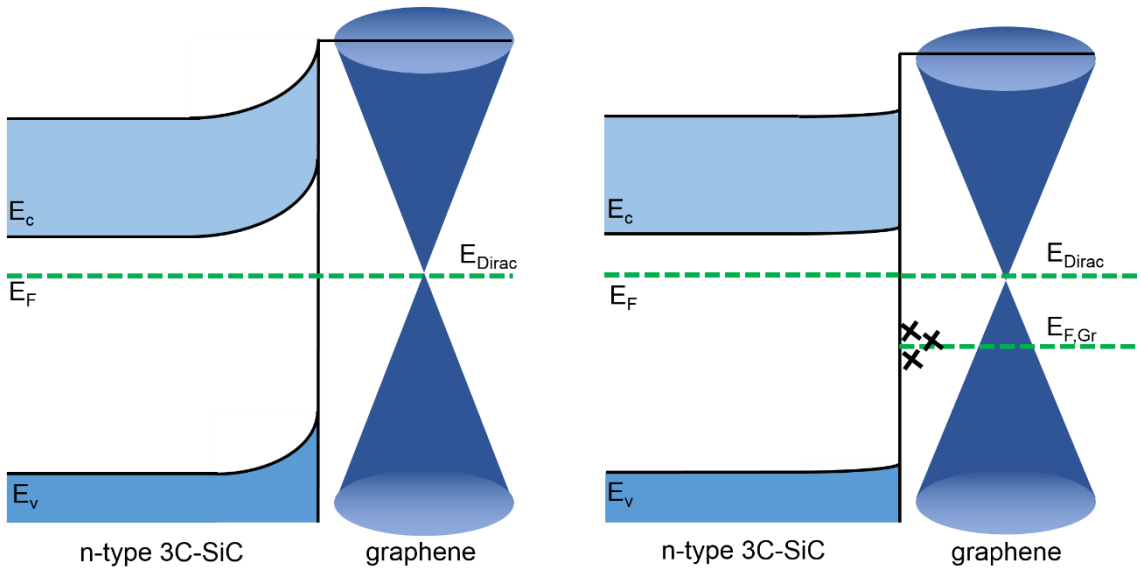

Figure 5.10. Band diagram of the junction for n-type 3C-SiC and graphene. (a) Ideal contact, (b) Case for Fermi level pinning at surface state.

5.6 The evaluation as passivation layer

5.6.1 Surface transition observed by optical microscope

Although photocurrent characteristic is declined with graphene, we implemented the stability examination for graphene-covered sample. In this examination, bare 3C-SiC and Gr5 which shows the largest photocurrent in graphene-covered samples were compared. The change of surface after the PEC reaction at 0.45 V (vs. Ag/AgCl) under the light illumination was observed with optical microscope after passing the electric charge of 0.002 C and 0.004 C in the PEC cell in two steps, separately. As shown in Figure 5.11, the photocurrent of about 0.002 mA/cm^2 flow for bare 3C-SiC for 7500 s. For Gr5, photocurrent decreased by 50 % flows in 0.001 mA/cm^2 for 16500 s. During this process, it is stable without decrease due to its insufficient total charge flow to diminish a current level. Because the photocurrent

level is different according to the samples, elapsed time for PEC reaction was controlled to set the same total flowed electric charge. After PEC reaction, the inspection by optical microscope and Raman spectroscopy is performed to investigate whether PEC reaction attacks graphene layer or not.

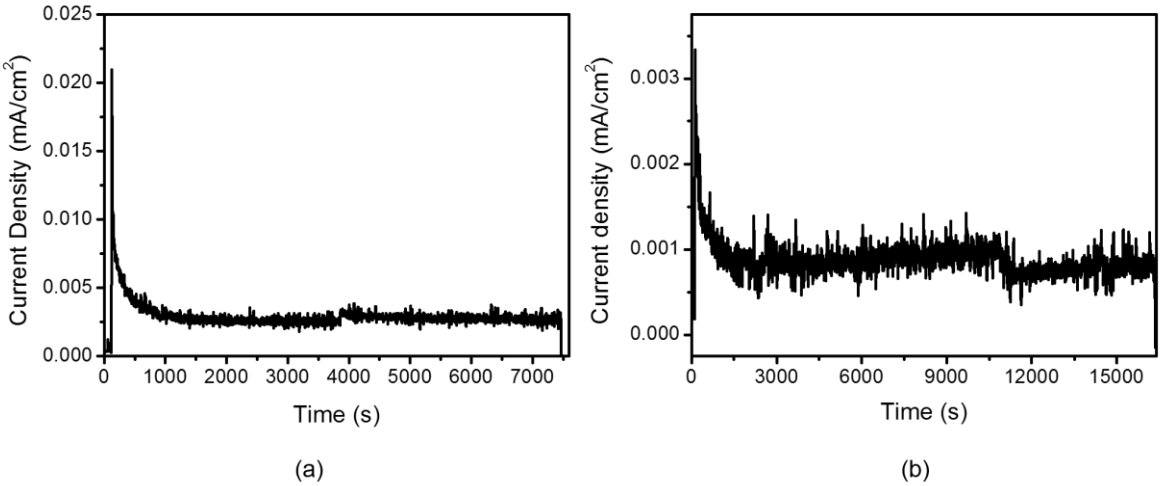

Figure 5.11. Time course of the photocurrent at 0.45 V (vs. Ag/AgCl) for (a) bare 3C-SiC and (b) graphene-covered sample (annealed for 5 min). The discontinuity at around 4000s (a) and 11000s (b) comes from the separate experimental process to observe the surface change as two step.

Figure 5.12 and Figure 5.13 show the images for surface of bare and Gr5 sample before and after the PEC reaction. After 0.002 C of electric charge flow, the surface for bare 3C-SiC is normal, while etched lines occurred by surface corrosion were discovered on the surface of Gr5. However, it is shown that some parts remain as normal without corrosion for Gr5 sample. After 0.004 C, the phenomenon of corrosion is also shown all over the whole surface for bare 3C-SiC sample. In this step, approximately 45 % (estimated with including other images except for used image in this thesis) of area is still stable against corrosion reaction.

In these results, it is shown that some surfaces of graphene-covered sample are not changed after PEC reaction. However, the other parts are corroded even faster than bare 3C-SiC (0.002 C).

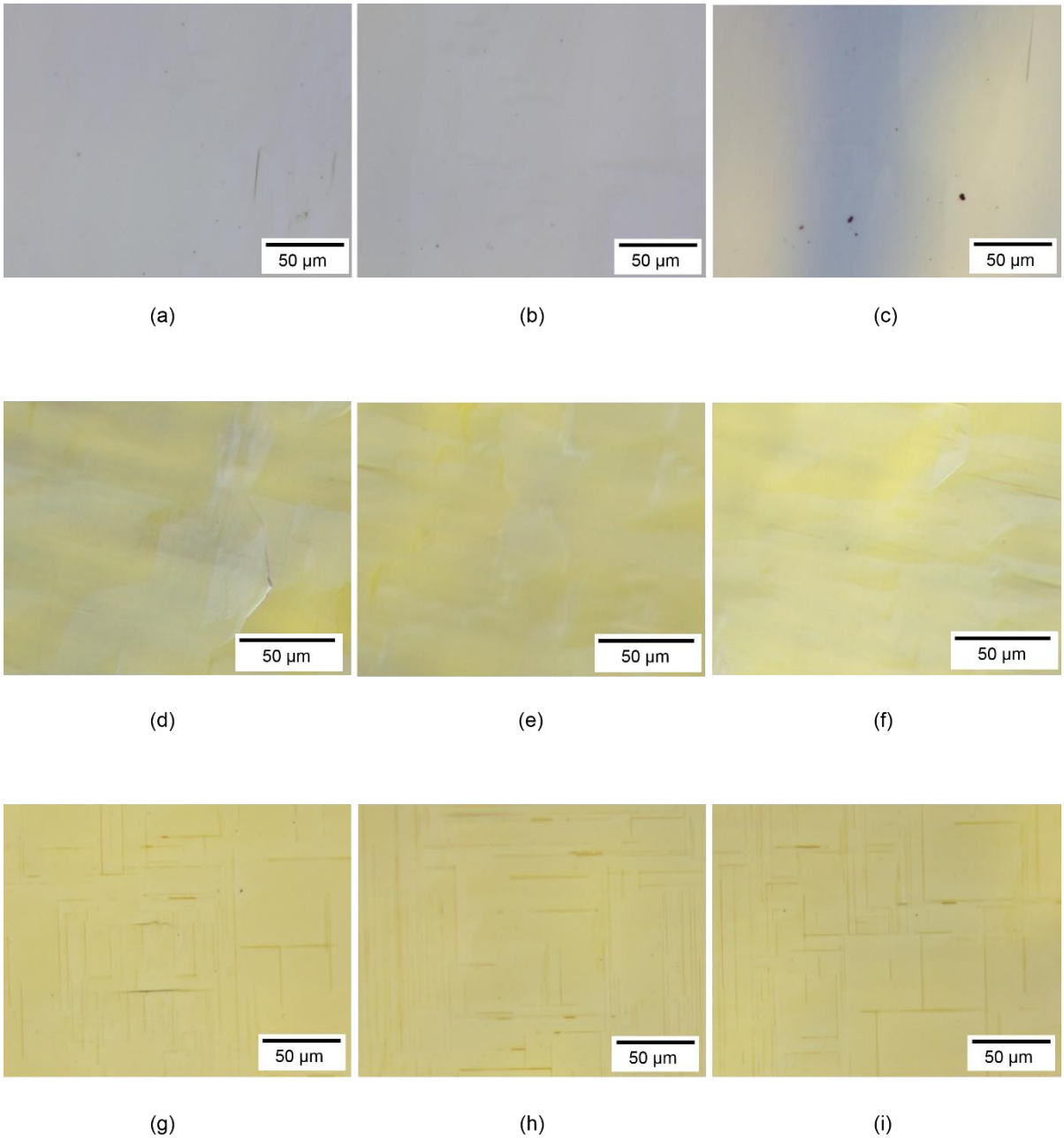

Figure 5.12. Optical microscope image of bare 3C-SiC. (a) – (c) Before reaction, (d) – (f) After 0.002 C, and (g) – (i) After 0.004 C. Three different places are observed to investigate location dependence at each step.

Figure 5.13. Optical microscope image of Gr5 sample. (a) – (c) Before reaction, (d) – (f) After 0.002 C, and (g) – (i) After 0.004 C. Three different places are observed to investigate location dependence at each step. The color difference should come from the state of backside.

5.6.2 Raman spectral analysis

For further investigation of the change for the Gr5 sample after PEC reaction, Raman spectra were analyzed for comparison of unchanged and changed region as shown in Figure 5.14. Point 1 is one of the normal regions and point 2 is in the corroded region, especially above the etched crack.

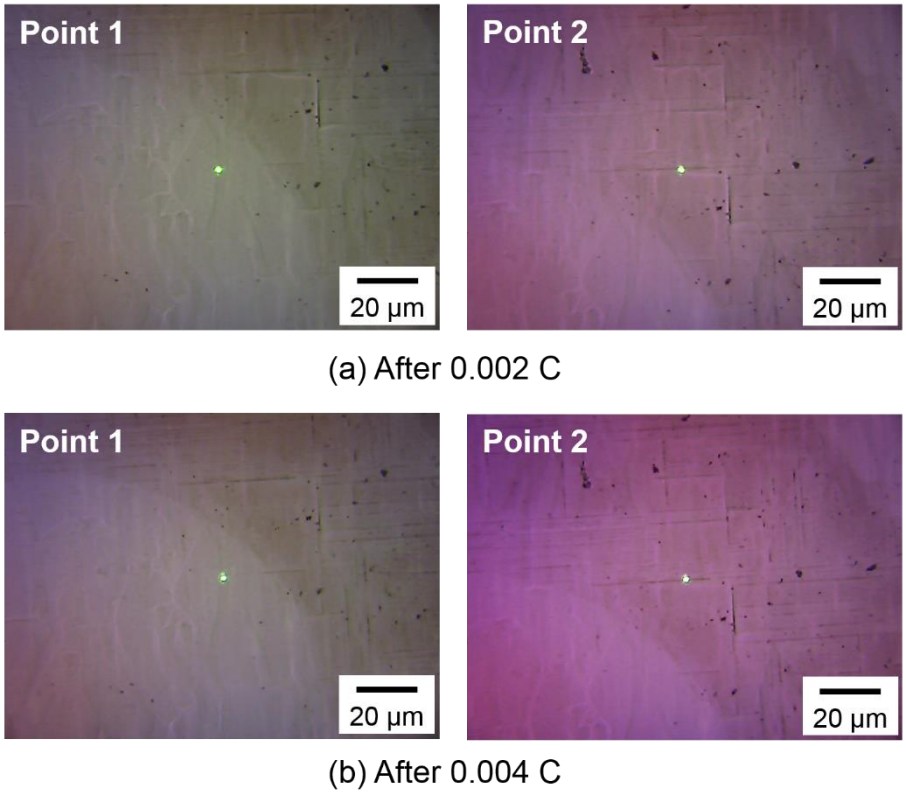

Figure 5.14. The measurement point of Raman spectra for unchanged and changed region. Green laser point indicates the target.

Figure 5.15 shows the result of Raman spectra for designated points of Gr5 sample. First of all, the existence of 2D peak is shown even after PEC reaction for both points indicating Gr layer is not removed by PEC reaction. Especially, the location of 2D peaks for

point 2 (corroded part) is blue-shifted from 2692.91 cm^{-1} to 2698.28 cm^{-1} (5.37 cm^{-1}). In point 1, no shift is found in 2D peak. It is known that blue-shift in 2D peaks originates from the compressive stress or doping in the graphene.[97] After PEC reaction of photo-electrode, SiO_2 or etched cracks caused by a corrosion reaction should be formed underneath graphene layer on 3C-SiC. Eventually, it results in the stress to the upper graphene layer.

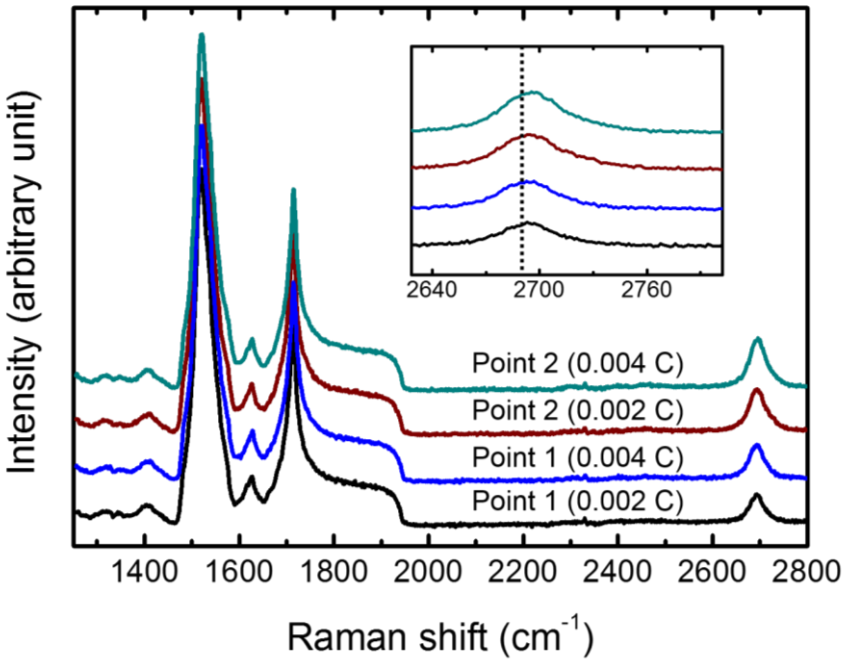

Figure 5.15. The Raman spectra of Gr5 samples after PEC reaction in two steps. Inset is the magnified spectra of 2D peak.

Raman spectral mapping was performed for Gr5 sample after PEC reaction to investigate the spectral difference between normal and damaged region. Figure 5.16 is the result of mapping analysis with the 2D peak intensity. The map in Figure 5.16(b) corresponds the designated region (Figure 5.16(a)). The distribution of 2D peak is not separated completely as actual image of region shows clear difference between undamaged and damaged area. However, this area includes larger portion of the parts with lower 2D peak intensity (blue area) as compared to the unchanged region. That is, the uniformity of graphene is lower than unchanged region resulting in the probability that the many cracks in graphene sheets exist in this area might be higher than the other region.

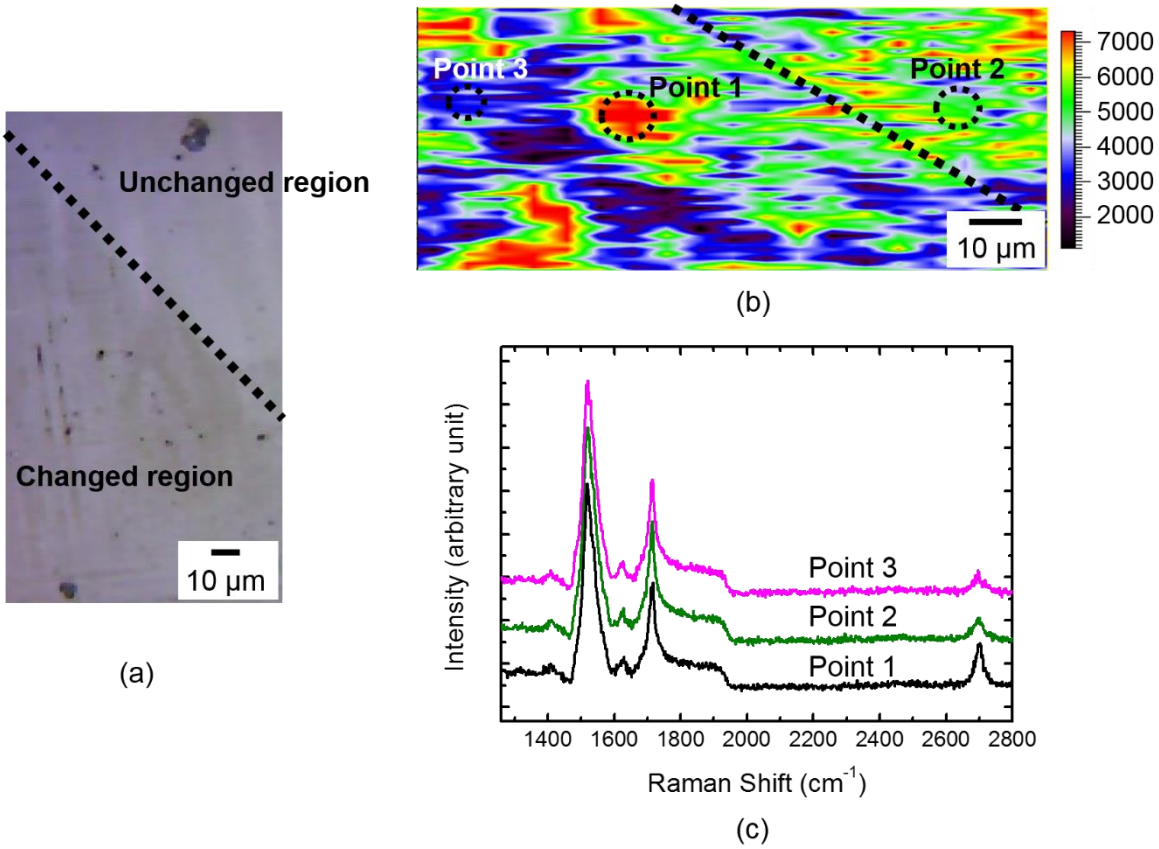

Figure 5.16. (a) The optical microscope image for surface region analyzed by Raman spectral mapping, (b) The map of distribution for 2D peak intensity (1610 – 1760 cm^{-1}) corresponding the designated region, (c) Raman spectra for labeled point in the map.

5.7 Overall discussion of the results

Graphene-covered 3C-SiC photo-electrode shows the degradation of photo-responsivity regardless of annealing process time. In direct comparison of photocurrent level, Gr5 sample shows the 50 % decreased current at 0.45 V (vs. Ag/AgCl) than 3C-SiC. The problems causing degradation can be considered as two parts, graphene and 3C-SiC contact issue and hydrophobic property of graphene. First, improper interaction from the Fermi pinning and electric decoupling at interface can disturb the carrier transfer from the 3C-SiC to graphene layer. Second, hydrophobic property of graphene shows low catalytic ability for direct water-splitting. In the viewpoint of stability, it shows the dependence on surface region. A 45 % in whole surface is not damaged after PEC reaction, while the etched cracks caused by corrosion are shown on the other surface. Regardless of position on the surface, however, the 2D peak in Raman spectra is not changed after PEC reaction indicating graphene layer is not damaged. Under these considerations, it seems that almost no current flows through the 45 % in normal regions for Gr5 after PEC reaction in accordance with decrease rate of photocurrents (50 %) probably due to the isolation from substrate. On the other hands, photocurrents flow through damaged surfaces. Here, corrosion reaction occurs underneath graphene layer due to invaded water molecules through grain boundaries at graphene sheets. The hydrophobic property of graphene layer promotes the SiC surface oxidation preferentially than water-splitting reaction. Thus, the corrosion reaction is observed relatively faster than bare 3C-SiC sample. Although the effect of graphene as passivation layer is still controversial from current results, the possibility to be a passivation layer is shown because graphene layer itself is not attacked during the reaction.

5.8 Suggested future works

5.8.1 Further analysis and optimization of graphene layer

The most necessary problem to be solved is a surface corrosion phenomenon. The efforts of graphene needs to be optimized especially for interaction issue. Before optimization, the interaction status between 3C-SiC substrate and graphene layer has to be analyzed. Such a low-energy electron microscopy (LEEM) can provide the evidence for graphene layer structure on the substrate.[98] The considered reason to block the electrical connection is an interfacial buffer layer expected to be formed during epitaxial graphene growth. It is known to be insulating due to the carbon atoms combined to the substrate covalently. This layer can be broken by annealing at H_2 atmosphere.[99] Therefore H_2 annealing treatment will lead to better interaction between 3C-SiC and graphene layer. Next, we can combine the graphene layer with catalytic materials such as Pt or oxide semiconductor and oxidize the surface of graphene for better catalytic ability. Especially, oxidized graphene (GO) has a hydrophilic property, so it is more proper than original graphene. Graphene layer can be oxidized by UV-Ozone oxidation with optimizing not to be etched by excessive treatment.[100]

5.8.2 p-type 3C-SiC as photo-cathode

Currently, we strongly need the passivation layer for n-type 3C-SiC photo-anode because oxidation reaction is driven at the surface of photo-electrode. If we utilized p-type semiconductor, reduction reaction occurs at the semiconductor surface while eliminating the cause of the corrosion ultimately.[53] Even if there should be limitations such as a difficult to

Al doping for p-type 3C-SiC and lower carrier mobility, it is expected to solve the life-time issue at least.

5.9 Conclusion

We investigated the effect of graphene layer towards passivation role of the 3C-SiC semiconductor for the photo-electrode application. Epitaxial graphene was fabricated on 3C-SiC by high temperature annealing process. In the PEC property, the photocurrent level of graphene-covered samples does not reach to bare 3C-SiC due to the interaction problem originated from lattice mismatch and hydrophobic property of graphene. In the time-dependent current examination in comparison of bare and Gr5 samples, Gr5 samples show faster corrosion phenomenon than bare sample (at 0.002 C). After finishing the experiment (0.004 C), however, the surface of 47 % for Gr5 shows no damage while the trace of corrosion reaction appears on the other parts. Nevertheless, the graphene layer on both undamaged and damaged surface should not be attacked directly. In the case of damaged surface, 2D peak of graphene is blue-shifted indicating the graphene layer is stressed by SiO_2 formation or etched cracks underneath graphene. In these results, carrier transfer should be blocked in undamaged surface while photocurrent flow through the damaged surface. It seems that preferential surface oxidation occurs than water-splitting in total reaction. In conclusion, graphene layer cannot serve as role of perfect passivation. However, graphene layer is not directly attacked during PEC reaction with problems of electric decoupling with 3C-SiC substrate. Therefore, it is expected to be a promising passivation layer with the development of interaction with substrate and combination of Pt particle or oxidized graphene for better catalytic ability. Also, the utility of photo-cathode can be ultimate solution for stability.

Chapter 6
CO_2 reduction system with 3C-SiC photo-electrode

6.1 Introduction

Previous chapters mainly described the PEC property of 3C-SiC photo-electrode for water-splitting which targets of H_2 energy generation. As reviewed about CO_2 gas issue in the Chapter 1, CO_2 reduction technology is very promising way to serve as solution for both useful chemical energy and lessening greenhouse gas. Especially, electrochemical reduction of carbon dioxide (CO_2) has been investigated in various ways due to the necessity to prevent the increase of CO_2, which is the cause for greenhouse effect.[35, 101, 102] In this method, CO_2 can be converted to the chemicals such as formic acid (HCOOH), carbon monoxide (CO), alcohols (CH_3OH), and methane (CH_4) etc. HCOOH, CH_4 and alcohols would be very valuable as an energy source with high density for storage. We reviewed that the CO_2 conversion system can be realized with PEC cell with semiconductor materials in same way with water-splitting in Section 1.5.3. However, two important issues are considered as the obstacles for realizing this system. First, it is highly unfavorable reaction in the thermodynamic and kinetic point of view. Namely, a large potential is required for CO_2 reduction more than water-splitting.[102] Water-splitting easily takes place in the aqueous solution, so CO_2 reduction have to compete with water-splitting in total PEC reaction. Second, most semiconductor materials which have been studied for water-splitting do not have the potential to drive the CO_2 reduction. A few wide band-gap materials show the application for CO_2 reduction.[35, 36, 38, 60, 103] On the other hand, the possibility for not only water-splitting but also CO_2 reduction with 3C-SiC semiconductor was demonstrated in the Chapter 3. In this chapter, the PEC cell for CO_2 reduction with 3C-SiC photo-electrode will be constructed and the produced gases are analyzed.

6.2 The configuration of CO_2 reduction system

Figure 6.1 shows the configuration of PEC cell for CO_2 reduction experiment which is basically same with water-splitting. The photo-electrode of n-type 3C-SiC (Lightly doped sample) was fabricated by same method introduced in Section 3.3. As a counter electrode, platinum (Pt) and silver (Ag) wires (Nilaco) were selected. PEC cell is composed of separated anode and cathode parts by an ion exchange glass filter to prevent an inverse reaction of the products. Both parts contain the same aqueous solution, 100 ml of 0.1 M $KHCO_3$ (pH = 8.5) as a supporting electrolyte. In this configuration, CO_2 reduction occurs at the cathode side by photo-generated carriers in n-type 3C-SiC photo-electrode. That is, water oxidation reaction was driven at the anode side. For realization of the whole PEC reaction, CO_2 gas is injected to cathode side and light is illuminated on the 3C-SiC surface. Then, photocurrent flow is monitored with Potentiostat and gas products are analyzed by micro gas-chromatography.

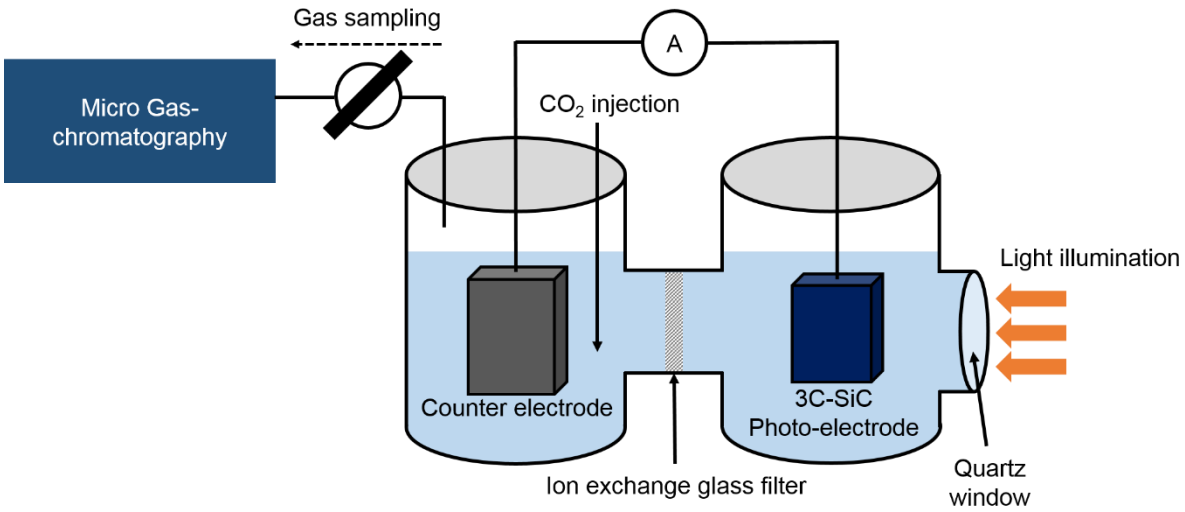

Figure 6.1. The configuration of PEC cell for CO_2 reduction.

6.3 Photocurrent characteristic

First, voltammetry method in the three electrode set-up with Ag/AgCl reference electrode is implemented to investigate the difference of photo-responsivity under the light illumination in the comparison for with and without CO_2 injection. Photocurrent curves against applied potential V (vs. Ag/AgCl) are compared as shown in Figure 6.2. Basically, it is confirmed that photocurrent for 3C-SiC regardless of the type of counter electrodes and the presence of CO_2 is normally flowed under the light illumination while there is almost no current without light (shown only for the case with CO_2). Figure 6.2(a) shows the photocurrent with Pt counter electrode. Without CO_2 bubbling, the photocurrent at an applied bias of 1 V (vs. Ag/AgCl) is 0.71 mA/cm^2. After CO_2 bubbling, it slightly increases to 0.73 mA/cm^2. In the same manner, the Ag counter electrode shows the increased photocurrent at 1 V, 0.69 mA/cm^2 in the presence of CO_2 while the photocurrent is 0.57 mA/cm^2 without CO_2 as shown in Figure 6.2(b). The Ag shows the higher enhancement of photocurrent after CO_2 bubbling than the Pt. The difference of photocurrents before and after CO_2 injection is 0.12 and 0.03 mA/cm^2 for Ag and Pt, respectively.

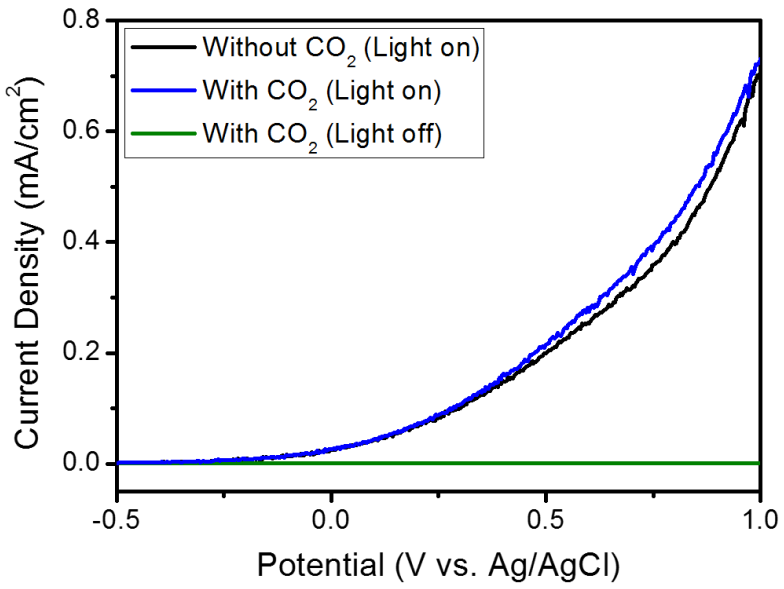

(a)

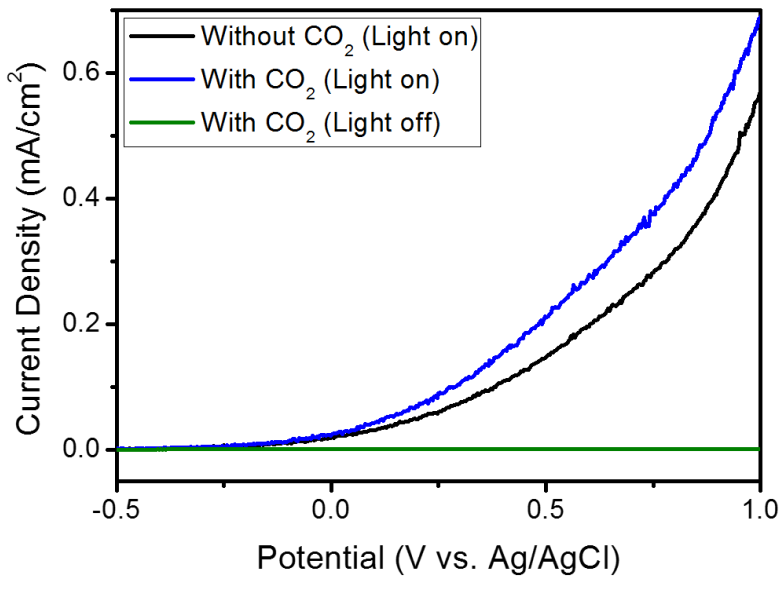

(b)

Figure 6.2. Dependence of the photocurrent characteristic of 3C-SiC photo-anode on the existence of CO_2 injection for (a) Pt and (b) Ag counter electrode. Without light illumination, no photocurrent flowed.

Figure 6.3 shows the difference of photocurrents difference in the potential range from 0.0 V to 1.0 V which shows the change clearly after CO_2 gas injection. The curve of current difference between with and without CO_2 is started to increase from 0.0 V and 0.2 V for Ag and Pt. The factors influencing the PEC reaction after CO_2 reduction are considered as following. The dissolution of CO_2 with an aqueous solution releases the proton which decrease the pH.[104] Therefore, the lowered pH (from pH 8.5 to pH 6.8) in the cathode side after CO_2 bubbling makes the potential difference which acts as chemical bias. More importantly, CO_2 reduction reaction is also added in the total reaction with water-splitting reaction. Due to these causes, photocurrent should be increased.[21, 104] With these consideration, larger increment of photocurrent and lower onset potential of current difference between with and without CO_2 for Ag suggest that preferred CO_2 reduction is induced with Ag counter electrode.

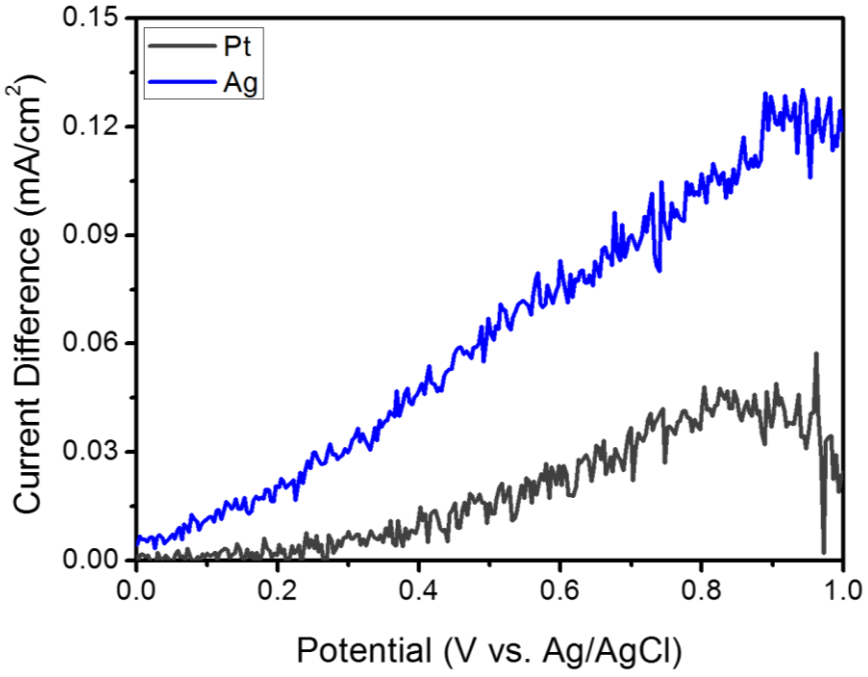

Figure 6.3. The difference of photocurrent between with CO_2 and without CO_2 in the range of 0 - 1 V (vs. Ag/AgCl) for Pt and Ag counter electrode.

6.4 The analysis of gas products

We performed the analysis of gas production after the PEC reaction with 3C-SiC in the presence of CO_2 at the cathode side. This experiment was performed in the two-electrode configuration under an applied bias of 1 V between photo-anode and counter electrode. During the process of the PEC reaction, possible chemical reactions at the counter electrode were expressed without considering any factors to decide the selectivity of the particular reaction in Eq. (1.8) – (1.11). In those producible substances, only gas products especially for H_2 and CO which is detectable are monitored by our GC system as introduced in Section 2.2.5. We examined background test with Ag counter electrode for about 3000 s under the condition without and with light illumination to confirm that no gases evolve without PEC reaction. Figure 6.4 shows the electric signal graph in the range of 0.6 – 1.1 min from the detector of GC as raw result. If CH_4 and CO gas components exist, it should be shown at 0.71 min and 0.88 min, respectively. As the result, no product was generated after the operation over 3000 s without light illumination. However, CO peak is only detected with the condition of light illumination, while it is hard to judge CH_4 peak is detected. For the CH_4 gas, it might not be clearly detected probably due to the limitation of detection level.

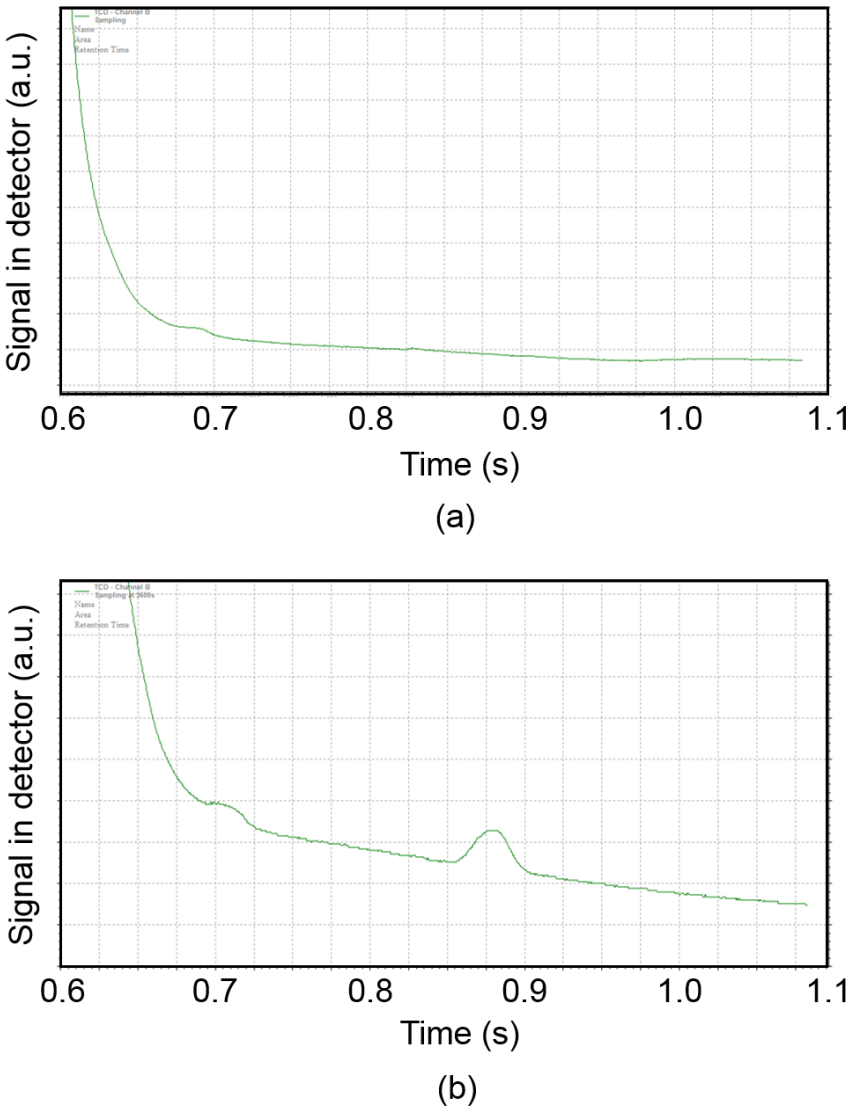

Figure 6.4. The raw electric signal result of gas-chromatography for background confirmation (a) without light illumination, and (b) with light illumination.

The amount of reduction products formed from the PEC reaction were determined with the reaction time as shown in Figure 6.5. The gas sampling from the cathode side of PEC cell was carried out at 1000 s, 2000 s, and 3000 s for the Pt counter electrode. When the Ag was applied to counter electrode, it was evaluated at 1200 s, 2400 s and 3600 s. Then, the gas sampling was repeated additionally at around 1200 s and 2400 s in order to confirm the reproducibility. As the result of PEC reaction, CO gas originated from the reaction of Eq. (1.8) is produced to 0.3 nmol at 1000 s and is grown to the 2.5 nmol at 3000 s with reaction time. Repeated experiment shows somewhat faster generation, 3.8 nmol at 2400 s. H_2 gas generation also increases linearly to 0.05 μmol at 3000 s implying that the water-splitting reaction of Eq. (1.3) occurs. The H_2 gas amount from the additional sampling at 1200 s and 2400 s is 0.012 and 0.045 μmol, respectively, showing same tendency with the first gas sampling result. Similarly to the Pt counter electrode, linear increase of the amount for both H_2 and CO with time is also confirmed for Ag metal. Although the amount of both H_2 and CO slightly diminishes at 2400 s as compared to first examination repeated due to small environmental changes for CO_2 reduction, the linearity of production with time is exhibited at the same way. These results indicate CO_2 reduction occurs forming CO gas with the reaction of water-splitting regardless of cathode type by the generated carriers in 3C-SiC photo-anode under the light illumination. However, each product is generated at the different evolution rate according to the type of metals. The Pt counter electrode shows the almost 4 times faster H_2 evolution rate than the Ag counter electrode. On the other hand, CO production rate for the Ag is 2 times higher as compared to the Pt.

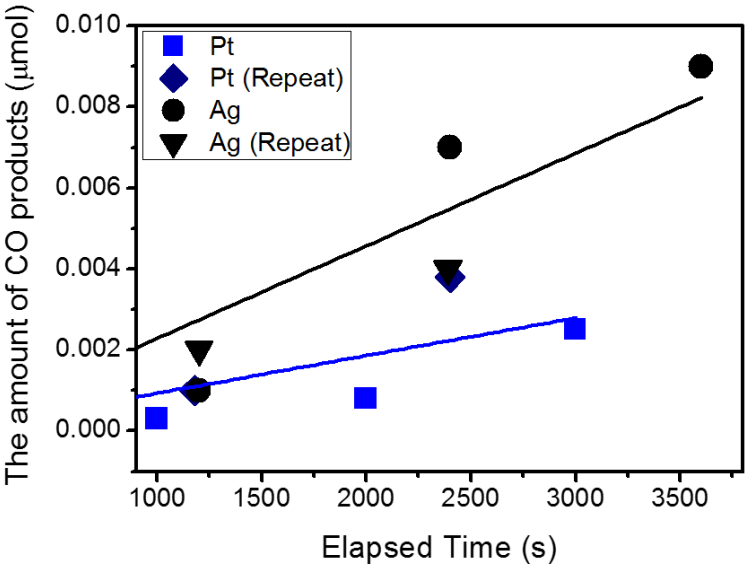

(a) CO

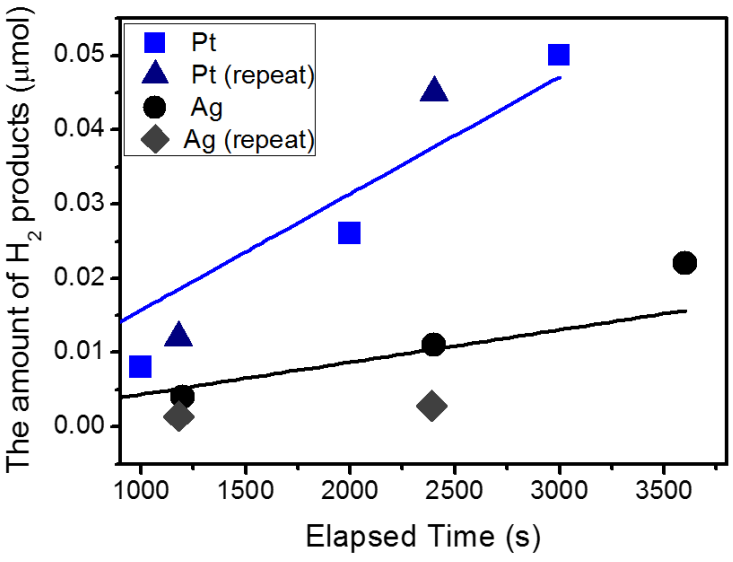

(b) H_2

Figure 6.5. The evolution of products (CO and H_2) with elapsed reaction time depending on the type of counter electrode (Pt and Ag). The marks with 'Repeat' indicates the plots from the experiment of reproducibility. The blue and black lines are fitting curves for all plots of Pt and Ag, separately.

Figure 6.6 shows the comparison of the product ratio of CO to H_2. The product ratio (CO/H_2) for the Pt and Ag is 0.056 and 0.75, respectively. The ratio value (< 1) means water-splitting reaction which is the origin of H_2 generation apparently prevails in the total PEC reaction for both metals. However, the Ag counter electrode exhibits 13.4 times larger ratio than the one of Pt. This result indicates Ag facilitates more CO production than Pt cathode which shows that much more favorable H_2 generation.

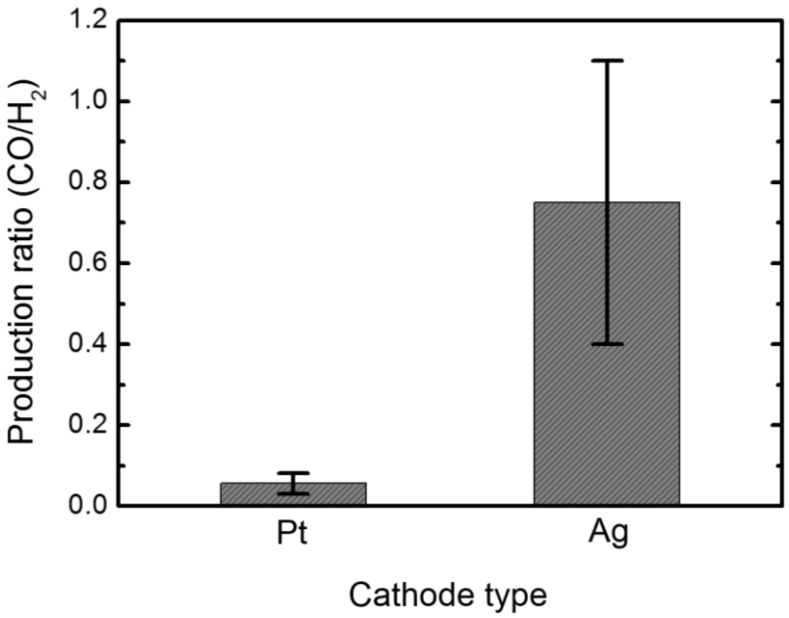

Figure 6.6. The comparison of the ratio of CO to H_2 gas products for Pt and Ag counter electrode.

6.5 Results and Discussion

The values from the photocurrent and gas product analysis are summarized in Table 6.1. Two factors to decide the different phenomenon at the surface metal electrode are proposed considering the natural property of each counter electrode: (1) Overpotential for hydrogen reduction.[21] (2) Binding energy for H atoms.[105] In this PEC reaction, CO_2 reduction occurs competitively with predominant water-splitting. Here, Pt metal is considered to have the lowest overpotential for hydrogen reduction in the various metals, leading to overwhelming H_2 generation.[106] However, Ag metal relatively lower binding energy for hydrogen atoms than Pt.[107] Hence, larger amount of CO_2 might exist around the Ag counter electrode as reactants while more H_2O molecular can be attracted around Pt. These results about selectivity with counter electrode eventually follow to the classification of metals for CO_2 reduction as described in Table 6.2 by Hori et al.[21, 108, 109] In this result, it is significant that light-excited 3C-SiC photo-anode drives the necessary carriers which has potential for CO_2 reduction. The variation with cathode condition should encourage the CO_2 conversion system design with 3C-SiC photo-anode for selective reduction.

Table 6.1. The summary of the results of PEC reaction according to the counter electrode type.

Type of counter electrode	**Pt**	**Ag**
Photocurrent (Without CO_2) at 1 V from Fig. 6.2.	0.70 mA/cm^2	0.57 mA/cm^2
Photocurrent (With CO_2) at 1 V from Fig. 6.2.	0.73 mA/cm^2	0.69 mA/cm^2
Photocurrent (CO_2) – Photocurrent (No CO_2) at 1 V from Fig. 6.2.	0.03 mA/cm^2	0.12 mA/cm^2
H_2 production rate from Fig. 6.5.	0.016 (nmol/s)	0.004 (nmol/s)
CO production rate from Fig. 6.5.	0.001 (nmol/s)	0.002 (nmol/s)

Table 6.2. The reported classification of various products according to the type of metal electrode from electrochemical CO_2 reduction. (Adapted from the reference 109, (Among products, EtOH and PrOH are neglected from the original table.)

Metal	Potential (vs. NHE)	Current density (mAcm^{-2})	Faradaic Efficiency (%)					
			CH_4	C_2H_4	CO	$HCOO^-$	H_2	Total
Pt	-1.07 V	5.0	0	0	0	0.1	95.7	95.8
Ni	-1.48 V	5.0	1.8	0.1	0	1.4	88.9	92.4
Ti	-1.60 V	5.0	0	0	0	0	99.7	99.7
Fe	-0.91 V	5.0	0	0	0	0	94.8	94.8
Cu	-1.44 V	5.0	33.3	25.5	1.3	9.4	20.5	103.5
Ag	-1.37 V	5.0	0	0	81.5	0.8	12.4	94.6
Au	-1.14 V	5.0	0	0	87.1	0.7	10.2	98.0
Zn	-1.54 V	5.0	0	0	79.4	6.1	9.9	95.4
Pd	-1.20 V	5.0	0	0	28.3	2.8	26.2	60.2
Ga	-1.24 V	5.0	0	0	23.2	0	79.0	102.0

6.6 Conclusion

In Chapter 6, we investigated the application of the 3C-SiC photo-anode to PEC CO_2 reduction in the aqueous solution with Pt and Ag counter electrode. 3C-SiC has the potential for CO_2 reduction with the conduction band-edge position confirmed to be located at the more negative level than the potential for producing HCOOH and CO which is at the highest level among materials generated by reducing the CO_2. Based on this possibility, the analysis of gas products (H_2 and CO) was performed with PEC cell at the applied bias of 1 V between photo-anode and counter electrode by GC which is available for direct sampling from the cell. Under the light illumination to the 3C-SiC photo-anode, the amount of H_2 and CO product increases proportionally to the reaction time. However, H_2 production rate is 4 times faster in the case of the Pt counter electrode which has the lowest overpotential for H_2 reduction in metals. For CO generation, 2 times higher rate is obtained by Ag. Moreover, Ag exhibits the 22.5 times higher ratio of CO to H_2, meaning that more CO generation from CO_2 reduction. In conclusion, CO_2 gas is reduced with light illuminated 3C-SiC photo-anode accompanying water-splitting in the aqueous solution. Although gas analysis was performed with the external bias of 1 V due to the limitation of the 3C-SiC material quality affected by defects etc., it is important that 3C-SiC is expected to be promising with the proper band-structure and improvement of material properties. Also, the selective reduction should be possible with the cathode condition as the result of the product ratio by counter electrode.

Chapter 7
General conclusions

7.1 Summary of research

With importance of development for solar-fuel energy resource, photoelectrochemical (PEC) water-splitting and CO_2 reduction with 3C-SiC semiconductor which is fulfilling the basic requirements for the application was evaluated and additionally developed towards the improvement of solar conversion efficiency and stability. We approach to enhance the performance with the effect of Pt particles and graphene passivation layer. Also, PEC CO_2 reduction is demonstrated with analysis of gas products by 3C-SiC photo-electrode. As a result, it is clarified that 3C-SiC semiconductor is significant candidates as promising photo-active materials for the solution of practical PEC device. The summary of each chapter is described as following.

In Chapter 3, we evaluated the potential and current obstacles of 3C-SiC semiconductor as photo-electrode for both water-splitting and CO_2 reduction with investigation of ideal prospective as the beginning of this research. Through the evaluation in respect of ideal solar-conversion efficiency with considering free-energy loss, future prospective and limitation has been reviewed. In the result of PEC characteristic, it is found that overpotential to drive water-splitting at the SiC surface is estimated to be too high 1.2 ~ 1.4 V while general oxide materials generally show the overpotential of 0.2 ~ 0.4 V for oxidation evolving reaction. Also, surface corrosion during PEC reaction is also limited for long-term stability. In Chapter 4 and Chapter 5, the strategies to compensate the current limitation of 3C-SiC photo-electrodes have been proposed.

In Chapter 4, we fabricated Pt particles by sputtering and annealing at 400 ℃ in order to enhance the carrier transport at the interface and surface durability. Importantly, lower onset potential from 1.1 V to 0.7 V indicating reduced overpotential is realized with Pt particles.

Chapter 7. General conclusions

With facile carrier transfer by induced potential between 3C-SiC and Pt particles, solar-to-hydrogen (STH) conversion efficiency at applied bias of 1.1 V (vs. RHE) is greatly improved by 33 times while achieving 0.1 %. In addition, enhanced stability with Pt particles is shown by suppressing the corrosion reaction due to the preferential oxidation at the Pt particle sides. We also presented the variation of Pt particles effect by the different annealing temperature during fabrication process. From the result, it was revealed that the annealing process leads the Pt as particle formation and reaction of Pt and Si resulting in Pt_2Si which is beneficial to have a good contact between Pt and SiC. Specifically, 500 ℃ is considered to develop the optimal contact and particle structure. However, 700 ℃ and 900 ℃ cause the excessive Pt_2Si formation and carbon compounds at the interface, respectively, resulting in lower performance. The Pt particle effect provides a significant role to promote the oxidation with overcoming the limitation of SiC semiconductor.

In Chapter 5, epitaxial graphene was fabricated on the SiC substrate by high temperature annealing at 1450 ℃ with variation of time and atmosphere for passivation. Thin graphene layer in Ar atmosphere is obtained showing a degraded PEC property than bare sample probably due to the Fermi level pinning at interface originated from low interaction with substrate and hydrophobic property. In stability issue, while bare 3C-SiC is suffered from the surface corrosion in whole surface area, 47 % in whole surface for graphene-covered sample (5 min) is not damaged. However, the other areas for graphene-covered sample is corroded even faster than bare 3C-SiC. In the damaged area, 2D peak of Raman spectrum is blue-shifted indicating graphene layer is stressed by SiO_2 or etched line formation underneath graphene layer. It is considered that current flow might be blocked through the undamaged surface because lattice mismatch of 3C-SiC and graphene layer leads to the electrical decoupling. However, surface oxidation occurs on the damaged surface with invasion of

water molecules through grain boundaries than water-splitting due to the hydrophobic property of graphene. Herein, we note that graphene layer itself is not directly attacked from 2D peak intensity. Thus, graphene layer have potential for passivation layer with optimal treatments although these controversial discussion needs more supporting proof. Therefore, it is expected to be improved with solution for the enhanced interaction with substrate and introduction of Pt particles or oxidized graphene for better catalytic ability.

In Chapter 6, we presents the CO_2 reduction system with 3C-SiC photo-electrode with two different counter electrodes (Pt and Ag). The gas products from CO_2 reduction by photo-excited carriers in 3C-SiC photo-electrode were analyzed. Here, we note that gas analysis is performed at applied bias of 1 V between photo-anode and cathode with micro gas-chromatography with high detectivity and fast analysis time enabling the time-dependent measurement without syringe sampling. We confirmed both H_2 and CO gas evolve after PEC reaction. It means water-splitting easily occurs in condition of aqueous solution. However, the product rate is different for Pt and Ag counter electrode. For Pt, 4 times faster H_2 production rate is achieved than Ag, while one of the CO is 2 times faster by Ag. Also, the ratio of CO to H_2 is 22.5 times with Ag electrode indicating Ag counter electrode promotes CO_2 reduction than water-splitting as compared to Pt. It is significant that CO_2 gas is reduced with light-excited carriers of 3C-SiC photo-anode although gas analysis is performed at an external bias of 1 V due to the difficulty at no bias limited by low performance of bare 3C-SiC as we reviewed. These results suggest the importance of 3C-SiC for pathway to obtain chemical energies not only for H_2 but also to decrease greenhouse gas (CO_2).

7.2 Future prospects and issues

7.2.1 Prospective of 3C-SiC for photo-electrode research

In this section, we evaluated the results from this research for 3C-SiC photo-electrode in comparison with current progresses of representative materials reviewed in Section 1.6. Table 7.1 includes the factors from basic fundamental characteristics of each material itself such as available light wavelength, possibility for water-splitting and CO_2 reduction and surface corrosion. STH efficiency and life-time are also described from the recently presented results by other researchers.[27, 30, 37, 43, 110] With diverse approaches to overcome the limitation of various materials, STH efficiency and life-time have been achieved over 1 % and a few hours to some days, respectively. Even if such a development with those materials has progressed over 10 - 30 years since discovery of TiO_2 photo-electrode, it is still far from the commercialization as reviewed in Section 1.3. For the materials such as TiO_2 and GaN which have a possibility for water-splitting or CO_2 reduction, the most dominant obstacle is a limitation of solar-spectrum absorption. We discussed about the ideal efficiency with band-gap in the rage of 1.1 eV to 3.5 eV. The maximum efficiency is not achievable over 2 % above the band-gap of 3 eV. Also, GaN is unique semiconductor meeting the CO_2 reduction potential. For this reason, we compared the prospective of 3C-SiC with GaN in Table 7.2. As mentioned, maximum STH efficiency is overwhelmingly higher for 3C-SiC than GaN due to the band-gap property. We have reviewed the free-energy losses largely affect the achievable efficiency with 3C-SiC photo-electrode. In the range of open circuit voltage loss from 0.5 V to 0.6 V, the efficiency is harshly varied from 7.21 % to 0.15 %. In contrary, GaN has a sufficient large band-gap to avoid the effect of open circuit voltage losses. In actual calculation, maximum STH efficiency of ~ 1 % does not decrease up to 0.6 V of losses.

Chapter 7. General conclusions

Because it has a direct band transition property (relatively lower amount of the loss of open circuit voltage), the effect of free energy loss can be almost neglected. In the viewpoint of prospective for practical device, however, GaN should be applied to with additional absorber material, while 3C-SiC has a bright prospect as single absorber structure.

Under the insufficient investigation for 3C-SiC until now, we have revealed the current limitations and prospective of 3C-SiC photo-electrode which have bright prospective for practical goal, water-splitting and CO_2 reduction. For progress, a 33 times improved solar conversion efficiency, from 0.003 % to 0.1 % by the effect of Pt particles to overcome the overpotential problem is achieved. Also, stability problem is partly enhanced with Pt particles and graphene layer. Although it is currently not enough as compared to presented other materials, it opens to the pathway for the research of significant 3C-SiC photo-electrode towards practical operation.

Table 7.1. The comparison of fundamental factors for PEC device for results of this thesis and other materials from recent published journals.

	Available wavelength	Water-splitting (H_2 generation)	CO_2 reduction	Surface corrosion	STH efficiency	Life-time
TiO_2	< 387 nm	○	×	○	1.2 %	> a few days
$BiVO_4$	< 517 nm	×	×	○	1.72 %	> 50 h
Si	< 1127 nm	×	×	×	2.9 %	> 2 h
GaN	< 365 nm	○	○	×	1.4 %	> 100 h
3C-SiC	< 540 nm	○	○	×	0.1 %	~ 1 h

Table 7.2. Direct comparison of GaN and 3C-SiC as possible materials for CO_2 reduction.

	Ideal STH	Effect of the loss of V_{oc}	Prospective as single-absorber
3C-SiC	~ 13.1 %	A bit large	Bright
GaN	~ 1 %	Too low	Bleak

7.2.2 Summary of future works

As suggested at the end of Chapter 5 and Chapter 6, we need to optimize the improvement of 3C-SiC photo-electrode. As the result of high overpotential for 3C-SiC photo-electrode, Pt effect is proposed to overcome the issue. However, it is also demonstrated that free energy loss largely affect the total efficiency. Therefore, the recombination in device should be minimized by nano-structure of photo-electrode and the combination of photovoltaic will be beneficial to supply an additional photovoltage to cancel out the loss of open circuit voltage. Next, we found the possibility of graphene layer for passivation. But it needs to optimize for perfect passivation with improvement of interaction with 3C-SiC substrate. The remove of buffer layer by H_2 annealing is expected to be solution of this problem. Finally, the development of photo-cathode by using p-type 3C-SiC can serve the ultimate solution for better stability without surface oxidation reaction.

References

1. BP *Statistical Review of World Energy*; London, 2013.

2. Keeling curve. https://scripps.ucsd.edu/programs/keelingcurve/.

3. Hansen, J., R. Ruedy, M. Sato, and K. Lo, GLOBAL SURFACE TEMPERATURE CHANGE. **2010**.

4. The depletion of fossil fuel energy. https://www.ecotricity.co.uk/our-green-energy/energy-independence/the-end-of-fossil-fuels.

5. Administration, U. S. E. I. Electric Power Montly. http://www.eia.gov/electricity/monthly/epm_table_grapher.cfm?t=epmt_1_01_a.

6. Kazmerski, L. *NREL compilation of best research solar cell efficiencies*; National Renewable Energy Laboratory (NREL): 2010.

7. (EIA), E. I. A. *Renewable Energy Consumption and Electricity Preliminary Statistics 2008*; 2009.

8. Abdi, F. F. Towards highly efficient bias-free solar water splitting. TU Delft, 2013.

9. Energy density. http://en.wikipedia.org/wiki/Energy_density.

10. *ENERGY CARRIERS AND CONVERSION SYSTEMS WITHEMPHASIS ON HYDROGEN* 2008; Vol. Vol. 1, p 382.

11. Energy, U. S. D. o. *Fuel Cell Technologies Office Multi-Year Research, Development, and Demonstration Plan*; 2014.

12. Pinaud, B. A.; Benck, J. D.; Seitz, L. C.; Forman, A. J.; Chen, Z.; Deutsch, T. G.; James, B. D.; Baum, K. N.; Baum, G. N.; Ardo, S.; Wang, H.; Miller, E.; Jaramillo, T. F., Technical and economic feasibility of centralized facilities for solar hydrogen production via

photocatalysis and photoelectrochemistry. *Energy & Environmental Science* **2013,** *6* (7), 1983-2002.

13. Fujii, K.; Nakamura, S.; Sugiyama, M.; Watanabe, K.; Bagheri, B.; Nakano, Y., Characteristics of hydrogen generation from water splitting by polymer electrolyte electrochemical cell directly connected with concentrated photovoltaic cell. *International Journal of Hydrogen Energy* **2013,** *38* (34), 14424-14432.

14. Peharz, G.; Dimroth, F.; Wittstadt, U., Solar hydrogen production by water splitting with a conversion efficiency of 18%. *International Journal of Hydrogen Energy* **2007,** *32* (15), 3248-3252.

15. Fujishima, A.; Honda, K., Electrochemical Photolysis of Water at a Semiconductor Electrode. *Nature* **1972,** *238* (5358), 37-38.

16. Khaselev, O.; Turner, J. A., A monolithic photovoltaic-photoelectrochemical device for hydrogen production via water splitting. *Science* **1998,** *280* (5362), 425-427; Licht, S.; Wang, B.; Mukerji, S.; Soga, T.; Umeno, M.; Tributsch, H., Efficient Solar Water Splitting, Exemplified by RuO2-Catalyzed AlGaAs/Si Photoelectrolysis. *The Journal of Physical Chemistry B* **2000,** *104* (38), 8920-8924; Reece, S. Y.; Hamel, J. A.; Sung, K.; Jarvi, T. D.; Esswein, A. J.; Pijpers, J. J. H.; Nocera, D. G., Wireless Solar Water Splitting Using Silicon-Based Semiconductors and Earth-Abundant Catalysts. *Science* **2011,** *334* (6056), 645-648; Rocheleau, R. E.; Miller, E. L.; Misra, A., High-Efficiency Photoelectrochemical Hydrogen Production Using Multijunction Amorphous Silicon Photoelectrodes. *Energy & Fuels* **1998,** *12* (1), 3-10.

17. Tachibana, Y.; Vayssieres, L.; Durrant, J. R., Artificial photosynthesis for solar water-splitting. *Nat Photon* **2012,** *6* (8), 511-518.

18. Maeda, K.; Teramura, K.; Takata, T.; Hara, M.; Saito, N.; Toda, K.; Inoue, Y.; Kobayashi, H.; Domen, K., Overall Water Splitting on (Ga1-xZnx)(N1-xOx) Solid Solution Photocatalyst: Relationship between Physical Properties and Photocatalytic Activity. *The Journal of Physical Chemistry B* **2005,** *109* (43), 20504-20510; Jun, K.; Lee, Y. S.; Buonassisi, T.; Jacobson, J. M., High Photocurrent in Silicon Photoanodes Catalyzed by Iron Oxide Thin Films for Water Oxidation. *Angewandte Chemie International Edition* **2012,** *51* (2), 423-427.

19. Jadhav, B., Chemistry of photoelectrode-electrolyte interface, 2012; Vol. Chapter II; Morrison, S. R., *Electrochemistry at Semiconductor and Oxidized Metal Electrodes*. Plenum Press: New York, 1980.

20. Rajeshwar, K., *Fundamentals of Semiconductor Electrochemistry and Photoelectrochemistry*. Wiley: 2002; Vol. 6, p 608.

21. Hori, Y., *Electrochemical CO2 Reduction on Metal Electrodes*. Springer: New York, 2008; Vol. 42.

22. Seitz, L. C.; Chen, Z.; Forman, A. J.; Pinaud, B. A.; Benck, J. D.; Jaramillo, T. F., Modeling Practical Performance Limits of Photoelectrochemical Water Splitting Based on the Current State of Materials Research. *ChemSusChem* **2014,** *7* (5), 1372-1385.

23. Murphy, A. B.; Barnes, P. R. F.; Randeniya, L. K.; Plumb, I. C.; Grey, I. E.; Horne, M. D.; Glasscock, J. A., Efficiency of solar water splitting using semiconductor electrodes. *International Journal of Hydrogen Energy* **2006,** *31* (14), 1999-2017.

24. Siripala, W.; Ivanovskaya, A.; Jaramillo, T. F.; Baeck, S.-H.; McFarland, E. W., A Cu2O/TiO2 heterojunction thin film cathode for photoelectrocatalysis. *Solar Energy Materials and Solar Cells* **2003,** *77* (3), 229-237; Butler, M. A., Photoelectrolysis and physical properties of the semiconducting electrode WO2. *Journal of Applied Physics* **1977,** *48* (5), 1914-1920.

25. Park, J. H.; Kim, S.; Bard, A. J., Novel Carbon-Doped TiO2 Nanotube Arrays with High Aspect Ratios for Efficient Solar Water Splitting. *Nano Letters* **2005,** *6* (1), 24-28.

26. Hong, S. J.; Lee, S.; Jang, J. S.; Lee, J. S., Heterojunction BiVO4/WO3 electrodes for enhanced photoactivity of water oxidation. *Energy & Environmental Science* **2011,** *4* (5), 1781-1787; Sayama, K.; Nomura, A.; Arai, T.; Sugita, T.; Abe, R.; Yanagida, M.; Oi, T.; Iwasaki, Y.; Abe, Y.; Sugihara, H., Photoelectrochemical Decomposition of Water into H2 and O2 on Porous BiVO4 Thin-Film Electrodes under Visible Light and Significant Effect of Ag Ion Treatment. *The Journal of Physical Chemistry B* **2006,** *110* (23), 11352-11360.

27. Cui, H.; Zhao, W.; Yang, C.; Yin, H.; Lin, T.; Shan, Y.; Xie, Y.; Gu, H.; Huang, F., Black TiO2 nanotube arrays for high-efficiency photoelectrochemical water-splitting. *Journal of Materials Chemistry A* **2014,** *2* (23), 8612-8616.

28. Asahi, R.; Morikawa, T.; Ohwaki, T.; Aoki, K.; Taga, Y., Visible-Light Photocatalysis in Nitrogen-Doped Titanium Oxides. *Science* **2001,** *293* (5528), 269-271.

29. Yuxin Yin and Zhengguo Jin and Feng, H., Enhanced solar water-splitting efficiency using core/sheath heterostructure CdS/TiO 2 nanotube arrays. *Nanotechnology* **2007,** *18* (49), 495608.

30. Kim, T. W.; Choi, K.-S., Nanoporous BiVO4 Photoanodes with Dual-Layer Oxygen Evolution Catalysts for Solar Water Splitting. *Science* **2014,** *343* (6174), 990-994.

31. Kronawitter, C. X.; Vayssieres, L.; Shen, S.; Guo, L.; Wheeler, D. A.; Zhang, J. Z.; Antoun, B. R.; Mao, S. S., A perspective on solar-driven water splitting with all-oxide hetero-nanostructures. *Energy & Environmental Science* **2011,** *4* (10), 3889-3899; Saito, R.; Miseki, Y.; Sayama, K., Highly efficient photoelectrochemical water splitting using a thin film photoanode of BiVO4/SnO2/WO3 multi-composite in a carbonate electrolyte. *Chemical Communications* **2012,** *48* (32), 3833-3835; Hwang, Y. J.; Boukai, A.; Yang, P., High Density

n-Si/n-TiO2 Core/Shell Nanowire Arrays with Enhanced Photoactivity. *Nano Letters* **2008,** *9* (1), 410-415.

32. Kenney, M. J.; Gong, M.; Li, Y.; Wu, J. Z.; Feng, J.; Lanza, M.; Dai, H., High-Performance Silicon Photoanodes Passivated with Ultrathin Nickel Films for Water Oxidation. *Science* **2013,** *342* (6160), 836-840; Hu, S.; Shaner, M. R.; Beardslee, J. A.; Lichterman, M.; Brunschwig, B. S.; Lewis, N. S., Amorphous TiO2 coatings stabilize Si, GaAs, and GaP photoanodes for efficient water oxidation. *Science* **2014,** *344* (6187), 1005-1009; Chen, Y. W.; Prange, J. D.; Dühnen, S.; Park, Y.; Gunji, M.; Chidsey, C. E. D.; McIntyre, P. C., Atomic layer-deposited tunnel oxide stabilizes silicon photoanodes for water oxidation. *Nat Mater* **2011,** *10* (7), 539-544.

33. van de Krol, R.; Liang, Y., An n-Si/n-Fe 2 O 3 Heterojunction Tandem Photoanode for Solar Water Splitting. *CHIMIA International Journal for Chemistry* **2013,** *67* (3), 168-171.

34. Katsushi Fujii and Takeshi Karasawa and Kazuhiro, O., Hydrogen Gas Generation by Splitting Aqueous Water Using n-Type GaN Photoelectrode with Anodic Oxidation. *Japanese Journal of Applied Physics* **2005,** *44* (4L), L543; Yotsuhashi, S.; Deguchi, M.; Hashiba, H.; Zenitani, Y.; Hinogami, R.; Yamada, Y.; Ohkawa, K., Enhanced CO2 reduction capability in an AlGaN/GaN photoelectrode. *Applied Physics Letters* **2012,** *100* (24), -.

35. Satoshi Yotsuhashi and Masahiro Deguchi and Yuji Zenitani and Reiko Hinogami and Hiroshi Hashiba and Yuka Yamada and Kazuhiro, O., Photo-induced CO 2 Reduction with GaN Electrode in Aqueous System. *Applied Physics Express* **2011,** *4* (11), 117101.

36. Sayama, K.; Arakawa, H., Photocatalytic decomposition of water and photocatalytic reduction of carbon dioxide over zirconia catalyst. *The Journal of Physical Chemistry* **1993,** *97* (3), 531-533.

37. Tomoe Hayashi and Momoko Deura and Kazuhiro, O., High Stability and Efficiency of GaN Photocatalyst for Hydrogen Generation from Water. *Japanese Journal of Applied Physics* **2012,** *51* (11R), 112601.

38. Masahiro Deguchi and Satoshi Yotsuhashi and Hiroshi Hashiba and Yuka Yamada and Kazuhiro, O., Enhanced Capability of Photoelectrochemical CO 2 Conversion System Using an AlGaN/GaN Photoelectrode. *Japanese Journal of Applied Physics* **2013,** *52* (8S), 08JF07.

39. SiC classification. http://www.semiconductorwafers.net/SiC-Crystallography--Important-Polytypes-and-Definitions.html.

40. Eriksson, J. Transport properties of 3C-SiC interfaces.

41. Shinsuke Miyajima and Keisuke Haga and Akira Yamada and Makoto, K., Low-Temperature Deposition of Highly Conductive n-Type Hydrogenated Nanocrystalline Cubic SiC Films for Solar Cell Applications. *Japanese Journal of Applied Physics* **2006,** *45* (4L), L432; Richards, B.; Brown, A.; Trupke, T.; Corkish, R.; Green, M. In *β-SiC–based Photovoltaic and Optical Devices*, Proceedings of ANZSES Conference, 2002.

42. Yasuda, T.; Kato, M.; Ichimura, M.; Hatayama, T., SiC photoelectrodes for a self-driven water-splitting cell. *Applied Physics Letters* **2012,** *101* (5), -.

43. Tae Song, J.; Mashiko, H.; Kamiya, M.; Nakamine, Y.; Ohtomo, A.; Iwasaki, T.; Hatano, M., Improved visible light driven photoelectrochemical properties of 3C-SiC semiconductor with Pt nanoparticles for hydrogen generation. *Applied Physics Letters* **2013,** *103* (21), -.

44. Fissel, A., Artificially layered heteropolytypic structures based on SiC polytypes: molecular beam epitaxy, characterization and properties. *Physics Reports* **2003,** *379* (3–4), 149-255; Severino, A., *3C-SiC epitaxial growth on large area silicon: Thin films*. India, 2012.

45. Severino, A.; D'arrigo, G.; Bongiorno, C.; Scalese, S.; La Via, F.; Foti, G., Thin crystalline 3C-SiC layer growth through carbonization of differently oriented Si substrates. *Journal of Applied Physics* **2007,** *102* (2), 023518.

46. Lebedev, A. A., Heterojunctions and superlattices based on silicon carbide. *Semiconductor Science and Technology* **2006,** *21* (6), R17.

47. Nagasawa, H.; Yagi, K.; Kawahara, T., 3C-SiC hetero-epitaxial growth on undulant Si(0 0 1) substrate. *Journal of Crystal Growth* **2002,** *237–239, Part 2* (0), 1244-1249.

48. Gas chromatography. http://www.chromedia.org/chromedia?waxtrapp=gaxgflDsHqnOxmOlIEcCxBDgB&subNav=jvcykmDsHqnOxmOlIEcCxBDgBfB.

49. Sang-il Park, J. H., and Younggil Nho http://optics.khu.ac.kr/optics/.

50. Raman principle. http://www.see.ed.ac.uk/cbee/Raman2.html.

51. XPS. http://blog.naver.com/hjh4142.

52. Akikusa, J.; Khan, S. U. M., Photoelectrolysis of water to hydrogen in p-SiC/Pt and p-SiC/ n-TiO2 cells. *International Journal of Hydrogen Energy* **2002,** *27* (9), 863-870; Quan-Bao Ma and Bernhard Kaiser and Jürgen Ziegler and Dominic Fertig and Wolfram, J., XPS characterization and photoelectrochemical behaviour of p-type 3C-SiC films on p-Si substrates for solar water splitting. *Journal of Physics D: Applied Physics* **2012,** *45* (32), 325101.

53. Kato, M.; Yasuda, T.; Miyake, K.; Ichimura, M.; Hatayama, T., Epitaxial p-type SiC as a self-driven photocathode for water splitting. *International Journal of Hydrogen Energy* **2014,** *39* (10), 4845-4849.

54. Kaplan, R.; Wagner, R. J.; Kim, H. J.; Davis, R. F., Electron cyclotron resonance in cubic SiC. *Solid State Communications* **1985,** *55* (1), 67-69.

55. Solar cell Operational Principles. http://ocw.tudelft.nl/fileadmin/ocw/courses/SolarCells/res00028/CH4_Solar_cell_operational_principles.pdf.

56. Christiana Honsberg, a. S. B., *PVCDROM*.

57. Polman, A.; Atwater, H. A., Photonic design principles for ultrahigh-efficiency photovoltaics. *Nat Mater* **2012,** *11* (3), 174-177.

58. Weber, M. F.; Dignam, M. J., Splitting water with semiconducting photoelectrodes—Efficiency considerations. *International Journal of Hydrogen Energy* **1986,** *11* (4), 225-232; Weber, M. F.; Dignam, M. J., Efficiency of Splitting Water with Semiconducting Photoelectrodes. *Journal of The Electrochemical Society* **1984,** *131* (6), 1258-1265.

59. Jun, K. Iron-oxide catalyzed silicon photoanode for water splitting. Massachusetts institute of technology, 2011.

60. Satoshi Yotsuhashi and Masahiro Deguchi and Yuji Zenitani and Reiko Hinogami and Hiroshi Hashiba and Yuka Yamada and Kazuhiro, O., CO 2 Conversion with Light and Water by GaN Photoelectrode. *Japanese Journal of Applied Physics* **2012,** *51* (2S), 02BP07.

61. Hou, Y.; Abrams, B. L.; Vesborg, P. C. K.; Björketun, M. E.; Herbst, K.; Bech, L.; Setti, A. M.; Damsgaard, C. D.; Pedersen, T.; Hansen, O.; Rossmeisl, J.; Dahl, S.; Nørskov, J. K.; Chorkendorff, I., Bioinspired molecular co-catalysts bonded to a silicon photocathode for solar hydrogen evolution. *Nat Mater* **2011,** *10* (6), 434-438.

62. Sivula, K., Metal Oxide Photoelectrodes for Solar Fuel Production, Surface Traps, and Catalysis. *The Journal of Physical Chemistry Letters* **2013,** *4* (10), 1624-1633.

63. Ning, Y. T. a. T., *Fundamentals of Modern VLSI Devices*. 2nd Edition ed.; Cambridge University Press: New York, 2009.

64. Ichimura, M., Slow Photoconductivity Decay in 3C-SiC on Si Substrates. *J. Appl. Phys.* **1998,** *84* (5), 2727-2731.

65. Ichimura, M.; Tajiri, H.; Morita, Y.; Yamada, N.; Usami, A., Excess carrier lifetime of 3C–SiC measured by the microwave photoconductivity decay method. *Applied Physics Letters* **1997,** *70* (13), 1745-1747.

66. Le Formal, F.; Tetreault, N.; Cornuz, M.; Moehl, T.; Gratzel, M.; Sivula, K., Passivating surface states on water splitting hematite photoanodes with alumina overlayers. *Chemical Science* **2011,** *2* (4), 737-743.

67. Masashi Kato and Masaya Ichimura and Eisuke, A., Sacrificial Anodic Oxidation of 6H-SiC. *Japanese Journal of Applied Physics* **2001,** *40* (11A), L1145; Shor, J. S.; Kurtz, A. D., Photoelectrochemical Etching of 6 H-SiC. *Journal of the Electrochemical Society* **1994,** *141* (3), 778-781.

68. Severino, A.; Camarda, M.; Scalese, S.; Fiorenza, P.; Di Franco, S.; Bongiorno, C.; La Magna, A.; La Via, F., "Preferential oxidation of stacking faults in epitaxial off-axis (111) 3C-SiC films". *Appl Phys Lett* **2009,** *95*, 111905.

69. Hassan, M., Reliability of Pt ohmic contact on an undoped 3C-SiC micro-electrothermal device. *Microsystem technologies* **2011,** *17* (1), 15-18.

70. Bora, T.; Kyaw, H. H.; Sarkar, S.; Pal, S. K.; Dutta, J., Highly efficient ZnO/Au Schottky barrier dye-sensitized solar cells: Role of gold nanoparticles on the charge-transfer process. *Beilstein Journal of Nanotechnology* **2011,** *2*, 681-690.

71. Khan, S. U. M.; Al-Shahry, M.; Ingler, W. B., Efficient Photochemical Water Splitting by a Chemically Modified n-TiO2. *Science* **2002,** *297* (5590), 2243-2245.

72. Eriksson, J.; Roccaforte, F.; Reshanov, S.; Giannazzo, F.; Lo Nigro, R.; Raineri, V., Evolution of the electrical characteristics of Pt/3C-SiC Schottky contacts upon thermal annealing. *AIP Conference Proceedings* **2010,** *1292* (1), 75-78.

73. Hikaru Kobayashi and Fumiaki Mizuno and Yoshihiro, N., Improvement in Hydrogen Photoevolution Efficiency for Platinum-Deposited Indium Phosphide Electrodes by the Removal of Surface States. *Japanese Journal of Applied Physics* **1994,** *33* (10R), 6065; Ueda, K.; Nakato, Y.; Suzuki, N.; Tsubomura, H., Silicon electrodes coated with extremely small platinum islands for efficient solar energy conversion. *Journal of The Electrochemical Society* **1989,** *136* (8), 2280-2285.

74. Nakato, Y.; Tsubomura, H., Structures and functions of thin metal layers on semiconductor electrodes. *Journal of Photochemistry* **1985,** *29* (1–2), 257-266.

75. Nakato, Y.; Ueda, K.; Yano, H.; Tsubomura, H., Effect of microscopic discontinuity of metal overlayers on the photovoltages in metal-coated semiconductor-liquid junction photoelectrochemical cells for efficient solar energy conversion. *The Journal of Physical Chemistry* **1988,** *92* (8), 2316-2324.

76. Parkinson, C. R.; Walker, M.; McConville, C. F., Reaction of atomic oxygen with a Pt surface: chemical and structural determination using XPS, CAICISS and LEED. *Surface Science* **2003,** *545* (1–2), 19-33.

77. Danyluk, S.; McGuire, G. E., Platinum silicide formation: Electron spectroscopy of the platinum‐platinum silicide interface. *Journal of Applied Physics* **1974,** *45* (12), 5141-5144.

78. Eriksson, J.; Roccaforte, F.; Reshanov, S.; Leone, S.; Giannazzo, F.; LoNigro, R.; Fiorenza, P.; Raineri, V., Nanoscale characterization of electrical transport at metal/3C-SiC interfaces. *Nanoscale Research Letters* **2011,** *6* (1), 120.

79. A. Jorio, M. D., R. Saito, and G. F. Dresselhaus, *Raman Spectroscopy in Graphene Related System*. Wiley-VCH: Weinheim, 2011; Tahara, K.; Iwasaki, T.; Matsutani, A.; Hatano, M., Effect of radical fluorination on mono- and bi-layer graphene in Ar/F2 plasma. *Applied Physics Letters* **2012,** *101* (16), -.

80. Winkler, M. T.; Cox, C. R.; Nocera, D. G.; Buonassisi, T., Modeling integrated photovoltaic–electrochemical devices using steady-state equivalent circuits. *Proceedings of the National Academy of Sciences* **2013,** *110* (12), E1076-E1082.

81. Walter, M. G.; Warren, E. L.; McKone, J. R.; Boettcher, S. W.; Mi, Q.; Santori, E. A.; Lewis, N. S., Solar Water Splitting Cells. *Chemical Reviews* **2010,** *110* (11), 6446-6473; Pourbaix, M., *Atlas of Electrochemical Equilibria in Aqueous Solutions*. National Association of Corrosion Engineers: Houston, 1974; Vol. ed. 2.

82. Kazuhiro Ohkawa and Wataru Ohara and Daisuke Uchida and Momoko, D., Highly Stable GaN Photocatalyst for Producing H 2 Gas from Water. *Japanese Journal of Applied Physics* **2013,** *52* (8S), 08JH04; Kainthla, R. C.; Zelenay, B.; Bockris, J. O. M., Significant Efficiency Increase in Self-Driven Photoelectrochemical Cell for Water Photoelectrolysis. *Journal of The Electrochemical Society* **1987,** *134* (4), 841-845; Liu, R.; Zheng, Z.; Spurgeon, J.; Yang, X., Enhanced photoelectrochemical water-splitting performance of semiconductors by surface passivation layers. *Energy & Environmental Science* **2014,** *7* (8), 2504-2517; Nakato, Y.; Ohnishi, T.; Tsubomura, H., PHOTO-ELECTROCHEMICAL BEHAVIORS OF SEMICONDUCTOR ELECTRODES COATED WITH THIN METAL FILMS. *Chemistry Letters* **1975,** *4* (8), 883-886.

83. Fan, F. R. F.; Shea, T. V.; Bard, A. J., Semiconductor Electrodes: LIV . Effect of Redox Couple, Doping Level, and Metal Type on the Electrochemical and Photoelectrochemical Behavior of Silicide-Coated n-Type Silicon Photoelectrodes. *Journal of*

The Electrochemical Society **1984,** *131* (4), 828-833; Howe, A. T.; Hawkins, R. T.; Fleisch, T. H., Photoelectrochemical Cells of the Electrolyte-Metal-Insulator-Semiconductor (EMIS) Configuration: I . Metal Thickness and Coverage Effects in the Pt/Silicon Oxide/n-Si System. *Journal of The Electrochemical Society* **1986,** *133* (7), 1369-1375; Contractor, A. Q.; Bockris, J. O. M., Investigation of a protective conducting silica film on n-silicon. *Electrochimica Acta* **1984,** *29* (10), 1427-1434; Jun Tae Song and Takayuki Iwasaki and Mutsuko, H., Pt co-catalyst effect on photoelectrochemical properties of 3C-SiC photo-anode. *Japanese Journal of Applied Physics* **2014,** *53* (5S1), 05FZ04.

84. Prasai, D.; Tuberquia, J. C.; Harl, R. R.; Jennings, G. K.; Bolotin, K. I., Graphene: Corrosion-Inhibiting Coating. *ACS Nano* **2012,** *6* (2), 1102-1108; Sutter, E.; Albrecht, P.; Camino, F. E.; Sutter, P., Monolayer graphene as ultimate chemical passivation layer for arbitrarily shaped metal surfaces. *Carbon* **2010,** *48* (15), 4414-4420; Chen, S.; Brown, L.; Levendorf, M.; Cai, W.; Ju, S.-Y.; Edgeworth, J.; Li, X.; Magnuson, C. W.; Velamakanni, A.; Piner, R. D.; Kang, J.; Park, J.; Ruoff, R. S., Oxidation Resistance of Graphene-Coated Cu and Cu/Ni Alloy. *ACS Nano* **2011,** *5* (2), 1321-1327.

85. Nair, R. R.; Blake, P.; Grigorenko, A. N.; Novoselov, K. S.; Booth, T. J.; Stauber, T.; Peres, N. M. R.; Geim, A. K., Fine Structure Constant Defines Visual Transparency of Graphene. *Science* **2008,** *320* (5881), 1308-1308.

86. Aristov, V. Y.; Urbanik, G.; Kummer, K.; Vyalikh, D. V.; Molodtsova, O. V.; Preobrajenski, A. B.; Zakharov, A. A.; Hess, C.; Hänke, T.; Büchner, B.; Vobornik, I.; Fujii, J.; Panaccione, G.; Ossipyan, Y. A.; Knupfer, M., Graphene Synthesis on Cubic SiC/Si Wafers. Perspectives for Mass Production of Graphene-Based Electronic Devices. *Nano Letters* **2010,** *10* (3), 992-995.

87. Maki Suemitsu and Sai Jiao and Hirokazu Fukidome and Yasunori Tateno and Isao Makabe and Takashi, N., Epitaxial graphene formation on 3C-SiC/Si thin films. *Journal of Physics D: Applied Physics* **2014,** *47* (9), 094016.

88. Emtsev, K. V.; Bostwick, A.; Horn, K.; Jobst, J.; Kellogg, G. L.; Ley, L.; McChesney, J. L.; Ohta, T.; Reshanov, S. A.; Rohrl, J.; Rotenberg, E.; Schmid, A. K.; Waldmann, D.; Weber, H. B.; Seyller, T., Towards wafer-size graphene layers by atmospheric pressure graphitization of silicon carbide. *Nat Mater* **2009,** *8* (3), 203-207.

89. Lee, D. S.; Riedl, C.; Krauss, B.; von Klitzing, K.; Starke, U.; Smet, J. H., Raman Spectra of Epitaxial Graphene on SiC and of Epitaxial Graphene Transferred to SiO2. *Nano Letters* **2008,** *8* (12), 4320-4325.

90. Fukidome, H.; Ide, T.; Kawai, Y.; Shinohara, T.; Nagamura, N.; Horiba, K.; Kotsugi, M.; Ohkochi, T.; Kinoshita, T.; Kumighashira, H.; Oshima, M.; Suemitsu, M., Microscopically-Tuned Band Structure of Epitaxial Graphene through Interface and Stacking Variations Using Si Substrate Microfabrication. *Sci. Rep.* **2014,** *4*.

91. Kim, J.-H.; Hwang, J. H.; Suh, J.; Tongay, S.; Kwon, S.; Hwang, C. C.; Wu, J.; Young Park, J., Work function engineering of single layer graphene by irradiation-induced defects. *Applied Physics Letters* **2013,** *103* (17), -.

92. Liang, X.; Sperling, B. A.; Calizo, I.; Cheng, G.; Hacker, C. A.; Zhang, Q.; Obeng, Y.; Yan, K.; Peng, H.; Li, Q.; Zhu, X.; Yuan, H.; Hight Walker, A. R.; Liu, Z.; Peng, L.-m.; Richter, C. A., Toward Clean and Crackless Transfer of Graphene. *ACS Nano* **2011,** *5* (11), 9144-9153; Parvez, K.; Wu, Z.-S.; Li, R.; Liu, X.; Graf, R.; Feng, X.; Müllen, K., Exfoliation of Graphite into Graphene in Aqueous Solutions of Inorganic Salts. *Journal of the American Chemical Society* **2014,** *136* (16), 6083-6091.

93. Norimatsu, W.; Kusunoki, M., Epitaxial graphene on SiC{0001}: advances and perspectives. *Physical Chemistry Chemical Physics* **2014,** *16* (8), 3501-3511.

94. Yang, R.; Huang, Q. S.; Chen, X. L.; Zhang, G. Y.; Gao, H.-J., Substrate doping effects on Raman spectrum of epitaxial graphene on SiC. *Journal of Applied Physics* **2010,** *107* (3), -.

95. Sonde, S.; Giannazzo, F.; Raineri, V.; Yakimova, R.; Huntzinger, J. R.; Tiberj, A.; Camassel, J., Electrical properties of the graphene (0001) interface probed by scanning current spectroscopy. *Physical Review B* **2009,** *80* (24), 241406; Nozik, A. J.; Memming, R., Physical Chemistry of Semiconductor−Liquid Interfaces. *The Journal of Physical Chemistry* **1996,** *100* (31), 13061-13078.

96. Yeh, T.-F.; Cihlář, J.; Chang, C.-Y.; Cheng, C.; Teng, H., Roles of graphene oxide in photocatalytic water splitting. *Materials Today* **2013,** *16* (3), 78-84.

97. Jang, M.; Trung, T. Q.; Jung, J.-H.; Kim, B.-Y.; Lee, N.-E., Improved performance and stability of field-effect transistors with polymeric residue-free graphene channel transferred by gold layer. *Physical Chemistry Chemical Physics* **2014,** *16* (9), 4098-4105; Ni, Z. H.; Wang, H. M.; Ma, Y.; Kasim, J.; Wu, Y. H.; Shen, Z. X., Tunable Stress and Controlled Thickness Modification in Graphene by Annealing. *ACS Nano* **2008,** *2* (5), 1033-1039; Ouerghi, A.; Kahouli, A.; Lucot, D.; Portail, M.; Travers, L.; Gierak, J.; Penuelas, J.; Jegou, P.; Shukla, A.; Chassagne, T.; Zielinski, M., Epitaxial graphene on cubic SiC(111)/Si(111) substrate. *Applied Physics Letters* **2010,** *96* (19), 191910.

98. Starke, C. R. a. C. C. a. U., Structural and electronic properties of epitaxial graphene on SiC(0 0 0 1): a review of growth, characterization, transfer doping and hydrogen intercalation. *Journal of Physics D: Applied Physics* **2010,** *43* (37), 374009.

99. Pallecchi, E.; Lafont, F.; Cavaliere, V.; Schopfer, F.; Mailly, D.; Poirier, W.; Ouerghi, A., High Electron Mobility in Epitaxial Graphene on 4H-SiC(0001) via post-growth annealing under hydrogen. *Sci. Rep.* **2014,** *4*.

100. Huh, S.; Park, J.; Kim, Y. S.; Kim, K. S.; Hong, B. H.; Nam, J.-M., UV/Ozone-Oxidized Large-Scale Graphene Platform with Large Chemical Enhancement in Surface-Enhanced Raman Scattering. *ACS Nano* **2011,** *5* (12), 9799-9806.

101. Iizuka, K.; Wato, T.; Miseki, Y.; Saito, K.; Kudo, A., Photocatalytic Reduction of Carbon Dioxide over Ag Cocatalyst-Loaded ALa4Ti4O15 (A = Ca, Sr, and Ba) Using Water as a Reducing Reagent. *Journal of the American Chemical Society* **2011,** *133* (51), 20863-20868; Yano, H.; Shirai, F.; Nakayama, M.; Ogura, K., Efficient electrochemical conversion of CO2 to CO, C2H4 and CH4 at a three-phase interface on a Cu net electrode in acidic solution. *Journal of Electroanalytical Chemistry* **2002,** *519* (1–2), 93-100; Arai, T.; Sato, S.; Kajino, T.; Morikawa, T., Solar CO2 reduction using H2O by a semiconductor/metal-complex hybrid photocatalyst: enhanced efficiency and demonstration of a wireless system using SrTiO3 photoanodes. *Energy & Environmental Science* **2013,** *6* (4), 1274-1282.

102. Rosen, B. A.; Salehi-Khojin, A.; Thorson, M. R.; Zhu, W.; Whipple, D. T.; Kenis, P. J. A.; Masel, R. I., Ionic Liquid–Mediated Selective Conversion of CO2 to CO at Low Overpotentials. *Science* **2011,** *334* (6056), 643-644.

103. Hiroshi Hashiba and Satoshi Yotsuhashi and Masahiro Deguchi and Yuka Yamada and Kazuhiro, O., Selectivity Control of CO 2 Reduction in an Inorganic Artificial Photosynthesis System. *Applied Physics Express* **2013,** *6* (9), 097102.

104. Sreekanth, N.; Phani, K. L., Selective reduction of CO2 to formate through bicarbonate reduction on metal electrodes: new insights gained from SG/TC mode of SECM. *Chemical Communications* **2014,** *50* (76), 11143-11146.

105. Kaneco, S.; Katsumata, H.; Suzuki, T.; Ohta, K., Photoelectrocatalytic reduction of CO2 in LiOH/methanol at metal-modified p-InP electrodes. *Applied Catalysis B: Environmental* **2006,** *64* (1–2), 139-145.

106. B. Hu, a. S. L. S., *Green Carbon Dioxide: Advances in CO2 Utilization*. Wiley: New Jersey, 2014.

107. Frese Jr, K. W., Calculation of surface binding energy for hydrogen, oxygen, and carbon atoms on metallic surfaces. *Surface Science* **1987,** *182* (1–2), 85-97.

108. Li, W., *Advanced in CO_2 conversion and utilization*. ACE Symp. Ser.: 2010; Hoshi, N.; Kato, M.; Hori, Y., Electrochemical reduction of CO2 on single crystal electrodes of silver Ag(111), Ag(100) and Ag(110). *Journal of Electroanalytical Chemistry* **1997,** *440* (1–2), 283-286; Lu, Q.; Rosen, J.; Zhou, Y.; Hutchings, G. S.; Kimmel, Y. C.; Chen, J. G.; Jiao, F., A selective and efficient electrocatalyst for carbon dioxide reduction. *Nat Commun* **2014,** *5*.

109. Hori, Y.; Wakebe, H.; Tsukamoto, T.; Koga, O., Electrocatalytic process of CO selectivity in electrochemical reduction of CO2 at metal electrodes in aqueous media. *Electrochimica Acta* **1994,** *39* (11–12), 1833-1839.

110. Esposito, D. V.; Levin, I.; Moffat, T. P.; Talin, A. A., H2 evolution at Si-based metal–insulator–semiconductor photoelectrodes enhanced by inversion channel charge collection and H spillover. *Nat Mater* **2013,** *12* (6), 562-568.

111. Cotal, H.; Fetzer, C.; Boisvert, J.; Kinsey, G.; King, R.; Hebert, P.; Yoon, H.; Karam, N., III-V multijunction solar cells for concentrating photovoltaics. *Energy & Environmental Science* **2009,** *2* (2), 174-192.

Acknowledgement

First of all, I really would like to express my deepest appreciation to my supervisor, Prof. Hatano to give me an opportunity to study as a doctoral student in her laboratory at Tokyo Institute of Technology. She has continually supported in regard to my research and prospective with priceless advices and kindly cared about me to adapt in Japanese life. I am very encouraged by her passion and cheerful personality. Without her supervision and constant help this thesis would not be possible.

I would like to thank Dr. Iwasaki for valuable discussion and advices about my research. For doing an experiment, his advice is always helpful to get important result. He gave me valuable feedback for my publications and makes me to find what is missing in the manuscripts. Especially, lunch time in India curry restaurant with him on every Monday is never forgettable as refreshing time in a week.

I would like to thank Prof. Kodera to kindly encourage me for my research. Especially, the discussion about new project for artificial photosynthesis was very helpful for me to consider the issues. Through his new project about artificial photosynthesis, I could realize many issues again. Furthermore, he helped me to grasp the self-confidence concerning my achievements when I felt very depressed.

I would like to express special thanks to Prof. Oda, Prof. Miyamoto, and Prof. Kawano for critical comments on my research presentation inside device group to examine this thesis.

I would like to thank Prof. Ohtomo and Mr. Mashiko to provide a chance to use UV-Vis spectroscopy for valuable results of publication and discuss for the research progress.

I would like to appreciate Prof. Fujii at University of Tokyo to examine my thesis and to give me an opportunity to learn the technology of impedance measurement. I thank to Mr.

Nakamura for teaching me how to measure the impedance of semiconductor/solution junction actually. When I am not familiar to this research at 1st year of doctoral course, it is greatly helpful to understand and start the research.

I would like to thank Dr. Nakamine for advice about the research and funny small talks in the laboratory.

I would like to thank all current students, postdoctoral and secretaries in Hatano-Kodera laboratory with precious memories for three years. I also thank previous lab member, Mr. Kamiya and Mr. Hoshino for helping me to use experimental instruments and taking care of me to adapt in Japan.

I would like to express my gratitude to Dr. Kang in Konagai lab for cheering me up always when I felt anxiety against bright future. Also, thanks to my many precious friends for sending a message of support and prayer for me.

I would like to thank my beloved family, father, mother and my sister for their kind love, support during the completion of this study far away in Korea. I deeply thank to my Hyunha. She is always supporting me and spending a hard time together with aiming doctoral degree in Tokyo tech. It is really the most priceless bless of God.

I appreciate with all my heart that God always keeps supporting me by love. “But He knows the way that I take (He has concern for it, appreciates, and pays attention to it). When He has tried me, I shall come forth as refined gold (pure and luminous), Job 23:10”.

Publication List

SCI Journal

1) **Jun Tae Song**, Takayuki Iwasaki, and Mutsuko Hatano, Photoelectrochemical CO_2 reduction on 3C-SiC photo-anode with product selectivity in aqueous solution, Japanese Journal of Applied Physics, 54, scheduled to be published, 2015.

2) **Jun Tae Song**, Takayuki Iwasaki, and Mutsuko Hatano, Pt co-catalyst effect on photoelectrochemical properties of 3C-SiC photo-anode, Japanese Journal of Applied Physics, 53, 05FZ04, 2014.

3) **Jun Tae Song**, Hisanori Mashiko, Masayuki Kamiya, Yoshifumi Nakamine, Akira Ohtomo, Takayuki Iwasaki, and Mutsuko Hatano, Improved visible light driven photoelectrochemical properties of 3C-SiC semiconductor with Pt nanoparticles, Applied Physics Letter (APL), 103, 213901, 2013.

International conference

1) **Jun Tae Song**, Takayuki Iwasaki, and Mutsuko Hatano, Photoelectrochemical CO_2 conversion system with 3C-SiC photo-anode and Pt counter electrode, International conference on Solid State Devices and Materials (SSDM), Tsukuba, Japan, September, 2014.

2) **Jun Tae Song**, Takayuki Iwasaki, and Mutsuko Hatano, Improved visible light driven photoelectrochemical (PEC) properties of 3C-SiC semiconductor with Pt nanoparticles for hydrogen generation, The second International Education Forum on Environmental and Energy Science (ACEEES), California, USA, December, 2013.

3) **Jun Tae Song**, Yoshifumi Nakamine, Takayuki Iwasaki, and Mutsuko Hatano, Pt co-catalyst effect for improving 3C-SiC photo-anode properties, JSAP-MRS Joint Symposia, Kyoto, Japan, 2013.

4) **Jun Tae Song**, Takayuki Iwasaki, and Mutsuko Hatano, Photoelectrochemical water splitting using n-type 3C-SiC with visible light response, 2013 MRS Spring Meeting & Exhibit, D7.06, San Francisco, USA, 2013

5) **Jun Tae Song**, Yoshifumi Nakamine, Takayuki Iwasaki, and Mutsuko Hatano, Enhancement of 3C-SiC semiconductor photo-anode performance for water splitting using Pt co-catalysts, IEEE EDS WIMNACT 37 Future Trend of Nanodevices and Photonics, P-43,

Tokyo, Japan, Feburary, 2013.

6) **Jun Tae Song**, Takayuki Iwasaki, and Mutsuko Hatano, Photoelectrochemical properties of SiC semiconductor for water splitting, The First International Education Forum on Environment and Energy Science (ACEEES), Hawaii, USA, December, 2012.

Domestic conference

1) **Jun Tae Song**, Shunnosuke Akabane, Renato Goes Amici, Takayuki Iwasaki, and Mutsuko Hatano, Photoelectrochemical CO_2 reduction on 3C-SiC photo-anode, The 75th JSAP Autumn Meeting, Sapporo, September, 2014.

2) Shunnosuke Akabane, **Jun Tae Song**, Renato Goes Amici, Keiko Miyake, Masashi Kato, Takayuki Iwasaki, and Mutsuko Hatano, p-type 3C-SiC photo-electrodes for stable and high efficient water splitting, The 75th JSAP Autumn Meeting, Sapporo, September, 2014.

3) Hisanori Mashiko, **Jun Tae Song**, Takayuki Iwasaki, Mutsuko Hatano, Takayoshi Oshima, Akira Ohtomo, characterization of Semiconductor-Photoelectrodes Based on α-$(CrxFe1\text{-}x)_2O_3$ Films, The 60th JSAP Spring Meeting, Kanagawa, March, 2013.

4) **Jun Tae Song**, Yoshifumi Nakamine, Takayuki Iwasaki, and Mutsuko Hatano, Enhanced Photoelectrochemical Properties of 3C-SiC by Pt co-catalysts, The 60th JSAP Spring Meeting, Kanagawa, March, 2013.

5) **Jun Tae Song**, Takayuki Iwasaki, and Mutsuko Hatano, Photoelectrochemical Properties of SiC semiconductor for water splitting, The Fifth Energy-GCOE Career Development Program Forum, Tokyo, Japan, September, 2012.

Appendix A

Semiconductor

Solid materials are classified to metal, semiconductor and insulator with electric properties explained by the concept of band-gap (E_g). Here, semiconductor has a moderate E_g, so it is possible for some electrons in valance band to conduction band area by some external stimulation. As an example that an external stimulation is photo excitation, an electron can be excited from the valance band to the conduction band by one photon excitation. In this process, the value of E_g which is different with the type of semiconductors is important variable to decide the amount of generated energy from solar-light. Semiconductor materials are divided to intrinsic and extrinsic semiconductor according to the doping of impurity. Intrinsic semiconductor has a Fermi level (E_F), which means the energy level occupied by electron at the probability of half, located at the middle between conduction and valance band. At the temperature of 0 K, no electron exists except for valance band region. However, the electron might be thermally excited to the conduction band above 0 K. This variable electron distribution is explained by the Fermi-Dirac distribution with density of states. The Fermi function providing the probability that an electron energy state is occupied at temperature T is given by:

$$f(E) = \frac{1}{1 + e^{(E - E_F)/kT}} \tag{A.1}$$

The density of energy states ($g(E)$) indicating that the number of available states in a cubic cm per unit of energy, is expressed by:

$$g_c(E) = \frac{m_n^* \sqrt{2m_n^*(E - E_c)}}{\pi^2 \hbar^3},\ E \geq E_c \tag{A.2}$$

$$g_v(E) = \frac{m_p^* \sqrt{2m_p^*(E_v - E)}}{\pi^2 \hbar^3},\ E \leq E_v \tag{A.3}$$

m_n^* : the effective mass of electron

m_p^* : the effective mass of hole

$\hbar$: $h/2\pi$ (h is Planck's constant)

E_c : the conduction band energy level

E_v : the valance band energy level

By using these two functions (Fermi and density of energy states), the equation to define the number of electrons and holes in the conduction and valance region is obtained as followings.

$$n = \int_{E_c}^{E_{top}} g_c(E) f(E) dE \tag{A.4}$$

$$p = \int_{E_{bottom}}^{E_v} g_v(E)(1 - f(E)) dE \tag{A.5}$$

By substituting the Eq. (A.1), (A.2) and (A.3) to above two equations, the following relationships are finally deducted.

$$n = N_c \exp(\frac{E_F - E_c}{kT}),\ N_c = 2(\frac{2\pi m_n^* kT}{h^2})^{3/2} \tag{A.6}$$

$$p = N_v \exp(\frac{E_v - E_F}{kT}),\ N_v = 2(\frac{2\pi m_p^* kT}{h^2})^{3/2} \tag{A.7}$$

Here, N_c and N_v are considered as the density of states for conduction and valance band, respectively. Second, the extrinsic semiconductor has different Fermi level with regards to the type of impurities. Some impurities has a role of donor which gives additional electrons in the crystal and other impurities are acceptors attract electrons inside the semiconductor. The doped semiconductors with donor and acceptor are called n- and p-type semiconductor. As a result, majority carriers of n- and p-type semiconductors are electrons and holes. The band diagram of these two types of semiconductor is shown in Figure A.1. The position of the Fermi level for n-type is somewhat less than conduction band-edge level due to larger amount of electrons, while p-type has a Fermi level at located closer to valance band-edge level. In the PEC application, the position of semiconductor electrode (oxidation or reduction side) is varied according to the type of semiconductor as dopant.

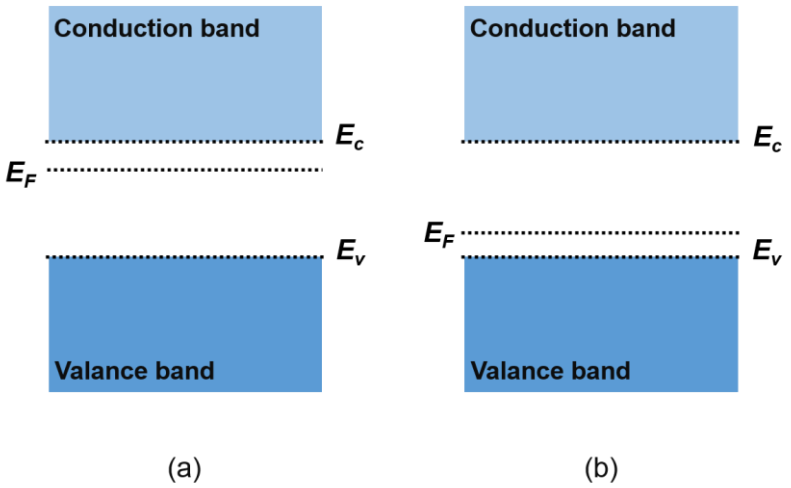

Figure A.1. Band diagram for (a) n-type and (b) p-type semiconductor.

Appendix B

Reference electrode scale comparison

The utility of reference electrode is very important to acquire precise experimental results. While general electric circuit experiments have a ground level as a zero point, there is no any reference in the loop including aqueous solution. In the electrochemical experiment, thus, known potential of redox couples are used as a standard level. Typically, Ag/AgCl in saturated KCl solution used in this thesis is representatively chosen as reference electrode for actual experiment due to its convenience for use. However, its scale is needed to be converted for analysis with variable pH. Here, the scale conversion to compare with other standard potential is explained. First of all, the scale of Ag/AgCl is converted to versus normal hydrogen electrode (NHE) which is comparable with vacuum level. In case of Ag/AgCl in saturated KCl solution, the scale for NHE is expressed as follows:

$$\text{E (V } \textit{vs.}\text{ NHE)} = \text{E (V } \textit{vs.}\text{ Ag/AgCl)} - 0.199\ \text{V} \tag{B.1}$$

$$\text{E (in vacuum)} \approx \text{E (V } \textit{vs.}\text{ NHE)} - 4.5\ \text{V} \tag{B.2}$$

As shown in above equations, this scale is independent on pH value. According to Nernst relationship, the potential in the solution changed with pH value. Therefore, it is critical to consider this scale with pH for proper evaluation especially for photo-electrode. In this case, reversible hydrogen electrode (RHE) scale can be applied with Nernst constant (0.059) as below:

$$\text{E (V } \textit{vs.}\text{ RHE)} = \text{E (V } \textit{vs.}\text{ NHE)} + 0.059 \cdot \text{pH} \tag{B.3}$$